SOURCE DETECTION OF SO2 EMISSIONS WITH UNKNOWN ORIGINS USING UV REMOTE SENSING AND NUMERICAL MODELING

by

Lori Mandable

A Thesis
Submitted to the
Graduate Faculty
of
George Mason University
in Partial Fulfillment of
The Requirements for the Degree
of
Master of Science
Earth Systems Science

Committee:

Guido Cervone	Dr. Guido Cervone, Thesis Director
P. Agouris	Dr. Peggy Agouris, Committee Member
Nigel Waters	Dr. Nigel Waters, Committee Member
P. Agouris	Dr. Peggy Agouris, Department Chair
Timothy L. B	Dr. Timothy L. Born, Associate Dean for Student and Academic Affairs, College of Science
Vikas Chandhoke	Dr. Vikas Chandhoke, Dean, College of Science

Date: 5-1-03

Spring Semester 2013
George Mason University
Fairfax, VA

Source Detection of SO2 Emissions with Unknown Origins Using UV Remote Sensing and Numerical Modeling

A thesis submitted in partial fulfillment of the requirements for the degree of Master of Science at George Mason University

by

Lori Mandable
Bachelor of Science
American University, 1993

Director: Guido Cervone, Professor
Department of Geography and Geoinformation Science

Spring Semester 2013
George Mason University
Fairfax, VA

DEDICATION

This is dedicated to my loving husband Terry, my two wonderful daughters Catherine and Kirstina, my parents, in-laws, grandparents, friends and my Thesis committee who have provided me with immeasurable support and encouragement during this research project.

ACKNOWLEDGEMENTS

I would like to thank the many family, friends and supporters who have made this possible. In particular my Committee, comprised of, Dr. Nigel Waters Dr. Peggy Agouris, and my Advisor, Dr. Guido Cervone, all of whom I regard as not only mentors, but as highly esteemed friends. Dr. Waters provided me with my first employment opportunity in this field, teaching me about the scientific publication process and providing me with support and editorial comments as well as being an incredible mentor. Additionally, he secured a position for me to participate in the annual UCGIS Symposium, for which I am exceedingly grateful. Dr. Agouris was an invaluable resource in teaching me about the Thesis process as well as being a supportive role model as a female scientist balancing work and family responsibilities To my Advisor, Dr. Guido Cervone, I thank you for your boundless patience in working with me, sharing your vast knowledge and insight of source detection methodologies and computer integration, providing me with the opportunity to attend the International Workshop on Source Term Estimation (STE) Methods For Estimating the Atmospheric Radiation Release From the Fukushima Daiichi Nuclear Power Plant, and for giving me advice, constructive criticism, mentoring and encouragement throughout this entire Master's program.

I also want to thank my loving husband, Terry, who supported my research efforts through proofreading, and filling in as Mr. Mom for the past year. My daughters Catherine and Kirstina helped me with hugs and inspiration throughout the process, never letting me doubt in my ability to complete this program. To my friends Debbie and Trish, my parents and in-laws, who endured hours of me talking about volcanoes, computer programs and statistics, thank you for continually providing encouragement to me. Lastly, I would like to thank the faculty and staff of the Departments of Geography and Geoinformation Science as well as Atmospheric, Oceanic and Earth Science for all of their instruction, guidance and support.

TABLE OF CONTENTS

LIST OF TABLES

LIST OF FIGURES

LIST OF EQUATIONS

LIST OF ABBREVIATIONS AND SYMBOLS

Advanced Earth Observing Satellite .... ADEOS
Atmosphere .... atm
Band Residual Difference .... BRD
Centimeter .... cm
Cloud-Aerosol Lidar with Orthogonal Polarization .... CALIOP
Cloud-Aerosol Lidar and Infrared Pathfinder Satellite Observations .... CALIPSO
Carbon Dioxide .... CO_2
Chlorine Cl
Chlorine Dioxide .... ClO_2 or OClO
Coordinated Universal Time .... UTC
Correlation Spectrometer .... COSPEC
Differential Optical Absorption Spectroscopy .... DOAS
Dobson Unit .... DU
European Remote Sensing Satellite .... ERS
European Space Agency .... ESA
Formaldehyde .... CH_2O
Geographic Information System .... GIS
Global Data Assimilation System GDAS1
Global Ozone Monitoring Experiment .... GOME
Gram .... g
Hectopascal .... hPa
Hybrid Single-Particle Lagrangian Integrated Trajectory .... HYSPLIT
Hydroperoxyl .... HO_2
Hydroxide .... OH
Hypobromite .... BrO
Infrared .... IR
International Civil Aviation Organization .... ICAO
Kelvin .... K
Kilogram .... kg
Kilometer .... km
Linear Fit .... LF
Megaton .... Mt
Meter .... m
Micrometer .... µm
Mole .... mol

Molecular oxygen .... O_2
Nanometer .... nm
National Aeronautics and Space Administration .... NASA
National Oceanic and Atmospheric Administration .... NOAA
National Polar-Orbiting Partnership .... NPP
Near Infrared .... NIR
Nitrogen Dioxide .... NO_2
Nitrogen Oxides .... NO_x
Ozone .... O_3
Ozone Mapping Profiler Suite .... OMPS
Ozone Monitoring Instrument .... OMI
Parts per Million .... ppm
Planetary Boundary Layer .... PBL
RMSE .... Root Mean Square Error
Scanning Imaging Absorption Spectrometer for Atmospheric Chartography ....
.... SCIMACHY
Second .... s
Sulfur .... S
Sulfur Dioxide .... SO_2
Sulfur Trioxide .... SO_3
Sulfuric Acid .... H_2SO_4
Sulfurous Acid .... HSO_3
Television Infrared Observation Satellite .... TIROS
Teragram .... Tg
Total Ozone Mapping Spectrometer .... TOMS
Transport & Dispersion .... T&D
Ultraviolet .... UV
United States .... US
Universal Serial Bus .... USB
Upper Troposphere/Lower Stratosphere .... UTLS
Visible .... VIS
Visible and Near-Infrared .... VNIR
Volcanic Ash Advisory Center .... VAAC
Volcanic Explosivity Index .... VEI
Water/Oxidane .... H_2O
Watt .... W

ABSTRACT

SOURCE DETECTION OF SO_2 EMISSIONS WITH UNKNOWN ORIGINS USING UV REMOTE SENSING AND NUMERICAL MODELING

Lori Mandable, M.S.

George Mason University, 2013

Thesis Director: Dr. Guido Cervone

Trace gases such as sulfur dioxide (SO_2) are capable of causing deleterious effects such as radiation damage, climate change, respiratory issues in animals and development of corrosive acid rain. Detection of such trace gases is typically conducted via ground and satellite remote sensing instrument measurements, and when used in tandem with an atmospheric Transport & Dispersion (T&D) model such as the Hybrid Single-Particle Lagrangian Integrated Trajectory (HYSPLIT) system, the results can be used to solve trace gas source detection problems.

This proposal discusses a methodology that combines HYSPLIT backward and forward modeling simulations to identify the characteristics of an unknown source of trace gas emissions. Specifically, this methodology will be used in the case of back tracing a passive SO_2 release to determine the volcanic source. The AURA/OMI satellite can measure atmospheric trace gases, such as SO_2, at a spectral resolution of 0.5nm from UV/VIS wavelengths of 270-500nm covering Earth daily (Levelt et al., 2006, Draxler &

Rolph, 2003). HYSPLIT is a T&D modeling system that can compute concentrations and trajectories associated with atmospheric emissions. It is flexible in its ability to run normal, matrix and ensemble trajectory models at multiple tropospheric heights and incorporate meteorological data from North American or global sources (R. Draxler, Stunder, Rolph, Stein, & Taylor, 2009).

The goal of this research is to identify the important characteristics of an unknown source, such as location, start time, duration of release and the altitude of the top of the release using numerical modeling in tandem with ground/satellite observations. For problems like passive volcanic release where the source is unknown, identifying the location is the primary source term to be estimated. For other problems in which the source location is known, source terms such as duration of the release and the altitude of the top of the release can be determined.

By combining the forward and backward modes, the complete potential of the models is fully harnessed. This system combines the high accuracy associated with forward simulations, assuming known source characteristics, with the flexibility of work with unknown sources associated with backward simulations. Ultimately, this will be a useful tool in back tracing any type of spectrally identified emissions to their source, which could include power and chemical plants, smelting operations, and volcanoes for improved SO_2 emission monitoring and emergency preparedness.

INTRODUCTION

Significance of Research

Sulfur dioxide (SO_2) is a trace gas within Earth's atmosphere with an estimated emissions range of 13-21 Tg S/year from volcanic sources and an overall emissions range of 49.9-54.6 Tg S/year from both natural and anthropogenic sources (Bani et al., 2012; Bhugwant et al., 2009; Lee et al., 2011). SO_2 emissions are responsible for both local and global climate change, the creation of corrosive acid rain, disturbing aircraft traffic patterns, degrading airborne equipment and beneath the atmospheric boundary layer (ABL) is responsible for respiratory issues in animals and preventing plant growth (Georgoulias et al., 2009). Global monitoring of both anthropogenic and volcanic SO_2 emissions is carried out by several remote sensing devices, with the OMI instrument providing the best combination of high-resolution and temporal (daily) coverage.

While anthropogenic sources of SO_2 emissions have been studied, regulated and capped by both national and international agreements, natural sources of SO_2 will continue to affect the issues stated above and therefore need to be repeatedly monitored to minimize the impact to air travel, animals and vegetation. In particular, UV satellite remote sensing techniques allow for monitoring of volcanoes that are in rugged areas in which traditional ground sensor based technology is impractical and/or too costly for a country to maintain (Lopez et al., 2012; Webley et al., 2012). Given that passive volcanic SO_2 emissions are one of the potential signals of a forthcoming eruption, SO_2 monitoring in these regions plays a critical role in evacuation planning, aviation routing and vegetation damage prevention (S.A. Carn, Krueger, Arellano, Krotkov, & Yang, 2008; Simon A. Carn, Krueger, Krotkov, Yang, & Evans, 2009). By back tracking an SO_2 emission to its source through UV remote sensing methodologies, volcanoes that are candidates for possible eruption can be more readily identified and monitored for further eruptive behavior. Additionally, this technology has the added benefit of being able to identify anthropogenic sources of SO_2 emissions to aid in identifying power plant or smelting operations in violation of legislated requirements (Carn et al., 2007).

Research Objectives

The goal of this Thesis is to identify the important source characteristics of a trace gas release, namely the location, duration, and maximum altitude of the release by collecting data from the space borne OMI remote sensing instrument and then using this data to model a backward simulation using the HYSPLIT system to determine the source of the emission. Specifically, this Thesis will explore passive volcanic emissions of SO_2 detected by the OMI instrument to determine their source. Once a candidate source is located, forward modeling simulations will be run on the HYSPLIT system to confirm the source location's legitimacy through sensitivity analysis. After the location's legitimacy is established, source terms such as time of eruption onset, duration and height of release will be determined through an optimization procedure to further quantify the passive emission's characteristics.

Assumptions

For this study, the following assumptions are made to better clarify and narrow the scope of research:

- Passive sulfur dioxide emissions will emanate from a single, stationary source and not travel beyond the tropopause in elevation.
- Sulfur dioxide emissions will be treated as a trace gas release.
- SO_2 trace gas releases will be considered buoyant, remaining in the atmosphere for a period of several days to weeks before settling or recombining to form other particles.
- Once a candidate location has been identified through sensitivity analysis, its latitude, longitude and elevation will be utilized in the optimization routine's parameters as the source latitude, source longitude and altitude of the bottom of the release.

Sulfur Dioxide

Sulfur dioxide, represented by the chemical abbreviation SO_2, is an invisible, colorless gas with the pungent odor of a stricken match. SO_2 is a gas at standard air temperature (273K) and pressure (1 atm), and readily dissolves when exposed to water (Centers for Disease Control and Prevention, 1999; Ebbing, 1996). It is comprised of one sulfur atom covalently bonded to two oxygen atoms, which give the molecule a density of 1.29×10^{-3} g/cm and an atomic mass of 64.066 g/mol (Bridgman, 2005; Ebbing, 1996). This mass is slightly greater than twice the average molecular mass of air within the troposphere, which is 28.97 g/mol, causing SO_2 molecules to descend at an average rate of -2 to 2 cm/s depending on the meteorological conditions, time of day, season and land cover/oceanic conditions (Voldner, Barrie, & Sirois, 1986; Xu & Carmichael, 1998). Following release into the atmosphere, sulfur dioxide gas is toxic to both plant life in as little as 130 $\mu g/(m^3 \cdot hour)$ and animal life in quantities as little as 125 $\mu g/(m^3 \cdot day)$ concentration (Faivre-Pierret & Le Guern, 1983; Knabe, 1976; Newhook, Hirtle, Byrne, & Meek, 2003). Human exposure at 20 ppm is known to cause significant eye irritation and respiratory issues (Ebbing, 1996; Faivre-Pierret & Le Guern, 1983). Figure 1 below illustrates the Lewis and VSPER structures of an SO_2 molecule. This triagonal planar arrangement causes a “bent” structure with a double bond between the S atom and one or both of the O atoms. The bond angle formed by this molecule is approximately 119.5°

between the two O atoms (Admin, 2008).

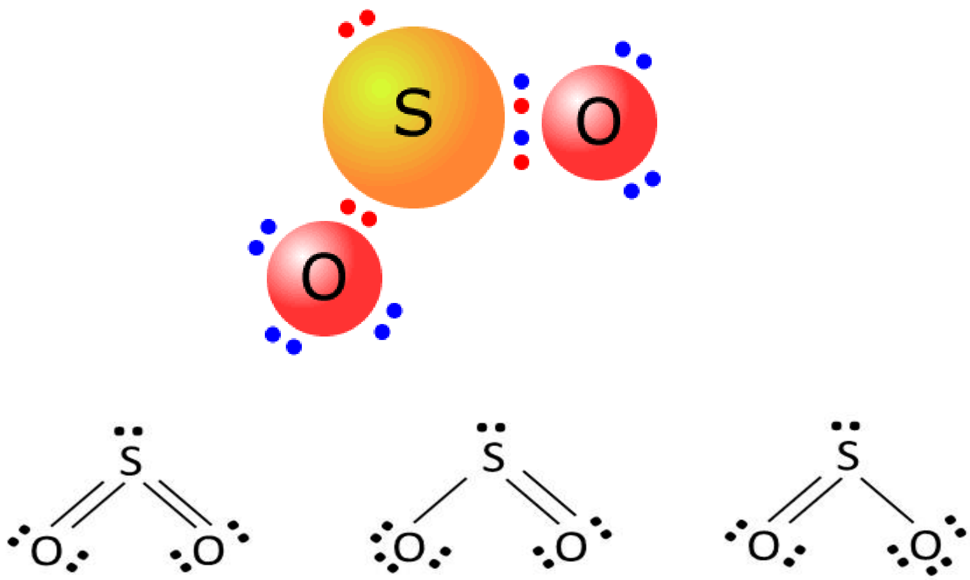

Figure 1: Lewis (top) and VSEPR (bottom) structures of a sulfur dioxide molecule (Admin, 2008; Ebbing, 1996).

This composition and structure are responsible for SO_2's physical and chemical properties described above as well as is its spectral signature. SO_2 displays strong spectral absorption bands in the ultraviolet (UV) portion of the electromagnetic spectrum, with almost full absorbance at 310.80 nm, roughly 65% absorbance at 313.20 nm and troughs of less absorbance at 311.85 nm, 312.61 nm and 314.40 nm. These characteristics distinguish it from the ozone (O_3) molecule allowing for ease in identifying the presence of SO_2 in a UV image.

Sources of Sulfur Dioxide

Sulfur dioxide (SO_2) is a naturally occurring gas that primarily enters the atmosphere as a by-product of anthropogenic burning of fossil fuels and smelting activity as well as via volcanic eruption. Figure 2 below illustrates the sulfur cycle, with approximate amounts of sulfur released as SO_2 from the factory and volcanic activity. The totals reflected in this figure include all forms of S, and therefore display higher amounts than just the sulfur that is measured in SO_2. Whereas anthropogenic activities such as the burning of fossil fuels, the processes used by smelting operations and human-induced forest fires provide the bulk of the 49.9-54.6 Tg S annual SO_2 budget, these activities show a tendency for consistent, low-level background SO_2 emission (Bani et al., 2012; Bhugwant, Sieja, Bessafi, Staudacher, & Ecormier, 2009; Chulkyu Lee et al., 2011).

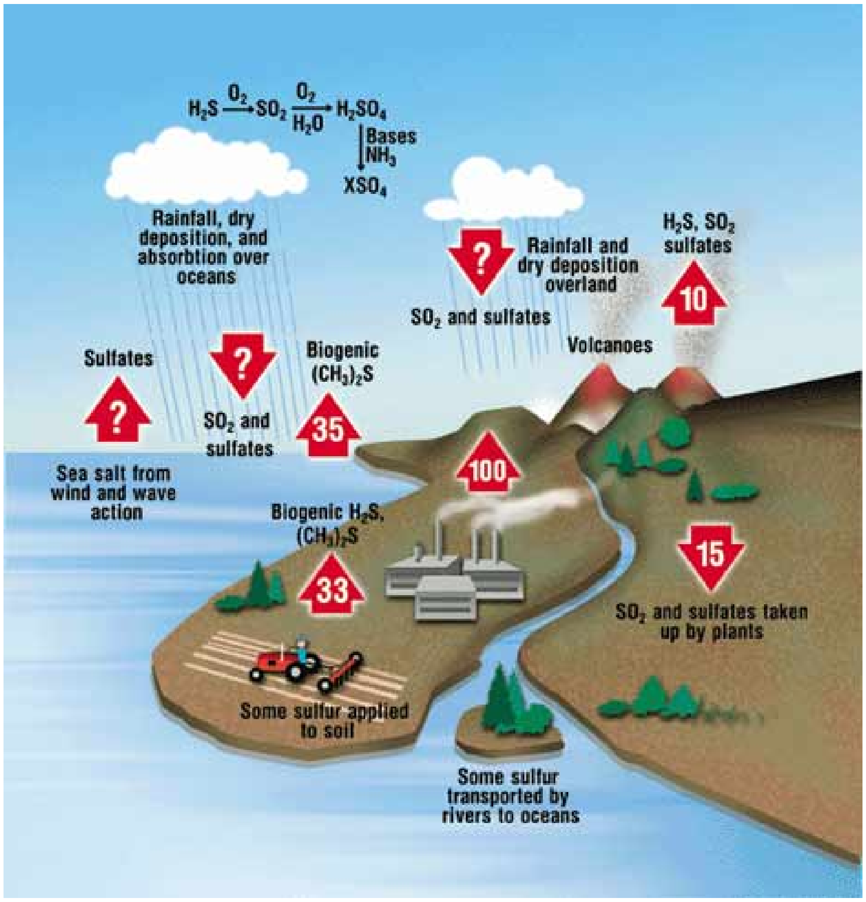

Figure 2: The sulfur cycle. Numbers are represented as Tg of S (Foust, n.d.)

This is in direct contrast to volcanic activity, which is responsible for two types of SO_2 emission. Prior to eruption, many volcanoes will exude SO_2 in small wisps, degassing the upper portions of excess gas from the magma chamber as low altitude tropospheric emissions. Such passive degassing events account for approximately 36% or 4.68-7.56 Tg of annual volcanic SO_2 emissions, and have loss rates of only 10^{-5}/s to 10^{-6}/s (S. A. Carn, Prata, & Karlsdóttir, 2008). However, volcanoes also release roughly 64% or 8.32-

13.44 Tg of their SO_2 annual flux as brief, intermittent large-scale injections of SO_2 into the troposphere and at times, reaching beyond the tropopause into the stratosphere (Bani et al., 2012; Bhugwant et al., 2009; Lee et al., 2011; Stoiber, Williams, & Huebert, 1987). Once in the stratosphere, these particles can take from months to years to fall back to the surface, with an example of a 1 μm radius droplet at 20 km altitude taking approximately 2 weeks to fall 1 km (Lacis, Hansen, & Sato, 1992).

Along with carbon dioxide (CO_2), chlorine (Cl) and water (H_2O), sulfur dioxide is recognized as a volatile component in volcanic magmas, contributing to the magnitude of volcanic eruptions in tandem with silica content (Wallace, 2001). Passive emissions of SO_2 in volcanoes are a general precursor to an eruptive event primarily in areas of convergent plate boundaries where the magma content is of intermediate to felsic composition with silica amounts exceeding 60% (Wallace, 2001). These convergent plate boundaries are illustrated below in Figure 3, where Earth's volcanoes are represented as red dots, convergent plate margins are represented by blue lines with triangles pointing in the direction of dominant or overriding plate thrust, and divergent boundaries are represented by solid red lines with black arrows pointing in the direction of plate movement and indicating the amount of spreading per year (NASA/Goddard Space Flight Center, 2002).

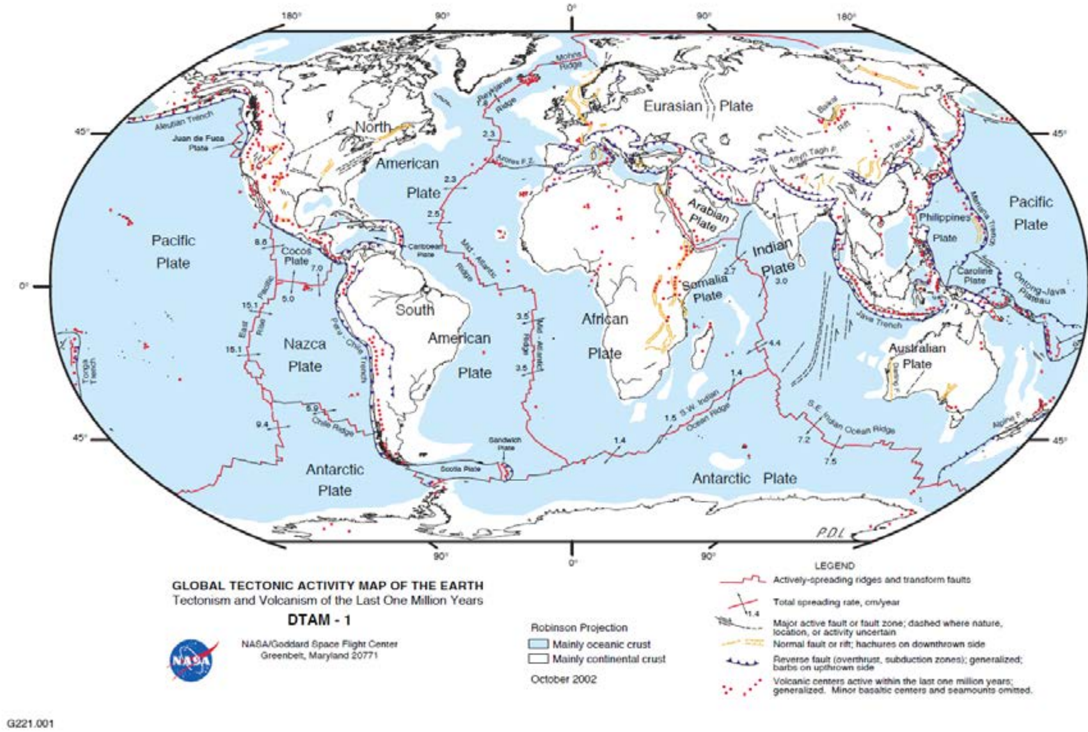

Figure 3: Plate tectonic margins illustrating active volcanoes at the margins (indicated by red dots) convergent plate margins in blue lines with triangles pointing in the direction of dominant plate overrun (NASA/Goddard Space Flight Center, 2002).

Eruptions in these areas are far more explosive, ranking a 3 or higher on the Volcanic Explosivity Index (VEI) in contrast to the more basaltic composition of magma found at divergent plate boundaries and hot spots due to their enriched volatile content and higher viscosity melts (Newhall & Self, 1982). These thick melts tend to separate into a stratified composition with an upper layer of gas-rich magma above lower layers of progressively denser material. As magma flows upward in response to changes in pressure, the magma conduits or volcanic "plumbing" vent this gas as a passive eruption. Three different scenarios of this process are illustrated below in Figure 4 from Boichu, Oppenheimer, Tsanev, & Kyle, 2010.

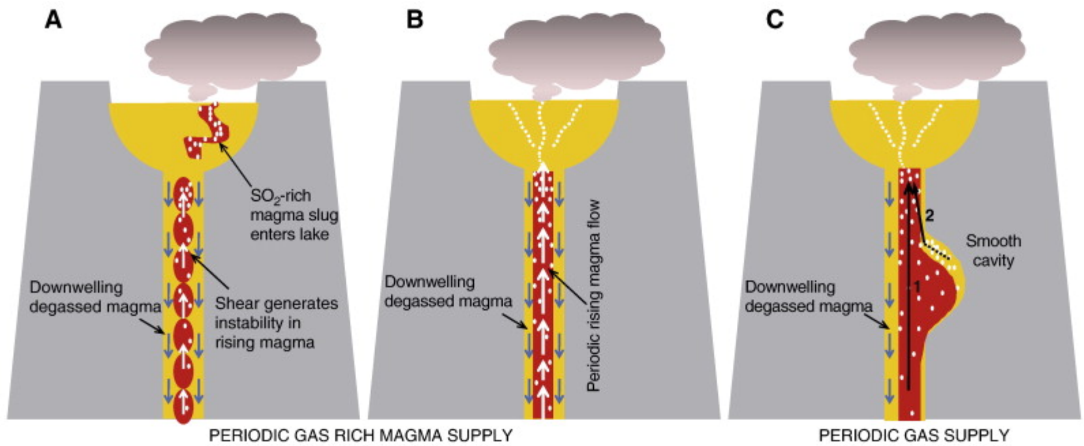

Figure 4: Magmatic degassing scenarios. A) Illustration of shear stresses between the buoyant gas-rich hot rising magma and downwelling cooler degassed counterpart. B) Illustration of volatile dependent viscosity differences. C) Illustration of gas segregation within the smooth cavity (Boichu et al., 2010).

Once this gas rich layer has escaped, explosive eruptions become imminent as the remaining viscous magma is propelled through the conduit due to underlying pressure from magma rising from depth in conjunction with the fracturing of surface rock (Scandone, 1996; Wallace, 2001).

During passive or small volcanic eruptions with a measure of 2 or less on the VEI, SO_2 enters the tropospheric section of the atmosphere, where it either falls back to land or water as dry SO_2 or chemically reacts with water to produce H_2SO_4, sulfuric acid or other sulfates (Aiuppa et al., 2007; Eatough, Caka, & Farber, 1994; Newhall & Self, 1982). The sulfuric acid and sulfates then fall as destructive acid rain that is toxic to vegetation (A. J. Krueger et al., 2009). The following diagram, Figure 3 below illustrates the chemical reactions that take place in the troposphere and stratosphere following SO_2 release.

$$
\begin{array}{lr}
SO_2 + OH \xrightarrow{M} HSO_3 & (1) \\
HSO_3 + O_2 \longrightarrow SO_3 + HO_2 & (2) \\
SO_3 + H_2O \xrightarrow{M} H_2SO_4 & (3)
\end{array}
$$

Equation 1: Chemical reactions in the transformation of sulfur dioxide to sulfuric acid (Khokhar et al., 2005).

If the SO_2 is injected via a violent volcanic eruption, which is typical with eruptions measuring a 3 or greater on the Volcanic Explosivity Index (VEI), then it has the ability to enter the stratospheric section of the atmosphere, where it can reside for several weeks before chemically combining and falling back to Earth (Aiuppa et al., 2007; Eatough et al., 1994; Lacis et al., 1992; McKeen, Liu, & Kiang, 1984). The vertical profile of such an emission can vary greatly and is dependent upon the volatile content of the magma, the explosivity of the eruption, and meteorological conditions. Two such profiles are shown below in Figure 5, with the Sierra Negra volcano exuding a larger, 46 Dobson Units (DU, with 1 DU = 2.69×10^{16} molecules/cm^2), but more quiescent emission typical of a shield volcano than the Manam stratovolcano’s more explosive discharge that produced 21 DU less in SO^2 release (Clerbaux et al., 2008; NASA/Goddard Space Flight Center, 2012).

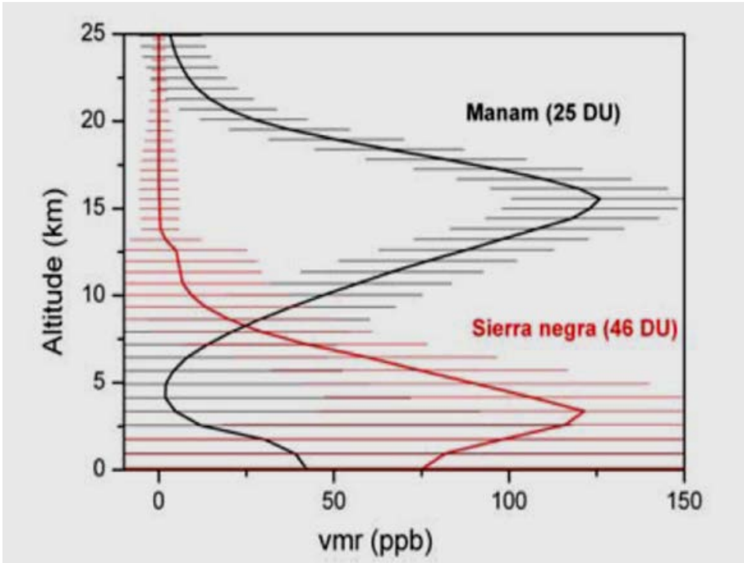

Figure 5: Comparison of SO2 vertical column profiles from two eruptions: Manam, Papua New Guinea and Sierra Negra, Galapagos Islands, Ecuador (Clerbaux et al., 2008).

Deleterious Effects of Sulfur Dioxide

Human and Animal Health

With over 500 million people living in close proximity to active volcanoes and countless more living near fossil fuel burning plants and smelting operations, discerning the impacts sulfur dioxide plays has the environment is a critical issue for hazard mitigation (Baxter, 2005). Sulfur dioxide has direct effects to both the human and larger animal population when it is ingested through inhalation. Human exposure at 100 parts per million (ppm) will burn the victim's nose, throat and bronchial tubes, causing difficulty in respiration. Prolonged exposure at 50 ppm induces airway restrictions in the bronchial tubes, producing a permanent asthmatic effect in the individual (Bhugwant et al., 2009; Centers for Disease Control and Prevention, 1999; Newhook et al., 2003). If exposed individuals already have a proclivity toward pulmonary issues, then SO_2 has been shown to increase instances of respiratory illness, emergency room visits, and mortality rates at consistent concentrations lower than the 50 ppm level described above (Centers for Disease Control and Prevention, 1999). For these reasons, The World Health Organization has established the following guidelines for sulfur dioxide exposure, as outlined below in Table 1, with Interim Target numbers set for countries as goals to decrease their SO_2 emissions and the Air Quality Guideline as the ultimate goal worldwide (Bhugwant et al., 2009).

Table 1: WHO Guidelines for SO_2 Exposure (Bhugwant et al., 2009).

	24 hour Average Exposure in μm/m^3	10-Minute Average Exposure in μm/m^3
Interim Target-1	125	-
Interim Target-2	50	-
Air Quality Guideline	20	500

Respiratory issues are not limited to human exposure to SO_2, as studies have also confirmed the presence of decreased pulmonary activity in animal populations. Chronic exposure has also illustrated inflamed bronchial airways as well as lung deterioration, making SO_2 a pollution hazard for the entire animal kingdom (Centers for Disease Control and Prevention, 1999).

In addition to these deleterious effects, human and animal populations also suffer indirect effects of SO_2 exposure when cropland, grazing sites and other vegetative food sources are damaged by exposure to gaseous emissions (Knabe, 1976). Roughly 30% of reported volcanic fatalities are attributed to post-eruption famines that have wiped out food sources for local populations (Baxter, 2005). These indirect effects also encroach on human and animal activity through the loss of vegetation that filters water and soil, provides erosion and avalanche control, hampering nature conservancy efforts and changing the landscape of areas used for recreational purposes.

Vegetation

Sulfur dioxide is recognized as a "primary air pollutant as well as a primary toxicant" to vegetation (Knabe, 1976). It enters vegetation principally through the plant's stomata, producing two different injury profiles: chronic or acute (Samuel N. Linzon, 1971). Chronic injury occurs when vegetation is exposed to low concentrations of SO_2 gas over extended periods of time, which directly contrasts with acute injury due to shortened exposures of high concentration gas. The extent of injury is dependent upon several factors, as each species of vegetation has differing degrees of tolerance to SO_2

exposure and sensitivities to environmental changes. The chief factors to be considered in an investigation of SO_2 toxicity are the frequency, duration and timing of release, the meterological conditions present, the distance from the release source and the height of the volcano or stack producing the emission (Knabe, 1976; S.N. Linzon, 1965; Samuel N. Linzon, 1971). The higher the frequency and/or duration of emissions, the greater quantity of release during a plant's growing season, windy and humid conditions, closer proximity to the source of the emission and the higher the source elevation all increase the possibility of vegetative damage (Knabe, 1976).

In several studies conducted from 1953-1963 in the forested areas surrounding Sudbury, Ontario, Canada, the effects of SO_2 toxicity were measured on several species of trees, with the Eastern white pine (*Pinus strobus* L) serving as the representative candidate to illustrate forest damage. This location was chosen due to its heavy smelting operations, with the area responsible for 2 million tons of SO_2 discharge annually during this timeframe in comparison to an annual SO_2 discharge of 3.5 million tons for the entire United States (Samuel N. Linzon, 1971). In the studies' 9 regions of interest lying to the northeast, southwest, west and east of Sudbury and ranging from 19-110 miles away from the city, areas closer to and to the northeast of Sudbury sustained the greatest damage from SO_2 gas emissions. The damage zones identified in these studies were divided into 3 typically elliptical areas and have been used in subsequent studies to delineate damage to areas from any pollutant gas: "Denuded or Total Kill," closest in proximity to the emission source and in the direction of typical wind direction, in which acute injury causes the death of trees, a "Transition or Heavy Kill" zone surrounding the

Denuded/Total Kill zone in which chronic injury effecting mainly the leaves or needles of trees is observed and a "Light Injury" sector surrounding the Transition/Heavy Kill zone in which minor chronic injury is noted (Knabe, 1976).

Unfortunately, in addition to its role as a primary gaseous pollutant, as SO_2 is oxidized by water vapor in the air, it produces sulfuric acid and becomes entrenched in the heavily moisture laden clouds which then fall as a secondary pollutant, acid rain (Dingman, 2008). The effects of acid rain are even more widespread than the effects from SO_2 gas emissions due to acid rain's ability to be readily transported with frontal systems spanning hundreds to thousands of miles. Once acid rain has fallen, it is responsible for depletion of forest growth through the acidification of soil that leads to a leaching of primary cations needed for tree growth such as calcium (Dingman, 2008).

Climate

Conjecture regarding the connection between volcanic eruptions and climatic changes has been recorded for over 2000 years with the works of Plutarch and Benjamin Franklin suggesting that volcanic eruptions "dimmed the sun" and caused a reduction in surface temperature. However it wasn't until the 20^{th} century that the link had been proven by a host of climate and volcanic scientists (Robock, 2000). Sulfur dioxide, while being only a trace gas in Earth's atmosphere comprising less than 1 ppm, was found to play a substantial role in climate change both at local and global levels.

Locally, sulfur dioxide causes a cooling effect in the troposphere, buffering temperatures from escalation by preventing absorption of incoming solar radiation through scattering (Robock, 2000). Keeping in mind that sulfur dioxide has a residence time of days to a few weeks in the troposphere, is easily transported by wind and readily combines with water to produce H_2SO_4 and other sulfates, these climatic changes are typically not significant enough to cause widespread destruction to crops, grazing land and other vegetation when emitted by volcanically violent eruptions. However, continual emissions described in the section above related to fossil fuel plants, smelting operations and repeated passive degassing can significantly harm vegetation residing in the downwind direction of the source (Knabe, 1976; Samuel N. Linzon, 1971). This is further compounded when heavily vegetated areas become depleted, local climate changes will ensue with issues such as soil erosion, heavier runoff of precipitation and avalanche control through the efforts of forest breaks being affected (Knabe, 1976).

In contrast to tropospherically-bound SO_2 emissions, stratospheric emissions have a far longer residence time of months to years, where they produce climatic changes on a global scale (S. A. Carn et al., 2007; Robock, 2000; Thomas & Prata, 2011). Sulfur dioxide residing in the stratosphere scatters incoming solar radiation, trapping the heat within this atmospheric layer and further preventing solar radiation from reaching the troposphere, which exacerbates the cooling effect described in the paragraph above. An illustration of this change in flux is seen below in Figure 6 from Robock, 2000. With

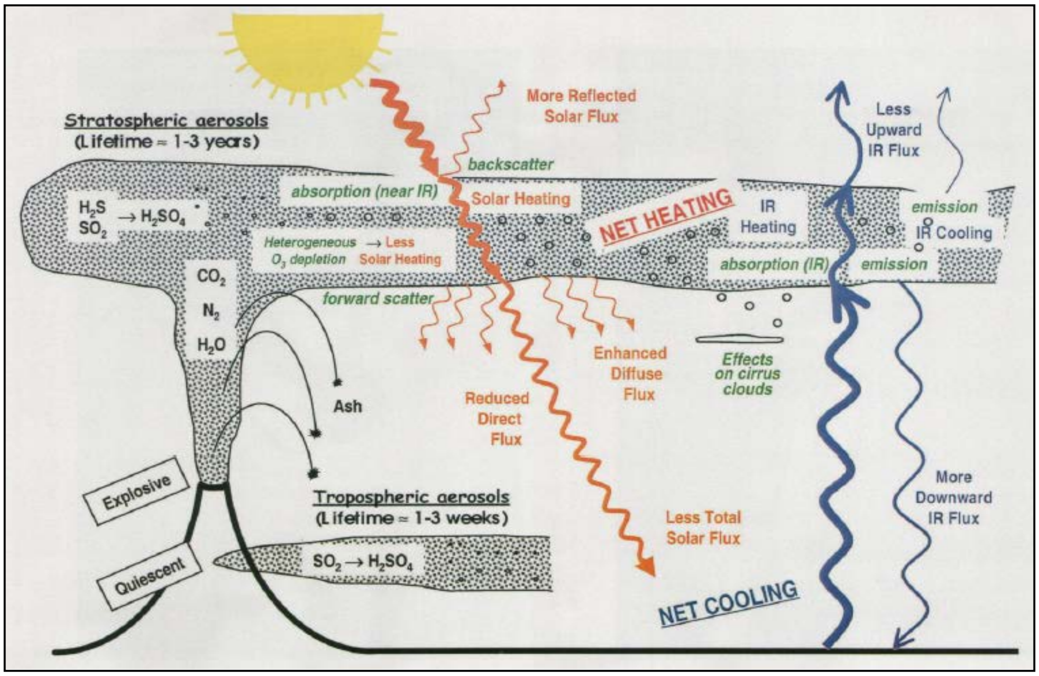

Figure 6: Changes to atmospheric flux as a result of volcanic eruption from Robeck, 2000.

large scale eruptions such as Mt. Pinatubo in June, 1991, a minimum estimation of 17 megatons (Mt) of sulfur dioxide was released into the stratosphere, where it resided for over 18 months and produced a net global temperature decrease of 0.5 K (Gerlach, Westrich, & Symonds, 1996; Soden et al., 2002). Additionally, with this eruption a secondary correlation was discovered; water vapor concentrations decreased in the atmosphere by 3% leading to a cooler, drier global climate in 1992 (Soden et al., 2002). An even more stark example of the consequences of such eruptions are the June-July 1783 fissure eruptions of Laki in Iceland that released 92 Mt of gas and changed the climate so dramatically that summer pastureland was annihilated leading to the loss of

79% of the island's sheep, 76% of the horses and 50% of the cattle (Grattan & Brayshay, 1995)

Aviation

In addition to the deleterious effects of sulfur dioxide to the health of humans, animals, vegetation and climate, SO_2 emanating from volcanic eruptions has also recently been recognized as a hazard to aviation. From 1953-2009, airlines logged 94 flights that were impacted by encounters with volcanic ash and SO_2, and 40 of those impacted flights occurred in 1991 following the VEI level 5-6 eruption of Mt. Pinatubo (Bluth, Doiron, Schnetzler, Krueger, & Walter, 1992; Prata & Tupper, 2009; Thomas & Prata, 2011). Additionally, the 2010 eruption of Iceland's Eyjafjallajökull volcano grounded all air traffic to and from northern Europe from 16-21 April, causing an estimated $4.7 billion in revenue losses (Read, 2011)

As aircraft fly through volcanic ash and gaseous clouds, the blend of sharp rock fragments, molten mineral material, glass shards and the reaction of SO_2 and OH to form sulfuric acid (H_2SO_4) can inflict damage to the aircraft fuselage, craze aircraft windows impairing pilot visibility, and clog jet engines leading to power failure (Simon A. Carn, Krueger, Krotkov, Yang, & Evans, 2009; Prata & Tupper, 2009). During active volcanic eruptions, volcanic ash is propelled into the upper troposphere and lower stratosphere portions (UTLS) of the atmosphere in tandem with volcanic volatile gases such as H_2O, CO_2 and SO_2. Unfortunately, volcanic ash, H_2O and CO_2 are not easily detectable in the UV portion of the electromagnetic spectrum, making it difficult for satellite-based sensors to track ash and gas clouds as they migrate globally. Keeping in mind that over

80% of Earth's annual volcanic eruptions attain a plume height of 6,000 m, 60% reach a plume height of 10,000 m and roughly 20% extend into the stratosphere at heights greater than 15,000 m, the vast majority of volcanic eruptive material inhabits the UTLS, where Earth's natural jet streams typically lie (Carn et al., 2009; Cordelia Maerker et al., 2008). This is particularly dangerous to the aviation community, as most commercial air flights occupy the air space of 9,000-11,000 m during the cruising portions of their flights to take advantage of the fuel savings and expedient winds offered by jet streams (Carn et al., 2009). Furthermore, as volcanic ash and gases travel through the atmosphere, they are quickly transported via Earth's atmospheric convection both vertically and horizontally, spreading over the globe in as little as two weeks. Current aircraft radar, meteorological and visual systems do not have the ability to identify volcanic ash and gases, and when considered in tandem with the approximate 5% annual global growth in aviation traffic, the need for policies and systems that can accurately assess and track the danger of volcanic ash and gas clouds is significant (Simon A. Carn et al., 2009; Prata & Tupper, 2009).

Fortunately, SO_2 is easily detectable in the UV, using highly sensitive remote sensing instrumentation like the Ozone Mapping Instrument (OMI), which is further described in the next section on Remotely Sensing Sulfur Dioxide. Due to SO_2's easy detectability, it is frequently utilized as a proxy for volcanic ash in determining whether air traffic should be rerouted or grounded. Sulfur dioxide is a hazard to aircraft in its own right. As gaseous-rich magma enters the atmosphere, it expands releasing heat into the atmosphere. As it strives to reach equilibrium with atmospheric conditions, it freezes and fractures as it cools (A. Krueger, Carn, Krotkov, Serafino, & Vicente, 2008). Once this material enters aircraft engines, it clogs turbine cooling passages causing overheating along with engine damage due to erosion of the turbine blades' coating (Grindle & Burcham, Jr., 2002). Additionally, once SO_2 reacts with the OH radical to form sulfuric acid, acid erosion of the aircraft's windows and fuselage can result in damage as minor as paint erosion and window scratches during brief exposure times in dilute conditions to airframe corrosion to significant visibility loss and ventilation issues if the exposure time is extensive or the concentration exceeds 10 Dobson Units (DU) (Simon A. Carn et al., 2009b). In many ways SO_2 can be more destructive than volcanic ash over the longer term due to SO_2's longer residence time in the atmosphere. Volcanic ash falls out of the eruptive plume more readily as a result of its higher mass and density or separation from the gaseous components via wind shear, leaving the more buoyant SO_2 to drift in the atmosphere (Thomas & Prata, 2011). As discussed in the previous section, SO_2 has a residence time of days to months depending on its altitude in the atmospheric column and the humidity levels present within the parcel, resulting in the need for vigilant tracking of SO_2 clouds in the atmosphere.

For these reasons, the International Civil Aviation Organization (ICAO) divided Earth into 9 regions and created a Volcanic Ash Advisory Centers (VAACs) in each region to track volcanic eruptions and mitigate aviation issues through the development of procedures regarding flight rerouting, grounding and tactics pilots should employ during encounters with volcanic ash/gaseous clouds (Prata & Tupper, 2009; Thomas & Prata, 2011). Figure 7, below illustrates the VAAC regions (Read, 2011).

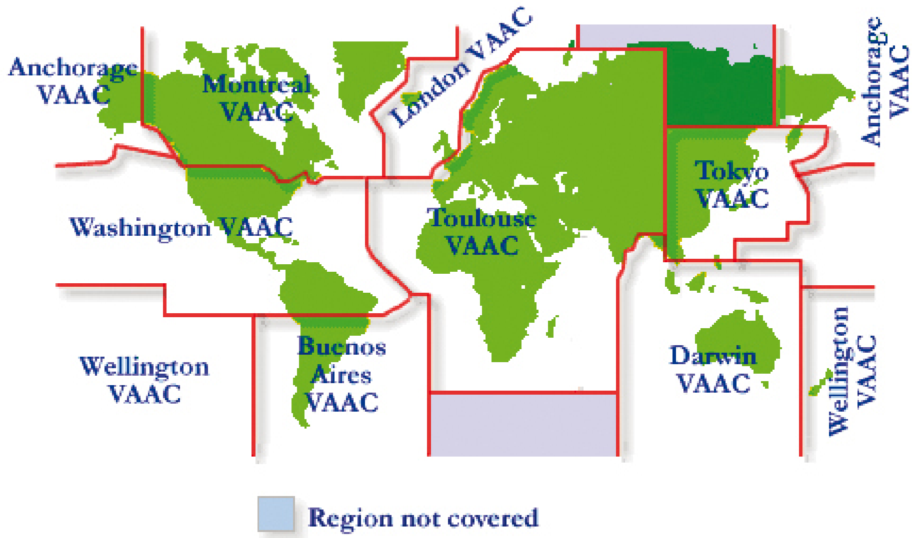

Figure 7: Volcanic Ash Advisory Centers regional divisions (Read, 2011).

These VAACs are co-located with a country's meteorological facilities allowing for the seamless integration of weather conditions and forecast model information with satellite remote sensing data to accurately predict ash and gas cloud transport throughout the atmosphere. With passive SO_2 emissions being a precursor to an active emission, it is vitally important for the VAACs to continue following not only active eruptions, but to also utilize satellite remote sensing data to track passive emissions as indicators of impending volcanic activity that can disrupt air travel. Following the 2010 eruption of Eyjafjallajökull volcano in Iceland, the ICAO enacted stricter guidelines that correlate ash concentration to flight operations, with less than 2×10^{-3} g/m^3 deemed safe for aviation, 2-4 x 10^{-3} g/m^3 safe under certain conditions and emissions greater than 4×10^{-3}

g/m^3 grounding air travel (Thomas & Prata, 2011). In their continued mission to ensure the safety of global aviation, these guidelines will continue to be revised as further testing results in better data regarding SO_2 and volcanic ash hazards to the industry.

Remotely Sensing Sulfur Dioxide

Prior to the 20th century, the human nose was considered the primary method of detecting sulfur dioxide (SO_2) emissions in the air. Although a colorless gas, SO_2's pungent smell similar to that of a freshly struck match make it easily detectable to those in close proximity to a source. (Faivre-Pierret & Le Guern, 1983)Once sulfur dioxide is released via eruption or anthropogenic activity, remote sensing instruments detect it via its characteristic spectral features. SO_2 displays greater than 95% absorbance at 310.80 nm, roughly 65% absorbance at 313.20 nm and has troughs of less than 35% absorbance at 311.85 nm, 312.61 nm and 314.40 nm. These characteristics distinguish it from the ozone (O_3) molecule, which shows a steadily declining absorption from 25% at 310 nm to almost no absorption at 325 nm. This dramatic difference in spectral signature allows for ease in distinguishing the presence of SO_2 in an image from ozone. These spectral features are seen below in Figure 4 (Yang et al., 2007).

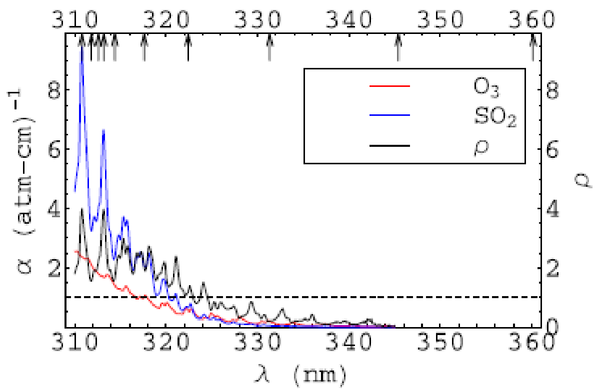

Figure 8: Spectral absorbance curves of SO2 (blue), O3 (red) and the ratio of SO2 to O3 (black) illustrating the unique spectral properties of SO2 (Yang et al., 2007).

The significance of separating the spectral signatures of ozone from SO_2 lies in the development of instrumentation to detect ozone in the atmosphere following the discovery of holes in the polar regions of the ozone layer. Once discovered, the scientific community propelled this issue to the forefront of research with governments devoting time and financial backing for advanced satellite UV sensors to monitor ozone flux. These sensors were then proven to be even more valuable in their ability to remotely detect other spectral signatures such as sulfur dioxide, nitrogen oxides (NO_x), hypobromite (BrO), chlorine dioxide (OClO or ClO_2) and formaldehyde (CH_2O) which also furthered our understanding of the relationship between volcanic gases and Earth's atmosphere (Khokhar et al., 2005).

Remote Sensing Instrumentation of SO_2 Emissions

With the rapid advance of technology and increased population density of areas lying near active volcanoes, the need for a better understanding of the dynamics associated with volcanism and development of early warning systems to evacuate those population centers led to the creation of ground-based UV sensor technology in the 1970's to measure gaseous emissions emanating from volcanic peaks. Beginning with the ground-based Brewer and Correlation Spectrometers (COSPEC), scientists were able to capture quantifiable measurements of SO_2 degassing at several sites including Mt. Etna, Italy, Kilauea, Hawaii (US), Mt. Erebus, Antarctica, Arenal, Costa Rica and Masaya, Nicaragua (Stix, Williams-Jones, & Hickson, 2008). By the late 1970's, satellite remote sensing technology began to allow for much larger spatial coverage of atmospheric phenomenon, and with the launch of the Total Ozone Mapping Spectrometer (TOMS) in 1978 a new chapter began in Earth's atmospheric observation. Following TOMS' surprising detection of SO_2's spectral signature obscuring ozone observations in the UV/VIS portion of the spectrum near the El Chichon volcano in 1982, instrumentation has become increasingly more sophisticated in discerning the role that SO_2 in particular, plays in atmospheric chemistry (A. J. Krueger et al., 1995). Based on this discovery, instrumentation then focused on higher resolution and more frequent temporal collection of UV/VIS space-borne data, utilizing the UV/VIS technological improvements to develop smaller and lighter ground-based portable sensors, and harnessing SO_2's characteristics in the thermal IR portion of the spectrum to further verify and quantify SO_2 emissions (Doutriaux-Boucher & Dubuisson, 2009; Bo Galle et al., 2002; Watson et al., 2004). All of these advances have led to a record of SO_2 emissions spanning from 1979-present, with increasing focus on detailed studies of specific volcanoes, power plants and smelting operations (Arellano et al., 2008; Bani et al., 2012; Burton et al., 2009; Carn et al., 2008; Carn et al., 2007; Igarashi et al., 2004).

Ground Based Ultraviolet Detection

COSPEC

With the development of the Correlation Spectrometer (COSPEC) in 1971, scientists had their first remote sensing tool that allowed them to directly measure sulfur dioxide emissions via the spectral signature shown above in Figure 8 through mask correlation spectroscopy. Mask correlation spectroscopy in the COSPEC device compared the "molecular absorption spectrum of a gas and an optical correlation mask used as a fingerprint of the gas under investigation" (Giovanelli, Tirabassi, & Sandroni, 1979). Only a few of the key absorption bands are calibrated and used in the comparison to identify the gas being studied, which represents a small portion of the full spectra.

Originally developed as a monitoring instrument for industrial and chemical plants to determine SO_2 and NO_2 emissions, the COSPEC device quickly became the standard tool for also measuring volcanic SO_2 fluxes (Galle et al., 2002). The portability of COSPEC made it invaluable in its usage both in measuring volcanic emissions and in tracking pollutants from fossil fuel consumption and smelting operations, for it could be mounted in aircraft, automobiles, on tripods and in factories. For over 30 years, the COSPEC device has been the most widely utilized piece of equipment in remotely sensing SO_2 emissions and continues to be in use today both as an SO_2 sensor and more importantly as an instrument to corroborate UV satellite SO_2 emission data.

One example of the COSPEC's longevity is in its measurements at Stromboli, which began in 1975. Through successive, sporadic measurements over the period from 1975 until 2002, scientists were able to track the flux of SO_2 released from Stromboli, which illustrated the volcano's pattern of mostly passive degassing punctuated by eruptive events (Burton, Caltabiano, Mure, Salerno, & Randazzo, 2009). In contrast to this pattern, COSPEC also illuminated the unique degassing patterns of several other volcanoes, including Mt. Etna, Mt. St. Helens, Mt. Pinatubo, Galeras, Redoubt, El Chichon, Arenal, Masaya, Nevado del Ruiz and Augustine, which showcased its greatest achievement – the ability to delineate degassing patterns of a volcano and allowing the accumulation of that knowledge to discern Earth's annual SO_2 budget as well as begin the process of predicting volcanic eruptions. As each crater demonstrated its own set of degassing characteristics, with some like Stromboli showing mostly passive degassing cycles in contrast to craters like Galeras that showed sudden decreased SO_2 gas levels just prior to eruptive onset, scientists began to understand the eruptive causes of the volcano in question and link this data to measured COSPEC SO_2 output (Stix et al., 2008).

While being an incredibly useful instrument for understanding the SO_2 output of particular volcanoes, COSPEC did have a number of criticisms. The instrument itself weighed in at a bulky 20 kg, needed 23 W of power and was not designed for the rugged topography of volcanic landscapes (Nadeau & Williams-Jones, 2008). It required repeated verification measurements with each positioning either at the volcanic source or on an aircraft for aerial reconnaissance, and could not be deployed during active eruptions, as this situation posed too much of a danger to COSPEC's users and the equipment. Additionally, its cost of 60,000 USD with further funding needed for servicing and maintenance costs made it unattainably expensive for many researchers to purchase (Galle et al., 2002). For those who were able to purchase the instrument, data was not available in real time and required algorithmic processing to exclude spectral interference sources, solar Frauenhofer lines, and the removal of multiple scattering and polarization effects from clouds and aerosols. Nevertheless, COSPEC was the first UV instrument to measure SO_2 degassing from volcanoes, and its use ushered in a flurry of additional devices that would dramatically improve upon its achievements.

Mini-DOAS

Toward the close of the 20th century, computer chips had become more powerful and slighter in footprint, allowing for “a smaller, cheaper, more robust alternative to the COSPEC, while also improving several factors in the data collection methodology and offering the opportunity for a wider range of field applications” (Nadeau & Williams-Jones, 2008). By the early 21st century a new type of sensor based on differential optical absorption spectroscopy (DOAS) was developed to harness technological advances that occurred over the previous 30 years. Differential optical absorption spectroscopy differs from the mask correlation spectroscopy used in the COSPEC device by its application of the full range of wavelengths in SO_2’s spectral signature. Called the Mini-DOAS, this new sensor weighed less than 1 km, required only 1 W of power through its USB port connection to a laptop computer and was one-tenth the size and cost of COSPEC (Nadeau & Williams-Jones, 2008). In parallel use with COSPEC, the Mini-DOAS device offered more accurate emissions measurements due to output illustrating a spectrum versus COSPEC's output of simple columns amounts of gas, now making it the undisputed choice in ground based spectroscopy (Galle et al., 2002).

Use of the Mini-DOAS has become far more widespread than COSPEC, for the reasons stated above, which has given scientists the ability to study a greater number of volcanoes. Specifically, efforts at Soufrière Hills, Montserrat and Volcán Masaya, Nicaragua showed vast improvement in accuracy, reduction in error to within 10% and provided near real time (less than 5 minutes) data delivery due to its use of the full UV spectrum in determining SO_2 values coupled with the ability for faster computational analysis as technology has advanced (Galleet al., 2002). Additionally, Mini-DOAS has the ability to measure faint fluxes in SO_2, which was not available with COSPEC. In the ten years since this introductory evaluation, use of the Mini-DOAS has progressed to involve deployed networks of these sensors, having the ability to continuously take measurements of volcanic degassing activity (Nadeau & Williams-Jones, 2008).

As advanced as the Mini-DOAS instrument has become, like COSPEC it is still hampered by the need to traverse dangerously active volcanic areas, is susceptible to higher error in hazy conditions and only has the ability to measure one volcano's activity (B. Galle et al., 2005). Additionally, measurements of plume velocity and plume height are also areas of uncertainty with typically high error rates requiring substantial technique refinement to correct (Johansson et al., 2009). However, like its predecessor COSPEC, Mini-DOAS is also useful in corroborating satellite-based measurements, ensuring improved accuracy and precision in measuring SO_2 gas emissions.

Satellite Ultraviolet Detection

In 1978, a new era began with the launch of the TIROS-N satellite with the Total Ozone Mapping Spectrometer (TOMS) in its payload. Although TOMS was not designed with the primary objective of measuring SO_2, instead its mission was to observe and map global ozone amounts as well as collect weather pattern data (NOAA Satellite Services Division, n.d.; Spector, 2007). However, this instrument would inaugurate the field of satellite SO_2 monitoring, initiating development of a whole host of other satellites, listed below in Table 2.

Table 2: History of Satellite Remote Sensing Devices Detecting SO2 (Brill, n.d.; Ernst, Kervyn, & Teeuw, 2008; Hoff & Christopher, 2009; Maccherone, n.d.)

Years	Satellite	Instrument	Instrumentation	Spatial Resolution	Orbit
1978-1991, 1991-1994, 1996-2006 1996-1997	Nimbus-7, Meteor-3, TOMS-EP, ADEOS	N7-TOMS, M3-TOMS, TOMS-EP, ADEOS-TOMS	UV	50x50 km	Polar
1995-present	ERS-2	GOME	UV, VNIR	320x40 km	Polar Sun-Synchronous
2003-present	Aura	OMI	UV, VIS	13x24 km, 13x12 km	Polar Sun-Synchronous

2006-present	CALIPSO	CALIOP	LIDAR	125m	Polar Sun-Synchronous
2007-present	METOP	GOME-2	UV, VIS	80x40 km	Polar Sun-Synchronous
2007-present	Envisat	SCIAMACHY	UV, VIS, VNIR	60x30 km	Polar Sun-Synchronous
2011-present	NPP	OMPS	UV, VNIR	50x50 km	Polar Sun-Synchronous

.

Satellite detection methods allowed for observation of SO_2 clouds on a regional, continental and global scale in comparison to the point by point analysis conducted with COSPEC and Mini-DOAS equipment. Krueger et al., noted this in their paper, stating "Conventional petrologic estimates of SO_2 release in explosive eruptions were found to be low by an order of magnitude when satellite data became available" (2009).

TOMS

The Total Ozone Mapping Spectrometer (TOMS) was launched in 1978 "to determine the spatial structure in the total ozone through daily, contiguous mapping of the earth"(A. Krueger, Krotkov, & Carn, 2008). Through 6 specific UV wavelengths between 310-380 nm, it covered a 2,795 km swath at a spatial resolution of 50x50 km (Ernst, Kervyn, & Teeuw, 2008). In 1982, TOMS reported exceedingly high readings of ozone over Mexico following explosive eruptions of the El Chichón volcano, which were hypothesized as and later determined to be SO_2 emissions after algorithms were written to separate the similar ozone and sulfur dioxide spectral signatures illustrated in Figure 4. This event initiated satellite remote sensing of atmospheric SO_2, with TOMS' mission expanded to include these explosive, volcanic-sourced SO_2 releases resulting in the application of SO_2 algorithms to previously collected data. Once implemented, the algorithms provided a now 30-year continuous record of the global SO_2 emissions needed to calculate the total sulfur budget as well as delivering information on the eruption activity of specific volcanoes (A. Krueger, Krotkov, et al., 2008).

Following the El Chichón eruption, TOMS became the standard satellite instrument for measuring SO_2 emissions from volcanoes. Over the course of its 3 missions, it accumulated data from 1978-2005 on 61 volcanoes worldwide with only one hiatus from 1994-1996 between the failure of M3-TOMS and the launch of the EP-TOMS/ADEOS-TOMS missions. M3-TOMS itself was a stunning collaboration at the end of the Cold War period between the United States and the Soviet Union with the M3-TOMS satellite made by NASA launched on a Soviet rocket. To date, the information collected by the four TOMS missions continues to be used by the scientific community and is responsible for better predictive behavior of erupting volcanoes and for SO_2 cloud tracking needed to produce aviation hazard assessments (S. Carn et al., 2003).

As with the COSPEC instrument, TOMS inaugurated a new chapter in SO_2 measurement, upon which subsequent instrumentation improved. Although TOMS was developed to image ozone, development of algorithms allowed for expanded usage of SO_2 emissions (S. Carn et al., 2003). Because TOMS is a passive remote sensor, it requires sunlight to provide the photon source necessary for SO_2 measurement, so night measurements are impossible. Additionally these SO_2 measurements are integrated over a column of gas, thus requiring additional information from ground sources or other satellites utilizing other areas of the electromagnetic spectrum to determine plume height.

The primary issues with TOMS were multiple instrument failures, beginning with M3-TOMS prematurely failing only three years after its launch and causing a 2 year gap in data between 1994 to 1996 (S. Carn et al., 2003). To provide both high sensitivity and spatial coverage, two TOMS satellites were launched in 1996. TOMS-EP was to fly at a low orbit, producing higher sensitivity images with a smaller footprint of 24 x24km, while ADEOS-TOMS provided global coverage. Unfortunately ADEOS-TOMS failed after only one year of operation, so TOMS-EP's orbit was increased to provide 39 x 39km images and giving scientists the global coverage of ADEOS-TOMS. A fifth TOMS satellite, QuikTOMS failed to achieve orbit after its 2001 launch, thus bringing an end to the TOMS program. Despite these failures, the TOMS program ushered in a new era of satellite UV remote sensing of atmospheric aerosols, leading to the following programs outlined below.

GOME

Following the success of the TOMS multispectral mission, the European Space Agency (ESA) launched the Global Ozone Monitoring Experiment (GOME) in 1995 to further both ozone and SO_2 mapping as the first UV hyperspectral sensing satellite. GOME provided "a twenty-fold improvement in SO_2 sensitivity over TOMS" through the integration of a DOAS algorithm that allows trace gas detection at weaker levels than

TOMS could distinguish (A. J. Krueger et al., 2009). Overall, GOME was an important advancement due to its ability to detect not only volcanically emitted sulfur dioxide, but also for detection of sulfur dioxide emitted as air pollution from fossil fuel consumption, for the first time.

GOME continued to catalog data on 20 active volcanoes from 1996-2002, including Bandai Honshu, Japan, Central Islands, Vanuatu, Piton de la Fournaise, Reunion Island, France, the Kamchatka region of Russia and remote portions of Indonesia that were previously unstudied due to their isolated locales. GOME was crucial in providing a catalog of information at these sites in a format consistent with that of TOMS data, which became instrumental in the development of evacuation and flight planning near these regions. In addition to these remote locations, GOME's data on Nyamuragira, Etna, Popocatepetl, Kilauea, Hekla and Tungurahu was compared with and validated by TOMS findings. Extending beyond TOMS' spectral resolution, GOME was the first satellite to identify anthropogenic sources of SO_2 in the eastern United States and Europe, and over portions of South Africa, China and Russia, providing quantitative information on emissions levels of fossil fuel consumption at power plants and smelting operations (Khokhar et al., 2005).

Like TOMS, GOME was a passive remote sensor with the ability to only conduct daytime measurements and continued to be hampered by issues with cloudy conditions, aerosol scattering effects and the inability to determine plume height (Khokhar et al., 2005). Although the spectral sensitivity of the instrument improved over TOMS, the spatial resolution remained course at 320 km x 40 km and had a far narrower swath width of 960 km (Ernst et al., 2008). Temporally, GOME also took longer to provide full planetary coverage in comparison to TOMS, with GOME needing a 3 day span over TOMS' daily coverage (Khokhar et al., 2005).

OMI

The Ozone Monitoring Instrument (OMI) became the premier instrument for SO_2 detection following its 2003 launch. With its daily global coverage, spectral resolution of 0.45nm, spatial resolution of 13 km x 24 km at nadir and a swath width 2795 km, it images most of Earth's volcanoes to produce detailed records of both eruption activity and passive degassing and continues the record catalog originating with the TOMS satellites and can be freely accessed via the internet at the NASA Global Sulfur Dioxide Monitoring Home Page or the Goddard Earth Sciences Data and Information Services Center's Giovanni program. Figure 9: OMI imaging track for 24 March, 2013 below provides the imaging path of OMI for 24 March 2013.

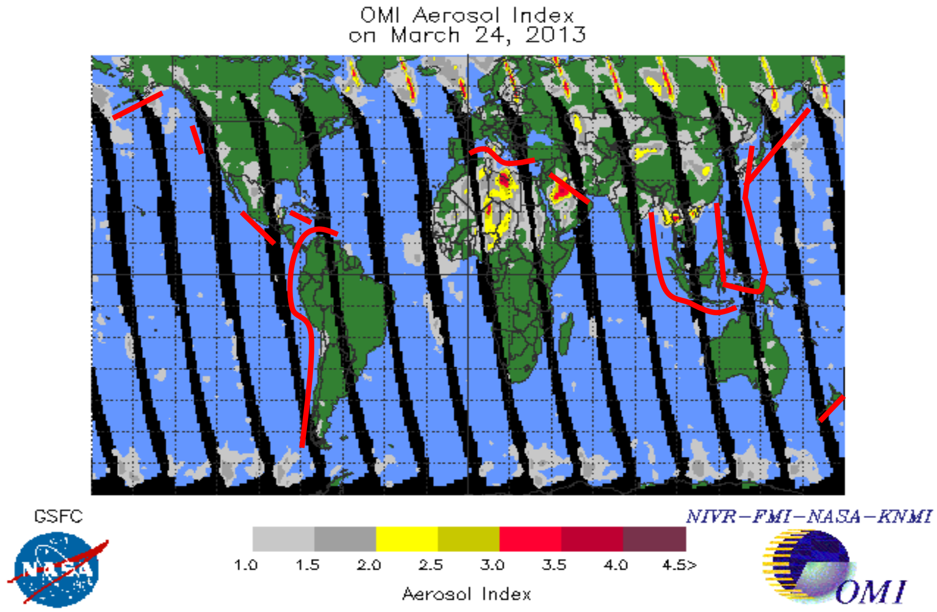

Figure 9: OMI imaging track for 24 March, 2013, with convergent plate boundaries represented by red lines (McPeters, 2013).

Additionally, OMI has the capacity to detect even smaller sources with a 26 ton detection limit, bettering GOME-2's 360 ton limit and TOMS 7,000 ton limit due to its 13 x13 km zoom capability (Carn et al., 2007). This coupled with OMI's lesser retrieval noise allows for monitoring of anthropogenic SO_2 emissions with unsurpassed detail from large sources such as fossil fuel burning power plants to smaller sources like smelting plants and forest fires. An example of an OMI image is shown below in Figure 10, illustrating a gaseous plume originating from an eruption of Mt. Etna on 4-March 2012 (Krotkov, 2012). Mt. Etna is represented by the triangle on the island of Sicily to the SW of mainland Italy, and the plume has streamed to the NNE over the Ionian Sea.

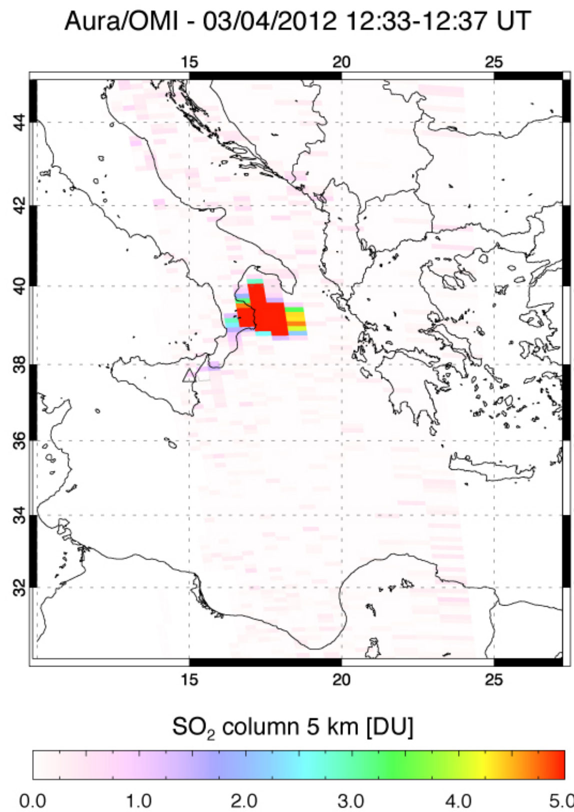

Figure 10: OMI image of gas plume originating from Mt. Etna (Krotkov, 2012)

OMI accomplishes its ability to detect both large and small scale SO_2 emission events through the use of two key algorithms, the linear fit method (LF) for full spectral measurements at altitudes between the UTLS and lower troposphere and the band residual difference (BRD) algorithm for highly sensitive measurements of smaller sources at the Planetary Boundary Layer (PBL) (NASA/Goddard Space Flight Center, 2012; Yang et al., 2007). For general volcano monitoring of active craters such as Nyamuragira, Democratic Republic of Congo and Soufriere Hills, Montserrat, the linear fit methodology provided error rates of less than 20% in estimating the emission amount, tending to underestimate the quantity if the emission exceeded 100 Dobson Units (Yang et al., 2007). In contrast, the BRD algorithm's use in determining emissions from Peruvian copper smelting operations in Ilo and La Oroya resulted in estimates of 0.07 Tg ± 0.03 Tg (Simon A. Carn, Krueger, Krotkov, Yang, & Levelt, 2007).

The largest disadvantage to OMI in addition to the traditional issues already expressed with passive UV remote sensing technology is decreased imaging performance from nadir as the side scanning spatial footprint increases, making it a less effective tool at high latitudes (A. J. Krueger et al., 2009). In Figure 9, this manifests itself as the parallel lines of aerosol seen in the high northern latitudes. Polar volcanoes such as Mt. Erebus in Antarctica and some in high latitudes in the Pacific Ring of Fire cannot be assessed as accurately compared to those at lower latitude. Lastly, OMI images suffer from two types of defects: white clouds and diagonal lines. The white clouds seen below in Figure 11(a) are "produced when upper level troughs (high total ozone) amplify and extend across the ozone profile climatology boundary between middle and high latitudes" thus generating the white clouds as "false residuals" (NASA/Goddard Space Flight Center, 2012). The diagonal lines trending in a NNW to SSE direction seen in Figure 11(b) are artifacts of the data gathering process and do not represent sulfur dioxide emissions.

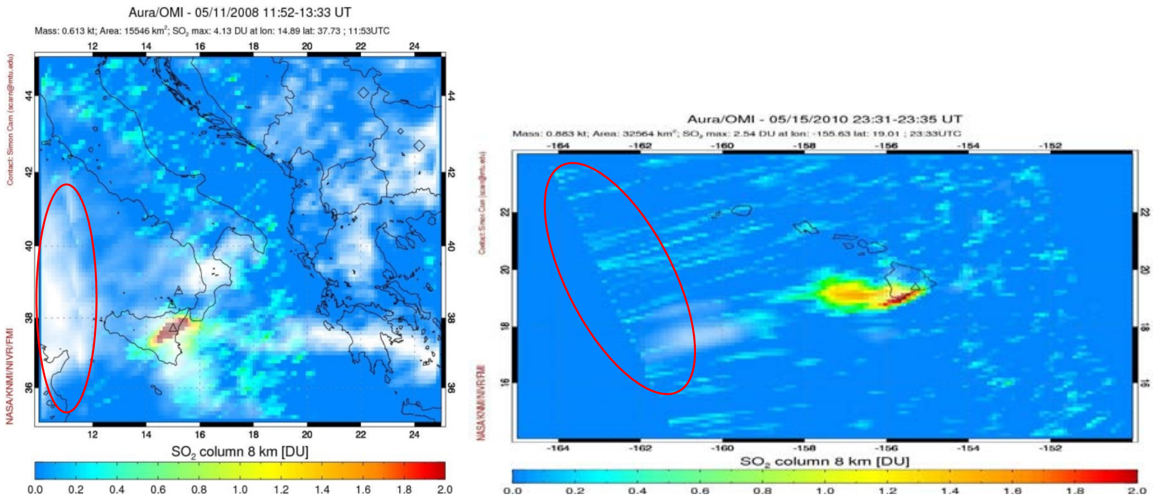

Figure 11: (a) on left, is an OMI image of Italy. The red oval on the left side shows an example of white cloud artifacts and (b) on right is an OMI image of Hawaii. The red oval on the left side of this image shows an example of diagonal line artifacts.

CALIOP

In contrast to the other remote sensing satellites discussed above, the Cloud and Aerosol Lidar with Orthogonal Polarization (CALIOP) instrument is an active sensor that uses laser pulses to determine aerosol cloud altitude. It measures this elevation via backscatter measurement, which compares aerosol absorption measurements to the extinction of those measurements to produce a height profile of the emission (Hoff & Christopher, 2009). Another differentiating factor between CALIOP and the other satellites in this paper is that CALIOP works in the radar portion of the spectrum allowing it to make measurements during the day, night and in the midst of cloudy conditions, whereas the other satellite instruments utilize the UV, visible and infrared portions of the electromagnetic spectrum. These UV-VIS-IR satellites are able to readily identify aerosol constituents within an emission, but their values are integrated over the entire column's depth making it difficult to determine the cloud height. Like OMI data, CALIOP data can be freely accessed via the internet through the Goddard Earth Sciences Data and Information Services Center's Giovanni program. An example of CALIOP's output is seen below in Figure 12, with color coded cloud types cross-sections displayed on a latitude/longitude x-axis and altitude on the y-axis.

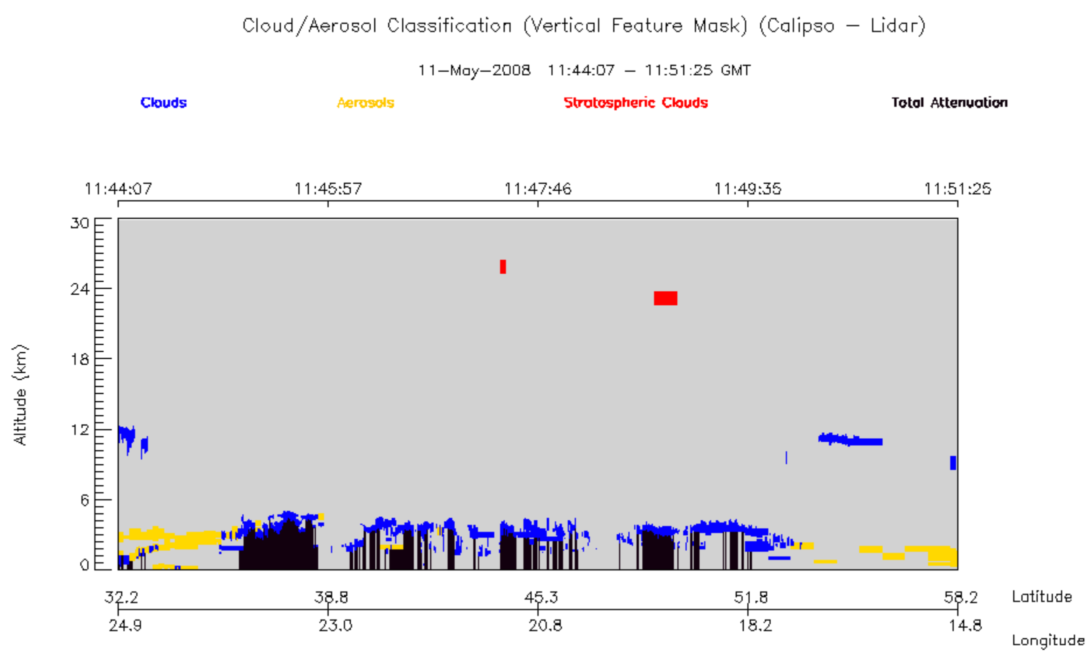

Figure 12: CALIOP Lidar output image at specific latitude/longitude coordinates, with blue illustrating cloud height, yellow showing aerosol height, and red delineating stratospheric cloud altitude (Kempler, 2008).

When CALIOP plume height measurements are used in tandem with UV-VIS-IR latitude and longitude data, the resulting 3D profile of SO_2 emissions can be integrated with meteorological data to produce a model of emission tracking from the source location to cloud dispersion, provided that the 60 km swath width crosses the emission

(Kristiansen et al., 2010; Winker et al., 2009; Yang et al., 2010). The largest issue thus far has been a slow leak in the pressurized energy system that empowers the laser, requiring the backup laser to be engaged for primary measurement (Hunt et al., 2009).

GOME-2

GOME-2, launched in 2007, continued to improve upon its UV remote sensing predecesors with far finer spatial resolution at dimensions of 80 km x 40 km and a wider swath width at 1920 km. Improving upon GOME's ability to provide early warnings of volcanic activity for both flight operations as well as evacuation planning on the ground, GOME-2 became particularly beneficial with effusive eruptions like Jebel al Tair in September of 2007 and Mt. Etna in May of 2008 (Rix et al., 2009). Tracing these emissions became critical in correctly routing aircraft around the gas clouds to avoid ash intake and corrosive SO_2 gas. GOME-2 along with OMI quickly became the most reliable resources for Earth's Volcano Ash Advisory Centers (VAACs) due to their combination of daily global coverage and highly detailed spatial resolution in providing detailed imagery of these emissions, which could then be combined with meteorologic information and fed into modeling programs such as FLEXPART and HYSPLIT (Rix et al., 2009). Additionally, GOME-2 's ability to perform limb observations allowed for polar imaging, which provided complete global coverage of SO_2 emissions (A. J. Krueger et al., 2009).

With GOME-2, the tradeoff for having better spatial and temporal coverage was a decrease in spectral resolution from GOME's 0.2-0.33nm to a coarser 0.26-0.51nm (Khokhar et al., 2005; Rix et al., 2009). To compensate for this, as well as the other typical issues with passive remote sensor technology of being able to only make measurements in unobstructed daylight, contending with aerosol scattering, and determining plume height, algorithms had to be written to eliminate noise and supplementary sensor information employed (Rix et al., 2009).

SCIAMACHY

The Scanning Imaging Absorption Spectrometer for Atmospheric Chartography (SCIAMACHY) also built upon GOME 's success with the additional capabilities of a finer spatial resolution of 60 km x 30 km, measuring wavelengths into the near-infrared (NIR) and being able to switch between stratospheric vertical profile measurement and nadir column views (A. J. Krueger et al., 2009; Richter, Wittrock, & Burrows, 2006). With a spectral resolution of 0.25 nm in the UV, it successfully imaged the Sierra Negra volcano in the Galapagos Islands during an October 2005 eruption as well as regional studies of the Middle East, China and North/Central America (Richter et al., 2006). In addition to the issues faced by the other UV sensors discussed in this paper, SCIAMACHY also has the drawback of decreased nadir coverage, due to the instrument having to dedicate equal time to both vertical profile measurement and nadir column views (Richter et al., 2006). Overall, SCIAMACHY has proven itself to be beneficial in extending the measuring capability of GOME as well as confirming observations made by GOME-2, but it lacks the spatial and temporal coverage of GOME-2 and OMI, requiring several days to obtain complete global coverage (Rix et al., 2009).

OMPS

The Ozone Mapper Profile Suite (OMPS) launched in 2011 is the latest addition to the UV satellite suite, which consists of a nadir mapper/profiler observing wavelengths between 250-380 nm and a limb profiler covering a wider range from 290-1000 nm (NASA, 2012). Its spatial resolution of 50 km x 50 km, swath width of 2600 km and daily coverage at nadir allow for complete, regular imaging of Earth extending catalogued measurements of SO_2 emissions from TOMS, GOME, OMI, GOME-2 and SCIAMACHY and allow for continued tracking of these emissions throughout the troposphere (NASA, 2012). After calibration, OMPS began to deliver products similar to OMI images in January, 2012. Due to the recent nature of its launch and operation, detailed studies of OMPS imaging of particular volcanoes or anthropogenic emissions are not currently available, but will be published in the near future.

While OMPS nadir viewing will cover Earth every 24 hours, it will take the limb profiler 4 days to complete full observations, so passive degassing emissions from high latitude volcanoes like Mt. Erebus, Antarctica will not have as complete of a record in comparison to those at lower latitudes with daily exposure. As with all other passive UV spectrometers reviewed in this paper, OMPS can only take measurements in daylight, preferentially in less cloudy environments and it continues to have issuess with aerosol scattering. Data derived from OMPS also does not include plume height, which needs to be discerned from other sensors such as CALIOP.

Transportation and Distribution Modeling Systems

There are several Transportation and Distribution (T&D) modeling systems widely used in the atmospheric sciences community to simulate the movement of aerosol gas clouds throughout the atmosphere. Once a gaseous emission has entered the atmosphere, it expands and disperses. Tracking the expansion and dispersion process is conducted through two types of methods: particle and puff. Particle tracking focuses on following individual molecules comprising the gas emission through time and space. Puff tracking instead "computes the trajectory of the mean particle position and the particle distribution" and assumes a "distribution shape (puff)" using a Gaussian curve or Top Hat approach (Draxler, 2004). In addition to accounting for the expansion and distribution of the gas parcel, T&D systems must also utilize either one of two types of atmospheric modeling methodologies or in tandem: Eulerian models and Lagrangian models. Eulerian models solve advection and diffusion movement on a fixed grid, which contrasts with Lagrangian models solving the advection and diffusion components as independent calculations (Draxler & Hess, 1998). Eulerian systems tend to work best in highly complicated emission scenarios, where solutions are required for each gridded point, but the scales for meteorological information as well as the emission source input data must be on the same scale as the model grid. Lagrangian systems have more flexibility in calculating solutions at any resolution for both particle and puff release methods, but require higher processing time to complete the independent advection and diffusion calculations (Draxler & Hess, 1998).

HYSPLIT

One of the many and most widely used T&D modeling systems in tracing gas emissions is The Hybrid Single Particle Lagrangian Integrated Trajectory (HYSPLIT) system, which combines the ability of particle tracking in the vertical direction with puff tracking in the horizontal direction (Igarashi et al., 2004). This methodology provides better accuracy of vertical dispersion while allowing for the expansion of gas “puffs” as the emission covers a greater spatial area and is freely accessible as either an internet driven package or a desktop package via the NOAA Air Resources Laboratory’s HYSPLIT home page (Draxler & Hess, 1998). HYSPLIT also demonstrates its robust capability by using both Lagrangian calculations of advection and diffusion, but placing them on a fixed grid of concentrations as used by Eulerian models, making HYSPLIT a “complete system for computing both simple air parcel trajectories and complex dispersion and deposition simulations” (Air Resources Laboratory, 2012; Draxler & Hess, 1998). Developed as a joint effort between the United States’ National Oceanic and Atmospheric Administration and the Australian Bureau of Meteorology, it provides results as accurate as rawinsonde data (Draxler & Hess, 1998).

HYSPLIT performs in both GUI-PC and web-based modes, each offering the same basic tools of concentration/dispersion and trajectory modeling. To begin using HYSPLIT, users are required to choose between the concentration/dispersion mode and the trajectory mode before entering data into the system. The concentration/dispersion mode takes into account atmospheric stability, atmospheric mixing and rate of dispersion to calculate and display gas amounts over a prescribed area, and can display both snapshot and animated simulations running in a forward or backward mode (Draxler & Hess, 1998). The trajectory mode also allows users to specify between forward and backward trajectory modes and can run for up to three latitude/longitude locations, three atmospheric elevations, and as either a normal (simple trajectory calculation from a specific latitude, longitude and elevation), matrix (multiple trajectories based on the farthest SW and NE coordinates with equal spacing between each trajectory run) or ensemble (multiple trajectories from each location) mode. Examples of outputs from the concentration/dispersion and trajectory modes are shown below in Figure 13.

Once the user has determined which type of mode to run, HYSPLIT then asks for meteorological inputs. These inputs are highly flexible, in that seven different meteorological data file types are available online for system integration or users are allowed to input meteorological data directly into the system as long as the required components of U and V (horizontal wind), T (temperature), Z (height), P (pressure), P_0 (surface pressure) are provided. It is also helpful if the user can input ground level winds and vertical motion (W, in units of pressure), although HYSPLIT has the ability to calculate these parameters, doing so greatly increases processing time (Roland R. Draxler & Hess, 1998).

Once these inputs have been selected, the user is brought to the Setup Model Run screen, where he/she can make further selections regarding whether to conduct the simulation in a forward or backward direction, the start time, the total run time, how often to start each trajectory. The lower half of the screen provides options for how the output will be displayed, such as the resolution, zoom, projection, labeling, type of output file and whether meteorological data should be added onto the trajectory display. HYSPLIT output files can be generated in the form of GIS Shapefiles, Adobe .pdf or Google Earth .kmz files, allowing them to be used in a wide variety of software programs for further analysis and presentation (Draxler, et al., 2009).

Once the user inputs all of their required options, the HYSPLIT program runs and delivers the results succinctly displayed in one image as seen in Figure 13 below (Draxler et al., 2009). All model types display results in variously sized latitude/longitude grids, such as 1^{o} x 1^{o} or 2^{o} x 2^{o}, which are calculated based on the size of the input coordinates and how far the gas parcel has traveled. In addition to the output displays, HYSPLIT creates a binary data file as output for integration into other programs (R. Draxler et al., 2009)

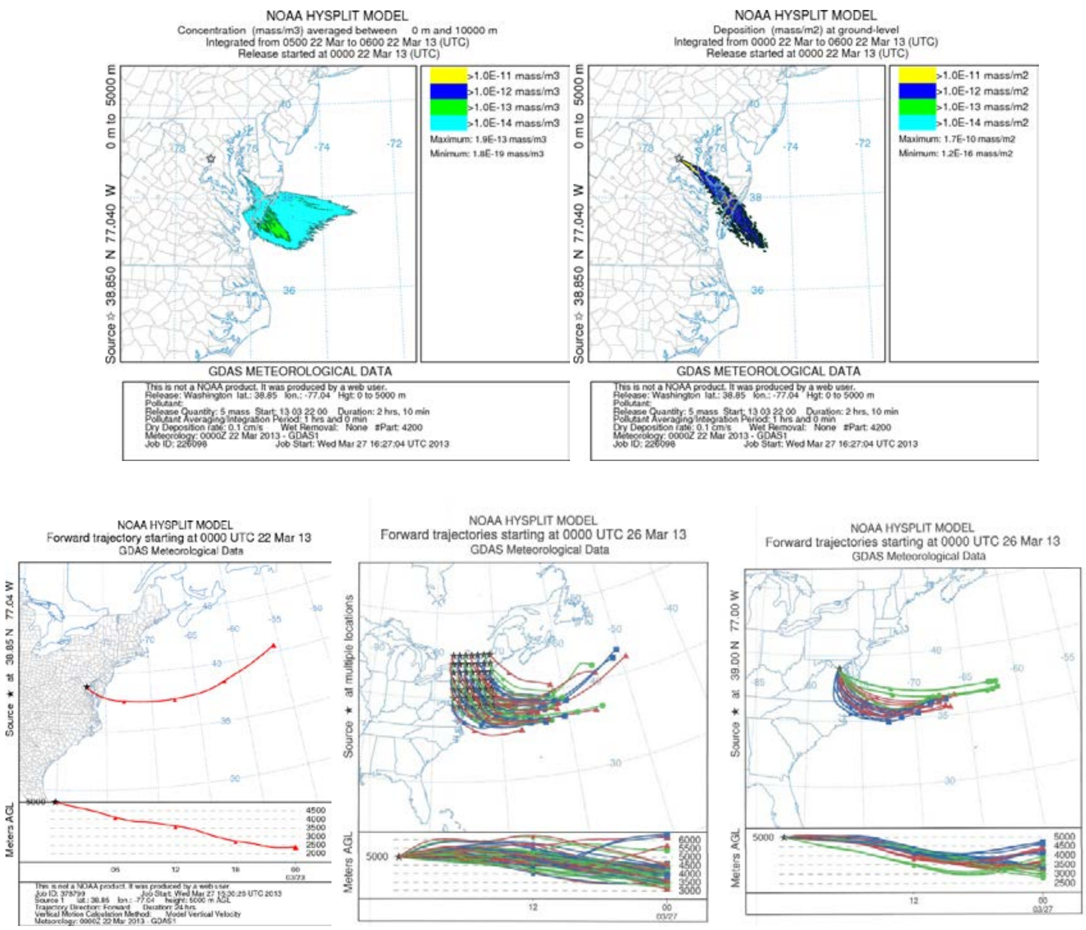

Figure 13: HYSPLIT output displays. a) Top row, left shows a Concentration output, b) Top row, right shows a Dispersion output, c) Bottom row, left shows a normal, single point Trajectory output, d) Bottom row, middle shows a matrix Trajectory output, and e) Bottom row, right shows an ensemble Trajectory output.

Overall, HYSPLIT is a proven tool in modeling transport and dispersion of any type of trace gas emissions effecting the aviation, air quality management and emergency preparedness industries, thus making it an excellent modeling tool for passive volcanic SO_2 emissions (Air Resources Laboratory, 2012). To date, the HYSPLIT system has been used primarily as a forward concentration/dispersion and trajectory analysis tool to model SO_2 emissions from eruptive events and project the path of the emission cloud until it fully disperses. It has also had some usage as a backward tracing tool, but this facet has not been exploited to the fullest extent (Igarashi et al., 2004).

Relevance of Literature to Experimental Methodology

Given an OMI image of an SO_2 emission and its companion CALIOP altitude image, the problem is how to determine that emission's source characteristics. As previously mentioned, HYSPLIT's backward tracing functionality has not been as widely utilized as the forward functionality, so the initial step in the experiment outlined in the Experimental Methodology section will be to narrow the emissions source within a geographic area to determine the source location using HYSPLIT's backward tracing capabilities.

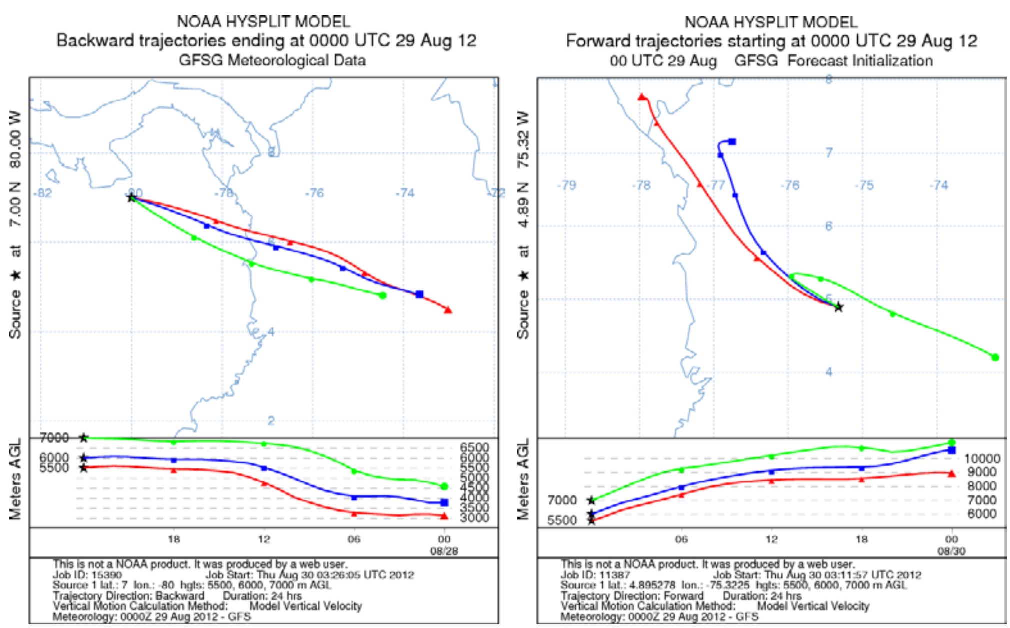

Figure 14: Left image is the backward trajectory model for the western coast of Colombia showing a generic plume originating at the approximate location of the Nevado del Ruiz volcano. The right image is a forward model, illustrating the trajectory and patterns at 5500 m (red), 6000m (blue) and 7000m (green) above ground level (AGL) for an eruption at Nevado del Ruiz, with trajectory points at 6 hour intervals beginning at the black star symbol and continuing along a line illustrated by circles, squares and triangles along the colored pathway.

The case illustrated above in Figure 14 shows just how difficult the problem of back tracing an emission to its source can be. The image on the left shows a backward trajectory from a hypothetical SO_2 emission located at grid coordinates 7^{o}N, -80^{o}W, off the southern coast of Panama in the Pacific Ocean. According to the HYSPLIT results, the source lies near grid coordinates 5^{o}N and between -75^o and -73^{o}W. The actual source of Nevado del Ruiz lies at 4.89^{o}N, -75.32^{o}W, slightly south and more to the west than as predicted. Given that SO_2 emissions have varying dissipation rates from reacting with the water in the atmosphere, areas in which the atmosphere is saturated in water vapor will have shorter SO_2 life spans (days to a few weeks) than those in drier environments (weeks to a few months). Because HYSPLIT calculates the backward trajectory utilizing meteorological conditions along a user provided time frame, part of solving the source location problem is discerning the initial release time. Therefore, when determining the source location, several iterations of backwards trajectories will be needed at differing time frames to determine the best fit of source location, which will also provide an approximate initial release time.

Once those results have been obtained, the next step is to run multiple HYSPLIT iterations in forward concentration mode to perform a sensitivity analysis on the potential candidate location to narrow the scope of possible combinations of release time, duration and altitude of the top of the release. Once the scope has been sufficiently narrowed, a second round of HYSPLIT runs are necessary encompassing all the permutations of time frames, durations and maximum release heights to determine the best fit of the emission when compared to the original OMI and CALIOP images.

In utilizing this approach, the methodology discussed above will provide the necessary quantitative components needed in determining the dangers presented by an SO_2 emission. Hazards from impending volcanic eruptions, fossil fuel plants and smelting operations necessitate the need for such research in hopes that these efforts will improve evacuation planning, aviation routing and ameliorate potential losses of vegetation and revenue. The data and processing utilized in this approach is free to the end user, making it a cost-effective methodology to implement in locations that are economically unable to continuously monitor SO_2 emission sources in a fashion similar to areas like Mt. Etna, Italy and Mt. St. Helens, Washington, United States.

EXPERIMENTAL METHODOLOGY

The proposed methodology outlined below in the flowchart and detailed step by

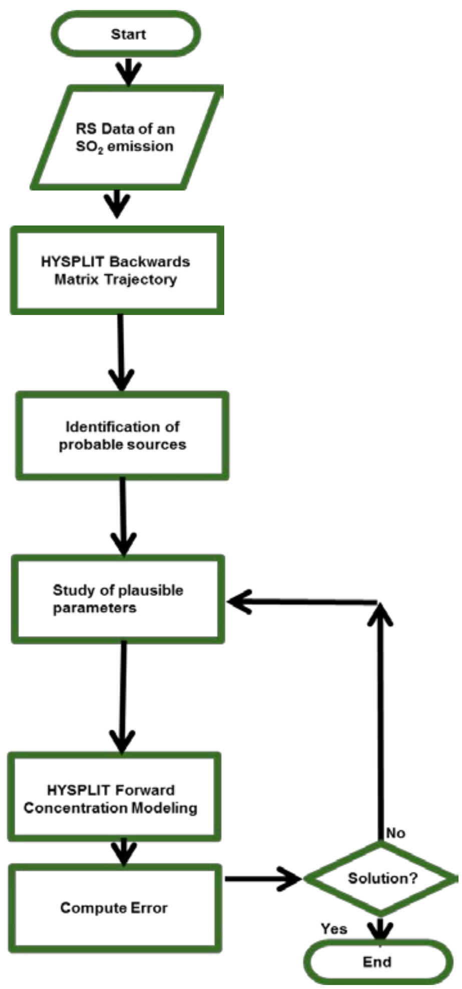

Figure 15: Flowchart of general methodology for source term detection

step list below utilizes data inputs from OMI and CALIOP images obtained from NASA's Goddard Earth Sciences Data and Information Services Center's Giovanni program and compares them to data derived from NOAA's HYSPLIT simulation program to determine the source location, time of release, duration, size, concentration and release rate of an SO_2 emission. Meteorological inputs to the HYSPLIT program are obtained from the Global Data Assimilation System (GDAS1) archived files that provide global data from to December 1, 2004 to the present (NOAA-Air Resources Laboratory, 2013). GDAS1 3-hour, 6-hour, and 9-hour forecast information is compiled 4 times daily at 00, 06, 12 and 18 hours UTC at 1^o x1^o latitude/longitude grids for 23 vertical pressure levels ranging from 1000 hPa to 20 hPa, enabling the development of a emissions parcel model as it moves through the atmosphere (Lu, Streets, Zhang, & Wang, 2012; NOAA-Air Resources Laboratory, 2013). Lastly, a short program written in the R programming language is called to evaluate error as determined by the RMSE formula presented by Cervone and Franzese and shown below in Equation 2 (2010). The goal of the program is to obtain an error calculation, which correlates with the area and time of best fit between the OMI and HYSPLIT data. These error scores are then normalized and compared to statistically determine the optimal source variables that fit with the OMI image.

$$\mathrm{RMSE} = \sqrt{\frac{\overline{(C_o - C_s)^2}}{\overline{C_o}^2}}$$

Equation 2: RMSE formula for computing error between OMI and HYSPLIT data (Cervone & Franzese, 2010).

Process

The detailed process of obtaining location, time of release, duration of release, size, strength and concentration rate emission source information is outlined in the 11-step guide below.

Step 1: Retrieve an OMI image of an SO_2 emission via the NASA Giovanni web site (http://disc.sci.gsfc.nasa.gov/giovanni/overview/index.html). Download the data file in ASCII format.

Step 2: Using the OMI image, make a latitude/longitude rectangular grid of points surrounding the emission as an SO_2 intensity field, recalling that each OMI image pixel represents 0.125^o latitude and 0.125^o longitude and noting the timespan of the image. An example is shown below in Figure 16 as a subset of the Mt. Etna OMI image shown previously in Figure 10.

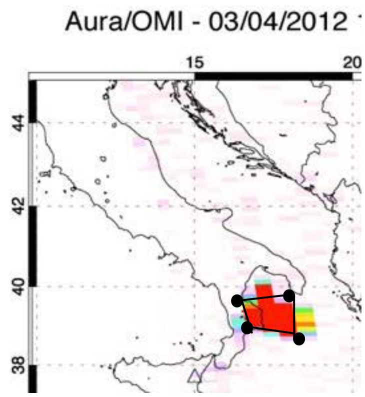

Figure 16: OMI Image subset of Mt. Etna illustrating the boxed SO_2 intensity field.

Step 3: Retrieve the corresponding CALIOP images for same date/time/rectangular grid of points noted in Step 2 to obtain emission's height range from the NASA Giovanni website, if available. Note the emission's highest (x), middle (y), and lowest (z) altitudes for use as the input parameters in HYSPLIT, further described in Step 4. If CALIOP data is not available for the emission, use altitudes spanning from 0 to 8000 m.

Step 4: Obtain GDAS1 Meteorological Data from ftp://arlftp.arlhq.noaa.gov/pub/archives/gdas1 site and download it to the HYSPLIT working directory, if using the PC-HYSPLIT. If using the web version of HYSPLIT, GDAS1 files will automatically be called, but users will need to understand the naming conventions described below to select the proper dataset for the HYSPLIT run. Note that the data sets are contained in weekly increments. GDAS1 datasets are named according to the following convention: gdas1.mmm.yy.w#, with “mmm” noting the specified month (e.g., jan for January), “yy” noting the specified year (e.g., 09 for 2009) and “w#” specifiying the week within that month and year. The weekly naming convention is as follows: days 1-7 are contained in the .w1 file, days 8-14 are contained in the .w2 file, days 15-21 are contained in the .w3 file, days 22-28 are in the .w4 file and days 29-31 are in the .w5 file (NOAA-Air Resources Laboratory, 2013).

Step 5: Run HYSPLIT in trajectory matrix mode to compute backwards trajectories of each rectangular gridded point at heights x, y & z, which are are the upper (x), middle (y) and lower (z) altitude points determined by the CALIOP data in Step 3. Multiple runs are necessary at 1 hour intervals to determine the time of initial release.

Step 6: Analyze the HYSPLIT backward trajectories produced in Step 4 to determine if there is/are potential sources (volcano, smelting operations, fossil fuel plants) in that area for the specified timeframe. If a timeframe maps back to a potential source then, move forward to Step 6, noting the time of release. If none of the timeframes track backwards to a potential source, then enlarge the original SO_2 emissions grid from the OMI data and proceed back through steps 2 through 4.

Step 7: Run HYSPLIT in forward trajectory mode to verify the backward trajectory results and time of release, which will also provide confirmation of the size and strength of the emission. If the forward trajectory matches the backward trajectory and time of release, then proceed to Step 7. If it does not match, go back to Step 5 and recheck the backward trajectory results.

Step 8: Construct a table listing all of the source characteristics (time, duration, latitude, longitude, mass units, top altitude of the release at the source and the bottom altitude of the release at the source) that will be tested in a sensitivity analysis. An example is provided in TABLE X below.

Step 9: Run HYSPLIT in forward dispersion/concentration mode to perform the sensitivity analyses of the time, duration, latitude, longitude, mass units, and top altitude of release at the source. Download the HYSPLIT binary data file for each run and execute the "Convert to ASCII" utility under the Concentration, Utilities menu to convert the data to table format.

Step 10: Take the output data file from OMI and from each HYSPLIT dispersion/concentration run and process the files through a statistical analysis program in R to determine the fit of information between the observed (OMI) and simulated (HYSPLIT) results. The fit is determined by the calculated error between the simulated and the observed values using the RMSE formula. The location associated with the minimized error is the best estimate for the origin of the emission at that particular time. Program code is listed in Figure 17 below.

```
filename.omi     = "OMI.csv"
# Calls the OMI data file
filename.hysplit  =  "cdump_075_20"
# Calls the Hysplit data file
library(akima)
# Calls the akima library which interpolates irregularly spaced data
library(maps)
# Calls the maps library which draws geographical maps
library(mapdata)
# Calls the mapdata library which contains extra map databases
OMI            = read.table(filename.omi,skip=9,sep=",")
# Reads the OMI file, skipping the 9th and values separated by commas
HYSPLIT         = read.table(filename.hysplit,header=T,sep="")
# Reads the HYSPLIT file, with the top row as a header row and values separated by a space
HYSPLIT         = HYSPLIT[1:(nrow(HYSPLIT)-1),]
# This takes out the last row of the data table, which is the average value at the end of the HYSPLIT data.
lori.colors = function(n) {
  return(rev(rainbow(n,end=.6)))
}
#This defines a color set for the output image
#
latitudes        =  as.numeric(levels(factor(OMI[,1])))
longitudes       =  as.numeric(levels(factor(OMI[,2])))
# Defines the domain of the OMI data
#
dat=OMI[,5]
dat[dat< 0]       =  NA
dat[dat> 1E20]     =  NA
dat             = matrix(dat,ncol=length(latitudes))
# Looks at the 5th column of data and eliminates areas of high noise and extreme values of OMI data.
#
int = interp(HYSPLIT[,4],HYSPLIT[,3],log(HYSPLIT[,5]),xo=longitudes,yo=latitudes)
int[[3]] = (int[[3]]/(max(int[[3]],na.rm=T)))*5
# Interpolates the points from an irregular grid
#
cat(file="Lori.out", sqrt( mean( ( int[[3]] - dat)^2 / mean((dat^2),na.rm=T),na.rm=T)) )
# Displays the error
#
if ( TRUE ) {
filled.contour(longitudes,latitudes,dat,
          xlab="longitudes",ylab="latitudes",
          xlim=c(14,19),ylim=c(30,40),
          plot.axes={
            map(add=T)
            axis(1)
            axis(2)
            image(int, add=T,col=lori.colors(20))
           },color.palette=lori.colors)
}
# Plots the maps to produce a display image
```

Figure 17: Program code in R that compares OMI and HYSPLIT datasets and derives an error measurement by implementing the RMSE formula and displays a mapped output. Documentation of the code is shown on lines beginning with the "#" symbol.

Step 11: Having determined the scenario with the lowest error value, run HYSPLIT in forward concentration mode to obtain a final image of the emission’s coordinates, altitude and concentration. Compare this HYSPLIT output with the original OMI image to ensure visual correlation.

This paper highlights two areas of interest in which the backtracking methodology was developed (Mt. Etna, Italy) and tested (Ecuador/Colombia).

Area of Interest – Mt. Etna, Italy

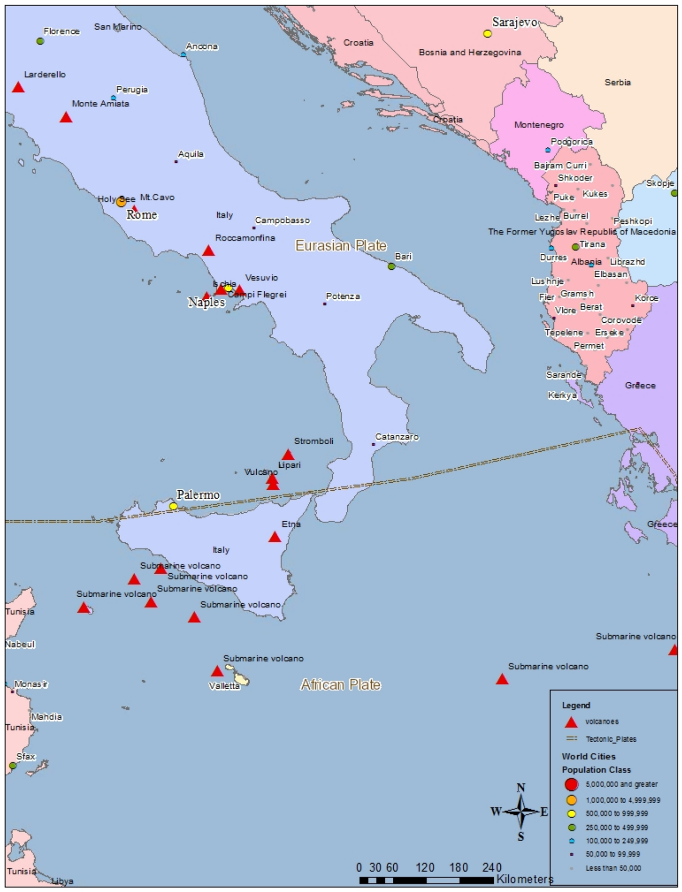

Figure 18: Map of the Sicily/Mt. Etna area with the boundary between the African and Eurasian plate represented by the line that lies just to the north of the island (ESRI, 2011).

Background

The area in which this process was developed was based on emissions emanating from Mt. Etna, Italy. Mt. Etna (3330 m) is a stratovolcano located on the island of Sicily, which lies to the southwest of the Italian mainland and is bisected by the convergent margin of the African plate and the Eurasian plate as shown above in Figure 18 (Global Volcanism Program, n.d.-a). Etna is the product of roughly 0.5 million years of eruptive activity, beginning as a submarine volcano and now is the largest volcano in Europe (Branca, Coltelli, De Beni, & Wijbrans, 2007). Etna has had eruptive activity chronicled since 1500 BC, and is one of the most extensively studied volcanoes on Earth. It houses state of the art equipment used to monitor seismic activity, growth via GPS, infrasound, lava samples and gaseous emissions, which have recorded Etna's passive extrusion of basaltic lava flows and gas punctuated by periods of more explosive activity of ash, lava and gas (Global Volcanism Program, n.d.-a).

Control Experiment

Given Etna's highly documented and studied eruptive patterns and readily available CALIOP imagery, it made for the perfect candidate as this methodology's control experiment. One of these documented eruptions occurred beginning on 13 May 2008 at 9:27 GMT, producing an explosive eruption cloud 4 km in height (Cannata, Montalto, Privitera, Russo, & Gresta, 2009; Global Volcanism Program, n.d.-a). Etna continued to produce smaller eruptive episodes of degassing as well as explosive eruptions periodically through 19 May 2008.

SO_2 Observations

The OMI image shown below in Figure 19 was taken over two days after the initial eruptive onset and clearly delineates the continued activity of Etna during this timeframe. The red box spanning on the uppermost image is the SO_2 intensity field that was used for backward trajectory calculations.

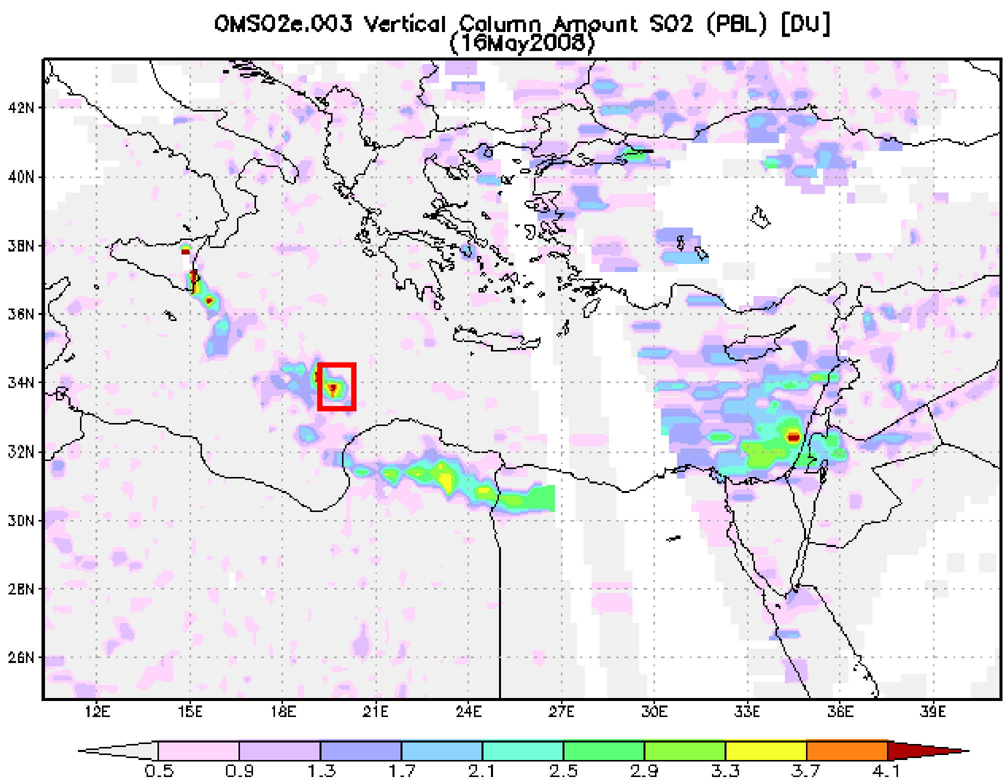

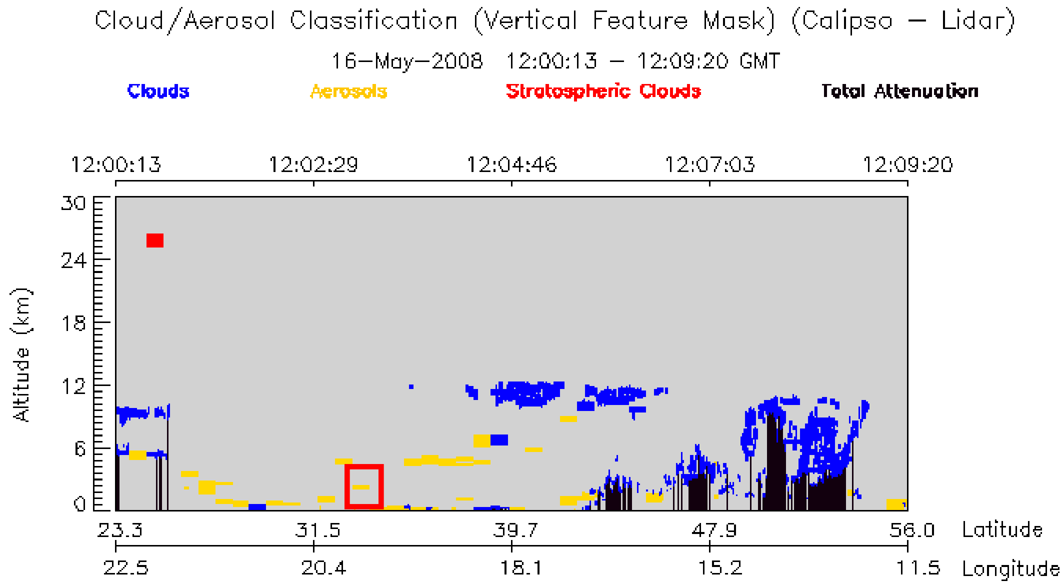

Figure 19: NASA Giovanni Images. Top: OMI dataset display from 16 May 2008 following several eruptive events at Mt. Etna, Italy. Bottom: CALIPSO image of aerosol heights in yellow. (Kempler & Hedge, 2013). Red boxes indicate the area of interest.

Trajectory Analysis

The control experiment began with backward trajectory measurements on the control target to define the first variable, the start time of the emission. The examined emission, highlighted in the red boxes of Figure 18, was located between 33.0^{o}N to 34.0^{o}N latitude and 19.0^{o}E to 20.0^{o}E longitude at between 1800 m and 2400 m AGL altitude. The time that this emission passed through this coordinate range varied from 12:02:40 to 12:03:01 UTC on 16 May, 2008. Trajectory analysis began with an initial matrix run in HYSPLIT, occurring 24 hours backwards from the start time of 12:03 UTC for Etna Box 1. This run produced a trajectory beyond Mt. Etna, so the time was revised to 18 hours, which produced the matrix trajectories depicted in Figure 20 below. The trajectories not only ended near Mt. Etna, but the model on the right side of the figure that was run from a starting altitude of 2400 m terminates at 3300 m, which was close to the 3330 m height of the volcano.

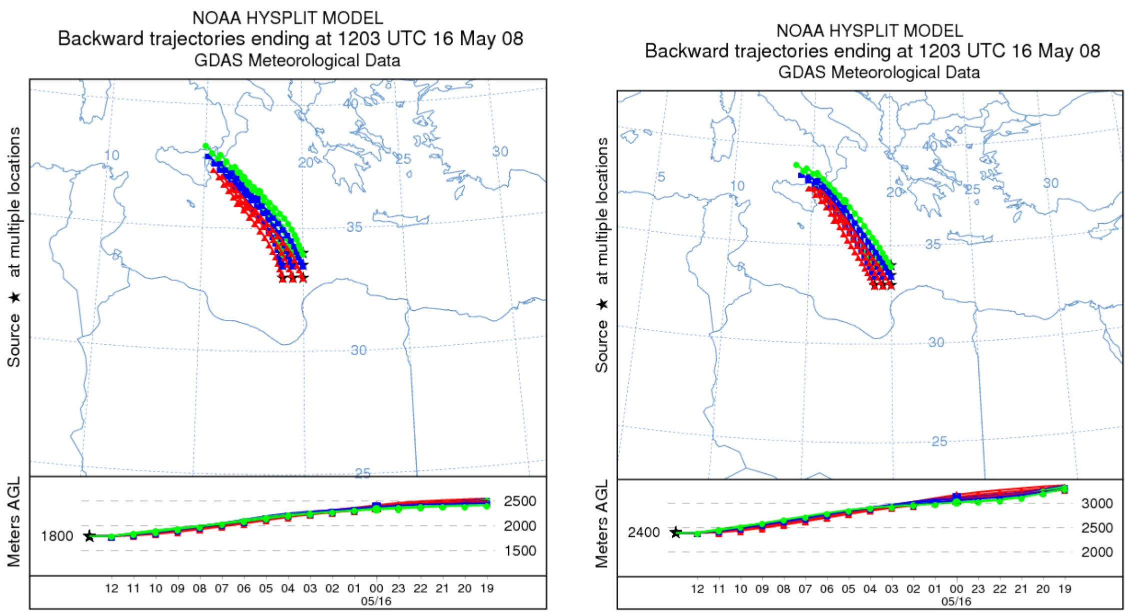

Figure 20: HYSPLIT Model run of backwards trajectories for 18 hours prior to 12:03 UTC, with the right image's parcel originating at 1800 m and the left image's parcel originating at 2400 m.

To further confirm this start time, an 18-hour forward trajectory was then run from the coordinates and elevation of Mt. Etna at a start time of 18:03 on 15 May 2008 and yielded an emission trajectory ending located at approximately 32.5^{o}N, 19.5^{o}E, which was just to the south of the coordinates given by the OMI image. Given these initial images, the 2400 m image on the right yielded a closer result to the actual height of Mt. Etna, at 3330 m, so this elevation was utilized as the basis for the sensitivity analysis.

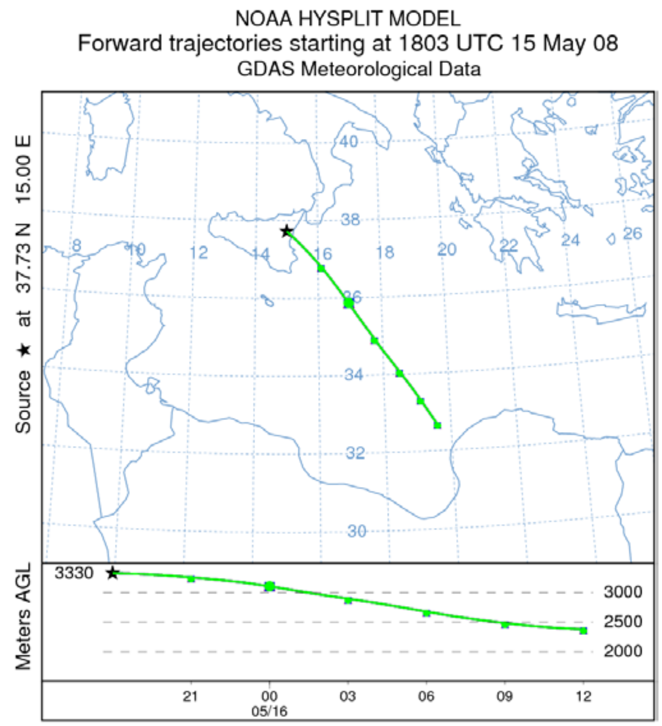

Figure 21: HYSPLIT forward trajectory beginning at 18:03 on 15 May 2008, detailing the transit path of an SO2 emission.

Given that this is trajectory lies beyond the OMI image's location, the next step of the process was to run multiple forward concentration simulations in HYSPLIT as part of the sensitivity analysis to determine the best fit time. Simulations were initiated at one hour intervals from Mt. Etna's coordinates and altitude between 12 and 16 hours post emission release. All other variables were held constant for this HYSPLIT run, which were the release bottom at Mt. Etna's elevation, 3330 m, the release top, assuming passive degassing at 3340 m, the duration of the release at 5 minutes and only 1 mass unit of gas released. Those results were then run through the program in R to determine the error rate. The time with the lowest error rate was associated with a release start time of 22:00 UT on 15 May 2008.

The next step was to test the sensitivity of the emission's release duration. Using the same methodology as determining initial time of release, all other variables were held constant, so the initial release time of 22:00 UT on 15 May 2008, release bottom at Mt. Etna's elevation, 3330 m, the release top, assuming passive degassing at 3340 m and only 1 mass unit was simulated. These HYSPLIT concentration runs were then compared to the OMI image in deciding the best fit according to a minimalized error rate.

This same process continued in determining the altitude of the emission as well as the number of mass units released. CALIOP data provided a window of aerosol emission between 1800-2400 m, but this figure required refinement to produce a best fit altitude. Similar to the problem of determining time, all other variables were held constant, so the initial release time of 22:00 UT on 15 May 2008, release bottom at Mt. Etna's elevation, 3330 m, the release top, assuming passive degassing at 3340 m, the duration of the release at 5 minutes and only 1 mass amount of gas were simulated and compared to the OMI image in deciding the best fit according to a minimalized error rate.

Once the sensitivity analysis completed, an initial "ideal" scenario was proposed, with the onset of the emission beginning on 15 May 2008 at 22:00 UT from Mt. Etna lying at 37.73^{o}N, 15^{o}E, with the bottom of the emission originating at 3330 m and the top at 3500 m, releasing 100 mass units of gas and taking 14 hours to travel to the coordinates identified by the OMI image.

To prove this was the optimal solution, an evolutionary, deterministic model of scenarios were run by testing every permutation of time, duration and altitude of the top of the emission within a range determined by the sensitivity analysis results. The error results were then processed through the R program with the goal of error minimalization. Over the course of 128 forward concentration HYSPLIT model runs, the candidate with the lowest error rate corresponded to an emission emanating from Mt. Etna on 15 May 2008 at 23:00 UT, with the peak height at the emission site of 3350 m, releasing 100 mass units of gas and taking 13 hours to travel to the OMI image coordinates. To conclude the process, a forward concentration model was run in HYSPLIT to verify these results, and the results of this model run appear below the Results and Discussion section and illustrate a match between the HYSPLIT and OMI/CALIOP data.

Area of Interest – Colombia and Ecuador

Figure 22: Map of the Northern Volcanic Zone of the Andes, South America. The line hugging the western coast of South America is the plate boundary between the Cocos and Nazca plates lying to the west and the South American plate to the east (ESRI, 2011).

Background

The first experimental area is of the western coast of northern South America, comprised of Colombia and Ecuador, shown above in Figure 22. These countries are part of the Andes mountain chain, which formed as a 7500 km long volcanic arc system from the subduction of the Cocos and Nazca oceanic plates beneath the continental South American plate (Stern, 2004). Subduction of this system began roughly 185 Ma with the opening of the South Atlantic Ocean pushing the South American plate into the Cocos and Nazca plates. With the Cocos and Nazca plates being composed of denser oceanic crust, they subducted beneath the South American plate and continue to do so at a rate of 7-9 cm/yr, creating the abundant source of magma that supplies the volcanoes in this chain (Stern, 2004). This system, divided into 4 regions of the Northern, Central, Southern and Austral Volcanic Zones, has produced 178 active volcanoes, with less than 25 of them actively monitored for instabilities. Unfortunately, over 20 million people live within a 100 km of an active volcano in this region, therefore rendering a methodology to aid in tracking potential eruptive development highly necessary (Stern, 2004).

Volcanism

The Northern Volcanic Zone is comprised of the 19 volcanoes of Colombia and 55 within Ecuador, as shown below in Figure 23. These volcanoes tend to have mafic to andesitic magmas that produce intermediate to explosive eruptions as well as extensive lahars due to the high amount of annual precipitation received in this region that creates stunning glacial summits on these mountains. One such eruption at Nevado del Ruiz, Colombia (5390 m) in November, 1985 killed over 23,000 people primarily through an eruptive lahar of muddy debris that buried entire villages (Stern, 2004).

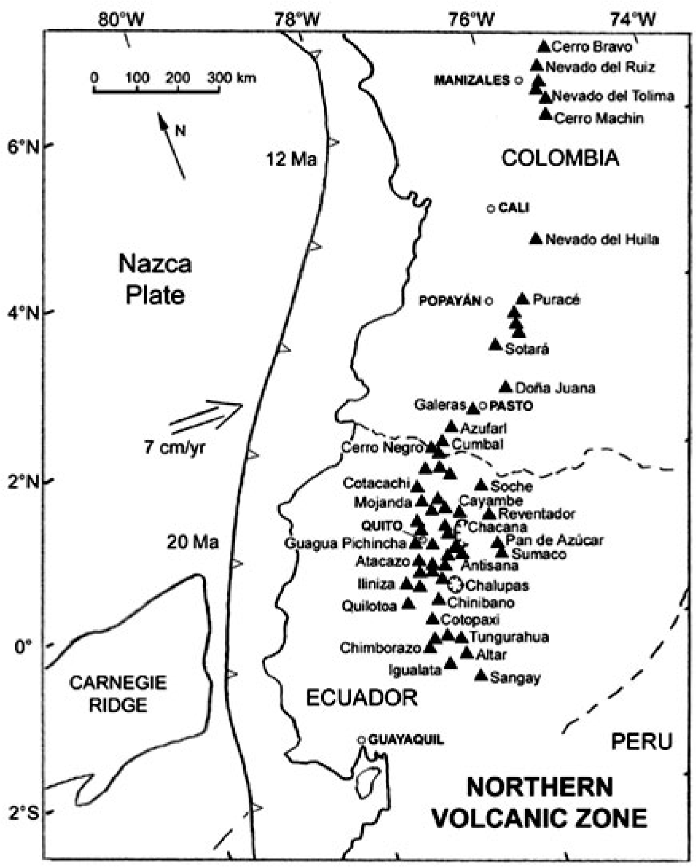

Figure 23: The Northern Volcanic Zone of the Andes Mountains encompassing Colombia and Ecuador. (Stern, 2004)

This event prompted the need for better awareness of the volcano's activity as well as developing and instigating evacuation plans in the event of further activity. Additional eruptions at Nevado del Ruiz, Nevado del Huila (5364 m) and Galeras, Colombia (4482 m) as well as Ecuador's Reventador (3562 m), Tungurahua (5023 m) and Sangay (5230 m) peaks over the past few years have further substantiated the need for additional volcano monitoring in this region to prevent a recurrence of the November, 1985 incident (Arellano et al., 2008; S. A. Carn et al., 2011; S.A. Carn et al., 2008; Sennert, 2012; Stern, 2004).

Colombia/Ecuador Experiment

SO_2 Observations

The first image examined is of the western coast of Colombia and Ecuador as shown below in Figure 23. The range of observed SO_2 is 0.5-3.3 DU in primarily green pixels next to small blue, purple and pink pixels between the coordinates of 5.0^{o}N to 5.5^{o}N latitude and 77.5^{o}W to 76.25^{o}W longitude, noted by the red box surrounding the parcel. Unfortunately, a corresponding CALIOP image could not be obtained for this emission as closest satellite track was 200 km to the east of the parcel.

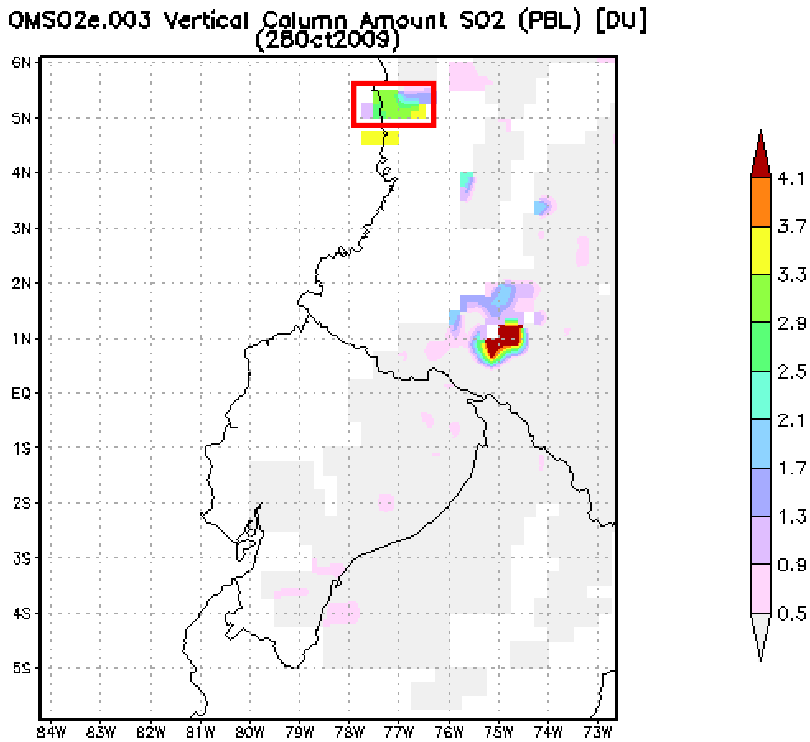

Figure 24: NASA Giovanni Image of an OMI dataset display from 28 October 2009 following an SO2 release off the western coast of Colombia. (Kempler & Hedge, 2013).

Trajectory Analysis

Given the location and temporal information from the OMI image, a HYSPLIT backwards trajectory series was run to better discern the source location, altitude and timing of the emission. Due to the lack of CALIOP imagery, the initial HYSPLIT backwards matrix trajectory was run at a series of elevations from 0 to 8000 m for nine points between 5^{o}N to 5.5^{o}N latitude and 77.5^{o}W to 76.5^{o}W longitude, which produced the HYSPLIT trajectories model seen below in Figure 25.

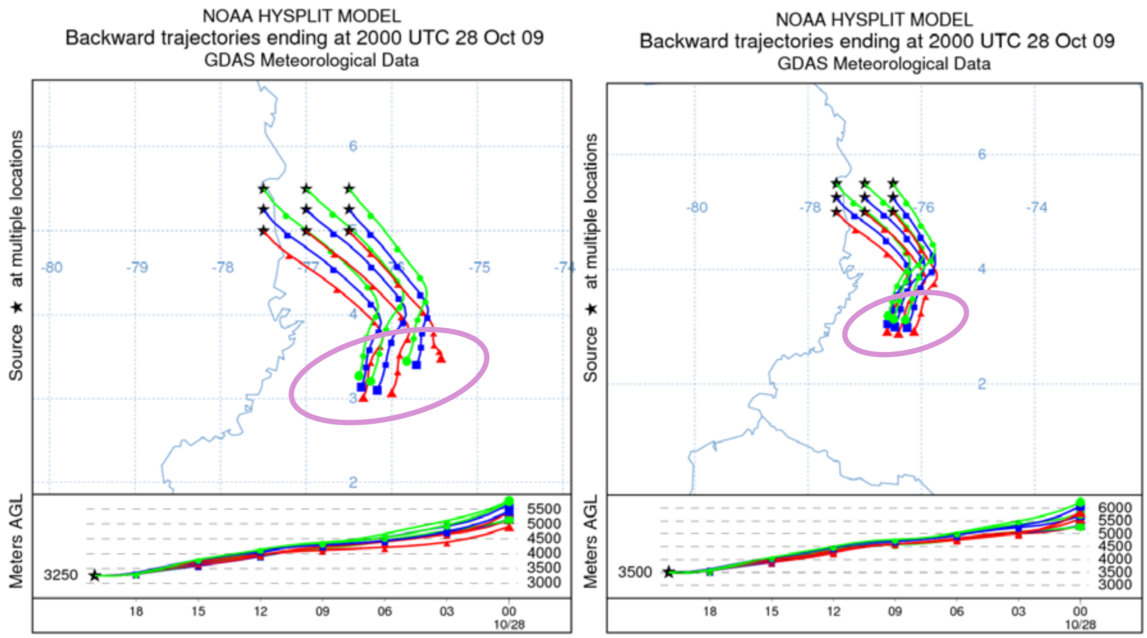

Figure 25: On left, the HYSPLIT 20 hour backwards matrix trajectory of an emission off the western coast of Colombia, with emission height originating at 3250 m. On right, another HYSPLIT 20 hour backwards trajectory utilizing the same starting coordinates, but at a starting height of 3500 m. Both images highlight an area surrounded by a purple ellipse detailing the location of possible originating sources.

In the control experiment, the emission source was a known entity, Mt. Etna. In this first test of the methodology, the source is unknown. In drawing a purple oval around the areas identified by HYSPLIT as the emission's source, the user next needs to inquire if potential sources of an SO_2 emission exist in this area. For this case, the purple oval encompasses the Nevado del Huila, Colombia volcano, which is one of the volcanoes detailed below in Table 3. These backward trajectory analyses also yielded a result close to the actual height of Nevado del Huila, at 5364 m, so this emission elevation of 3250 to 3500 m at the OMI coordinates was utilized as the basis for the sensitivity analysis and as an approximation in lieu of CALIOP data.

Table 3: Possible volcanic sources of the SO2 emission off of the western coast of Colombia (Global Volcanism Program, n.d.-b).

Volcano Name	Summit Elevation	Latitude	Longitude	Last Known Eruption
Nevado del Ruiz	5321 m	4.895 N	75.332 W	1991
Nevado del Tolima	5200+ m	4.67 N	75.33 W	1943
Nevado del Huila	5364 m	2.93 N	76.03 W	2011
Purace	4650+ m	2.32 N	76.40 W	1977
Dona Juana	4150+ m	1.47 N	76.92 W	1906
Galeras	4276 m	1.22 N	77.37 W	2010
Cumbal	4764 m	0.95 N	77.87 W	1926

Of these, only Nevado del Huila lies within the coordinates identified by the backwards trajectory model, and had documented activity in late October, 2009. To further confirm this possible location, a 20-hour forward trajectory was then run from the coordinates and elevation of Nevado del Huila at a start time of 0:00 on 28 October 2009 and yielded an emission trajectory ending located at approximately 4.75^{o}N, 76.85^{o}W, which was just to the south of the coordinates given by the OMI image and is seen below in Figure 26.

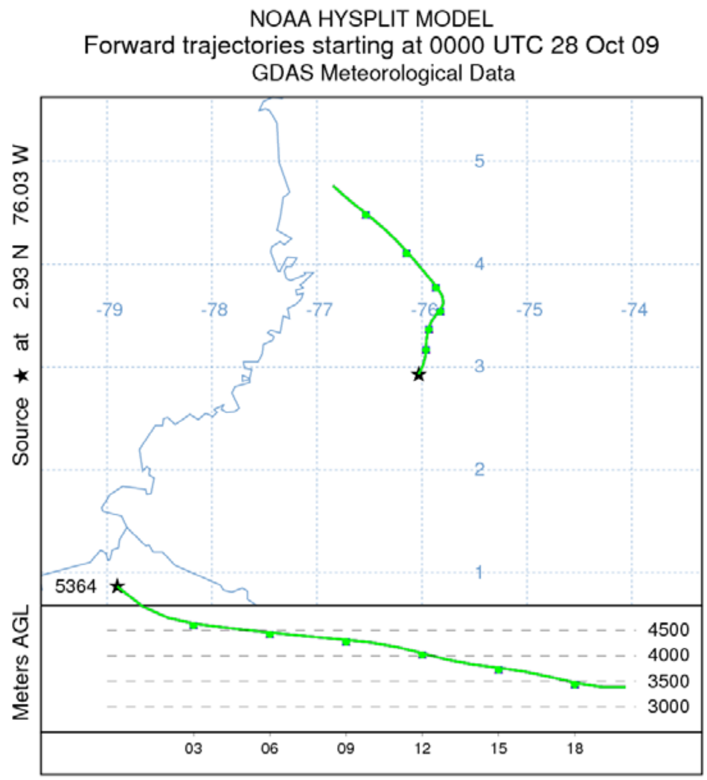

Figure 26: HYSPLIT 20-hour forward trajectory run from Nevado del Huila, indicating the parcel's ending altitude was approximately 3500 m.

The next step of the process was invoking HYSPLIT in dispersion/concentration mode to perform the sensitivity analysis, which narrowed the possible source parameters and was followed by the optimization routine. Beginning with the best fit time, simulations were initiated at one hour intervals from Nevado del Huila's coordinates and altitude between 16 and 27 hours post emission release. All other variables were held constant for this HYSPLIT run, which were the release bottom at Nevado del Huila's elevation, 5364 m, the release top, assuming passive degassing at 5600 m, the duration of the release at 30 minutes and only 1 mass unit of gas released. Those results were then run through the program in R to determine the error rate. The time with the lowest error rate was associated with a release start time of 1:00 UT on 28 October 2009.

Following the procedure for sensitivity testing the time was testing the sensitivity of the emission's release duration. Using the same methodology as determining initial time of release, all other variables were held constant, so the initial release time of 1:00 UT on 28 October 2009, release bottom at Nevado del Huila's elevation, 5364 m, the release top, assuming passive degassing at 5600 m and only 1 mass unit was simulated. These HYSPLIT concentration runs were then compared to the OMI image in deciding the best fit according to a minimalized error rate.

This same process continued in determining the altitude of the emission as well as the number of mass units released. Due to the lack of CALIOP altitude data, additional simulations ranging from 5500 to 8500 m were required to produce a viable result. Similar to the problem of determining time, all other variables were held constant, so the initial release time of 1:00 UT on 28 October 2009, release bottom at Nevado del Huila's elevation, 5364 m, the release top, assuming passive degassing at 5500 to 8500 m, the duration of the release at 2 hours and 1 to 100,000,000 mass amounts of gas were simulated and compared to the OMI image in deciding the best fit according to a minimalized error rate.

Once the sensitivity analysis completed, an initial “ideal” scenario was proposed, with the onset of the emission beginning on 28 October 2009 at 1:00 UT from Nevado del Huila lying at 2.93^{o}N, 76.03^{o}W, lasting for a 2-hour duration, with the bottom of the emission originating at 5364 m and the top at 6500 m, releasing 100,000,000 mass units of gas and taking 19 hours to travel to the coordinates identified by the OMI image.

To prove this was the optimal solution, the evolutionary, deterministic model of scenarios were invoked by testing every permutation of time, duration and altitude of the top of the emission within a range determined by the sensitivity analysis results. The error results were then processed through the R program with the goal of error minimization. Over the course of 196 forward concentration HYSPLIT model runs, the candidate with the lowest error rate corresponded to an emission emanating for a 2-hour duration from Nevado del Huila on 28 October 2009 at 1:00 UT, with the peak height at the emission site of 6500 m, releasing 100,000,000 mass units of gas and taking 19 hours to travel to the OMI image coordinates. To conclude the process, a forward concentration model was run in HYSPLIT to verify these results, the results of which appear below the Results and Discussion section and illustrate a correlation between the HYSPLIT and OMI data.

RESULTS AND DISCUSSION

Both the control case of Mt. Etna, Italy and the test case of Nevado del Huila, Colombia resulted in successful reconstructions back to the source of the emission, fully demonstrating the ability of this process to determine the source characteristics of a random parcel of gas. Certainly, having the benefit of CALIOP data in the Etna case study allowed for a more expedient process, requiring less runs during the sensitivity analysis and optimization process and providing the ability to cross-check the methodology's results against an additional independent data source. However as the Nevado del Huila case illustrates, if a user is unable to obtain CALIOP data it will not preclude the user from obtaining a minimized result and only requires additional processing time.

Results

Control Experiment – Mt. Etna, Italy

As discussed in the previous section, 128 permutations of differing aspects of emission onset time, duration, and top of the release elevation were produced in HYSPLIT for the optimization procedure and are detailed in Appendix A – Etna Sensitivity Analysis and Optimization Data. These runs were then compared to the OMI dataset via an R program utilizing the RMSE formula, producing a range of error values from 0.4556268 to 0.729673. The bar chart below in Figure 27 illustrates this range of error values and breaks them into 6 different cluster groups, based on similarity of error value with the red group of 4 results showing the lowest error and the first one of these red bars the being the best fit scenario.

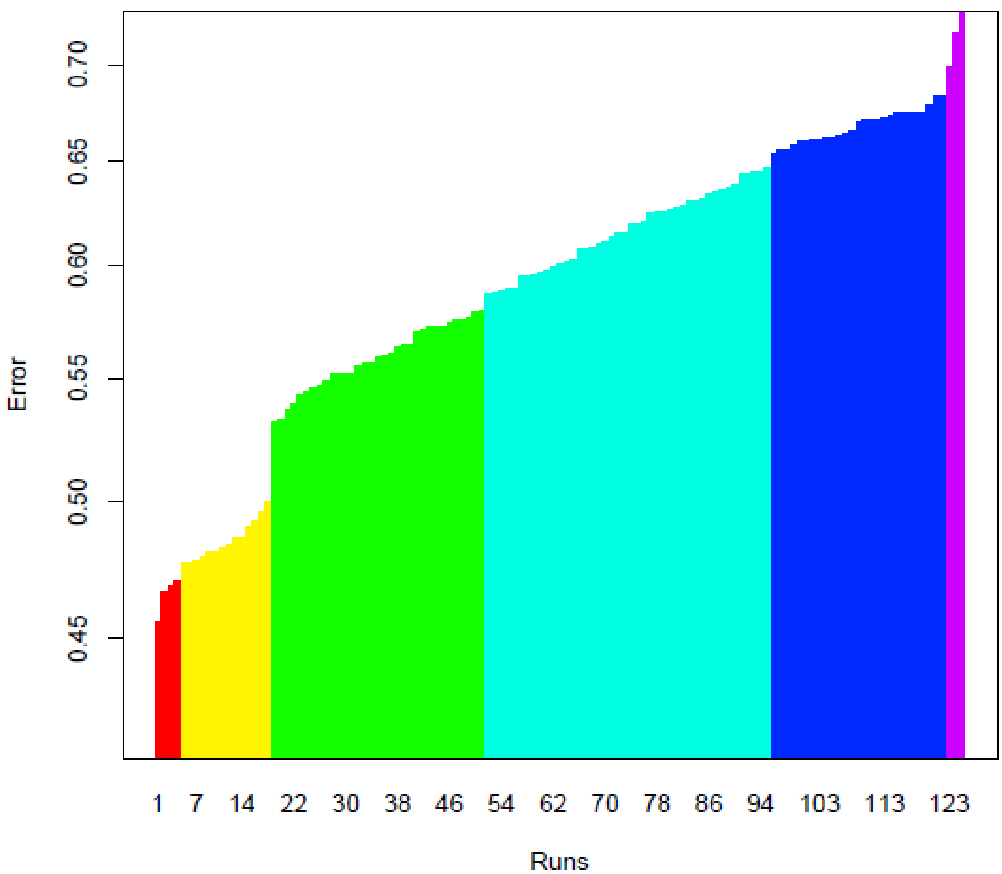

Figure 27: Bar chart of RMSE error rates, with the x-axis displaying the sequential run number and the y-axis displaying the error rate. Values in red correspond to the lowest error rates.

These color groups were then represented in a box plot format, shown below in Figure 28, with the red group corresponding to the box on the farthest left, followed by the yellow, green, light blue, blue and purple boxes progressing to the right. Within each of these boxes is a thick black line representing the median value of the cluster group, which best displays the minimization effort.

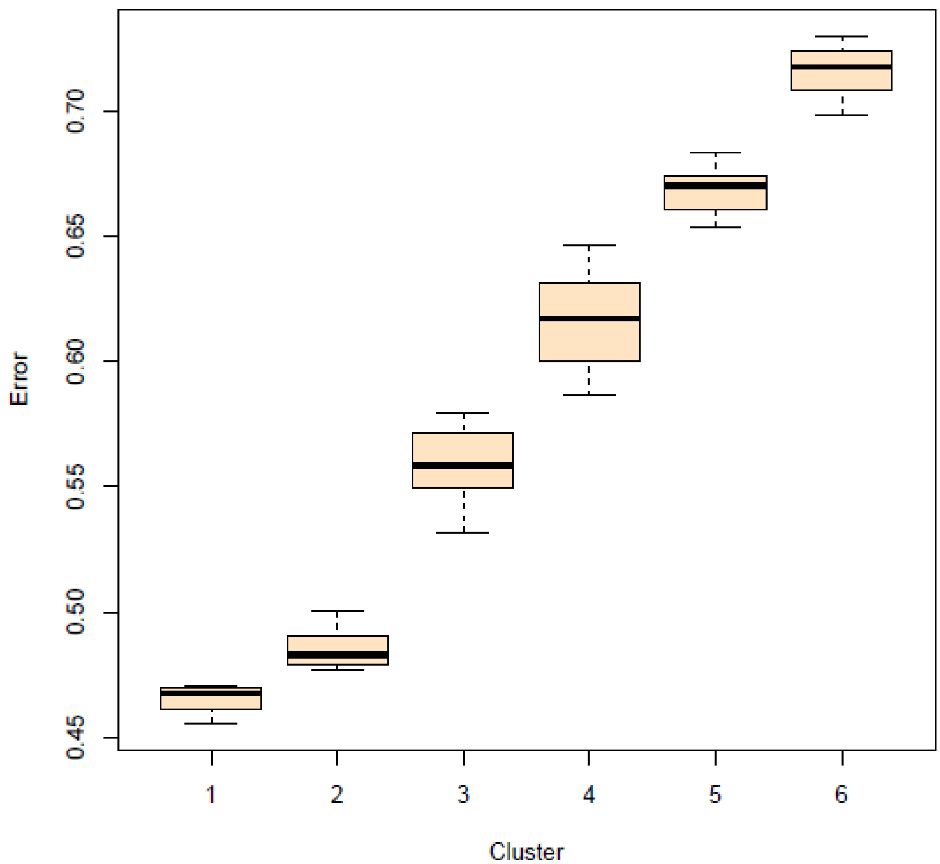

Figure 28: Box plot of RMSE error values broken into cluster groups that correspond to the bar chart groups shown in the previous figure. The thick black lines within each box represent the median value of that cluster group.

The optimized characteristics delivered by the evolutionary, deterministic modeling process corresponded to an emission emanating from Mt. Etna on 15 May 2008 at 23:00 UT, with the peak height at the emission site of 3350 m, releasing 100 mass units of gas and taking 13 hours to travel to the OMI image coordinates. To conclude the process a final HYSPLIT forward concentration run was simulated with these characteristics and the results of which are presented below in the concentration and particle density illustrations of Figure 29. When compared with the original OMI image, there is a close fit between the image and the simulation, allowing for the confirmation of this scenario as a likely case in determining the source characteristics of the emission.

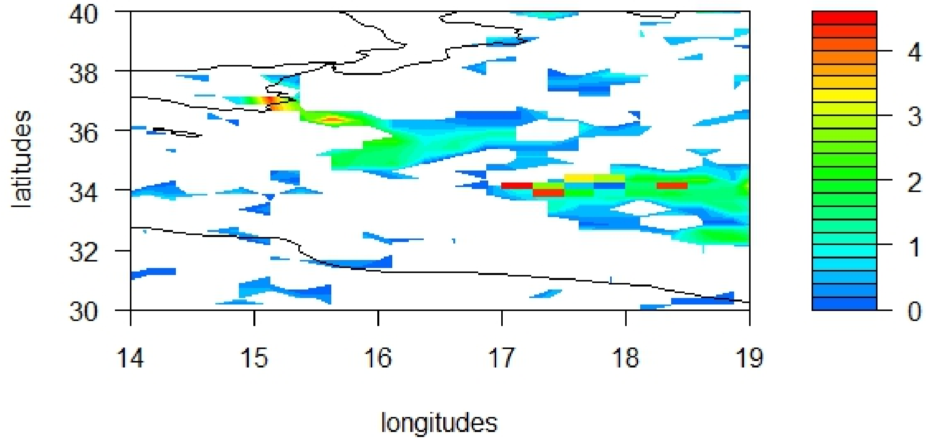
latitudes
longitudes
40
38
36
34
32
30
14
15
16
17
18
19
4
3
2
1
0

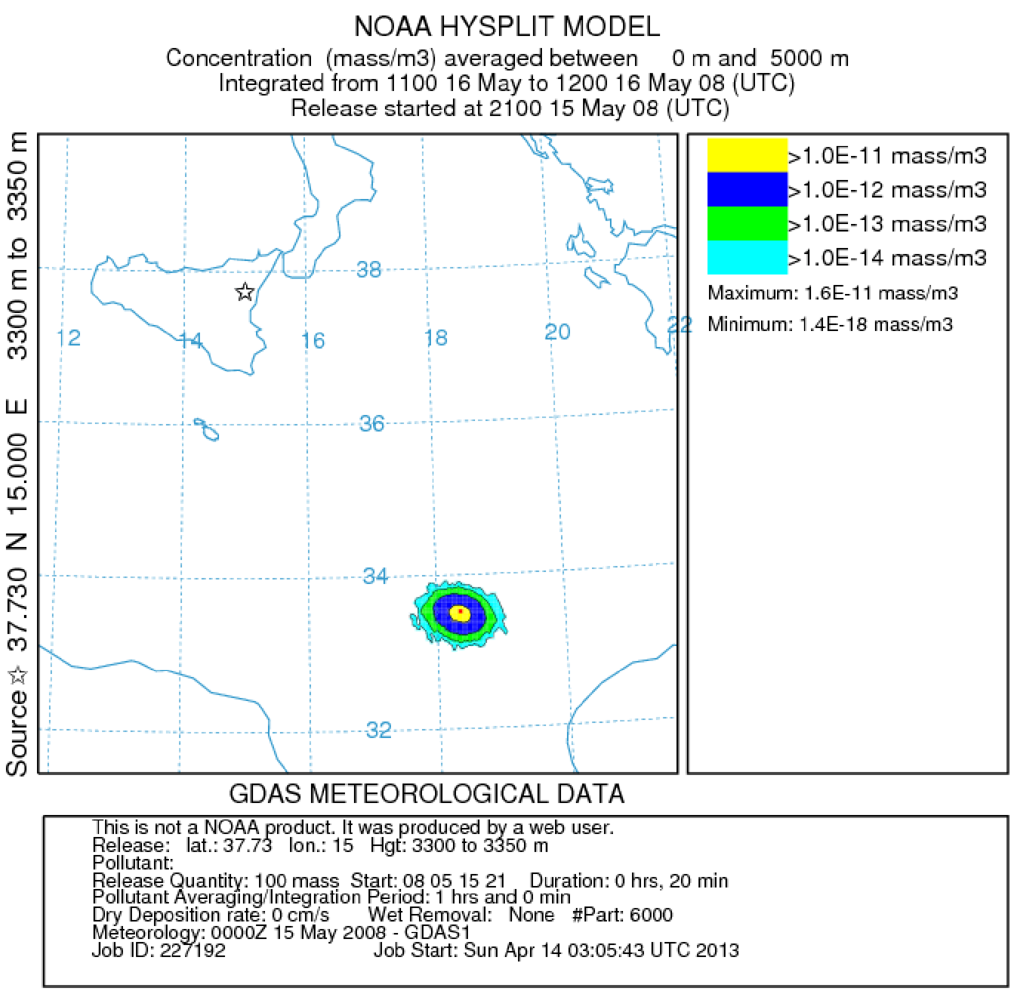
NOAA HYSPLIT MODEL
Concentration (mass/m3) averaged between 0 m and 5000 m
Integrated from 1100 16 May to 1200 16 May 08 (UTC)
Release started at 2100 15 May 08 (UTC)
Source ☆ 37.730 N 15.000 E 3300 m to 3350 m
>1.0E-11 mass/m3
>1.0E-12 mass/m3
>1.0E-13 mass/m3
>1.0E-14 mass/m3
Maximum: 1.6E-11 mass/m3
Minimum: 1.4E-18 mass/m3
GDAS METEOROLOGICAL DATA
This is not a NOAA product. It was produced by a web user.
Release: lat.: 37.73 lon.: 15 Hgt: 3300 to 3350 m
Pollutant:
Release Quantity: 100 mass Start: 08 05 15 21 Duration: 0 hrs, 20 min
Pollutant Averaging/Integration Period: 1 hrs and 0 min
Dry Deposition rate: 0 cm/s Wet Removal: None #Part: 6000
Meteorology: 0000Z 15 May 2008 - GDAS1
Job ID: 227192 Job Start: Sun Apr 14 03:05:43 UTC 2013

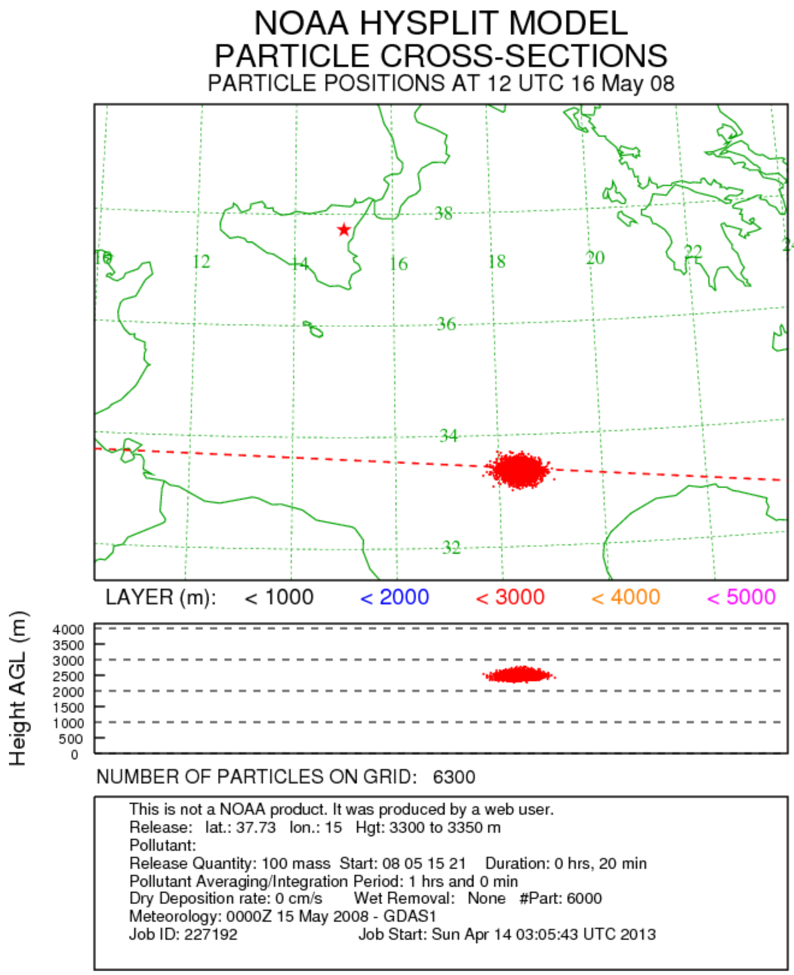

Figure 29: Top: R program map output displaying the map output associated with the lowest error scenario. Middle and Bottom: HYSPLIT forward concentration simulations, with the upper image displaying the trajectory of the emission 15 hours after release and the lower image displaying the particle density of the emission 15 hours post release.

Colombia/Ecuador

As discussed in the previous section, 186 permutations of differing aspects of emission onset time, duration, and top of the release elevation were produced in HYSPLIT for the optimization procedure and are detailed in Appendix B – Colombia/Ecuador Sensitivity Analysis and Optimization data. These runs were then compared to the OMI dataset via an R program utilizing the RMSE formula, producing a range of error values from 0.765254 to 1.958705. The bar chart below in Figure 30 illustrates this range of error values and breaks them into x different cluster groups, based on similarity of error value with the red group of x results showing the lowest error and the first one of these red bars the being the best fit scenario.

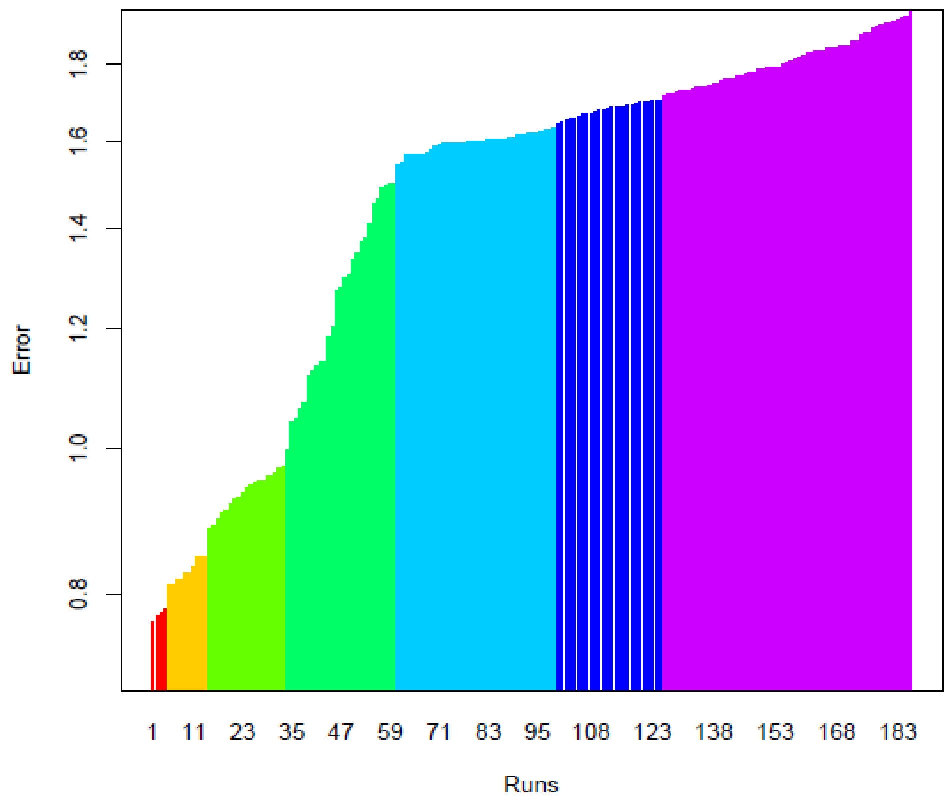

Figure 30: Bar chart of RMSE error rates, with the x-axis displaying the sequential run number and the y-axis displaying the error rate. Values in red correspond to the lowest error rates.

These color groups were then represented in a box plot format, shown below in Figure 31, with the red group corresponding to the box on the farthest left, followed by the yellow, green, light blue, blue and purple boxes progressing to the right. Within each of these boxes is a thick black line representing the median value of the cluster group, which best displays the minimization effort.

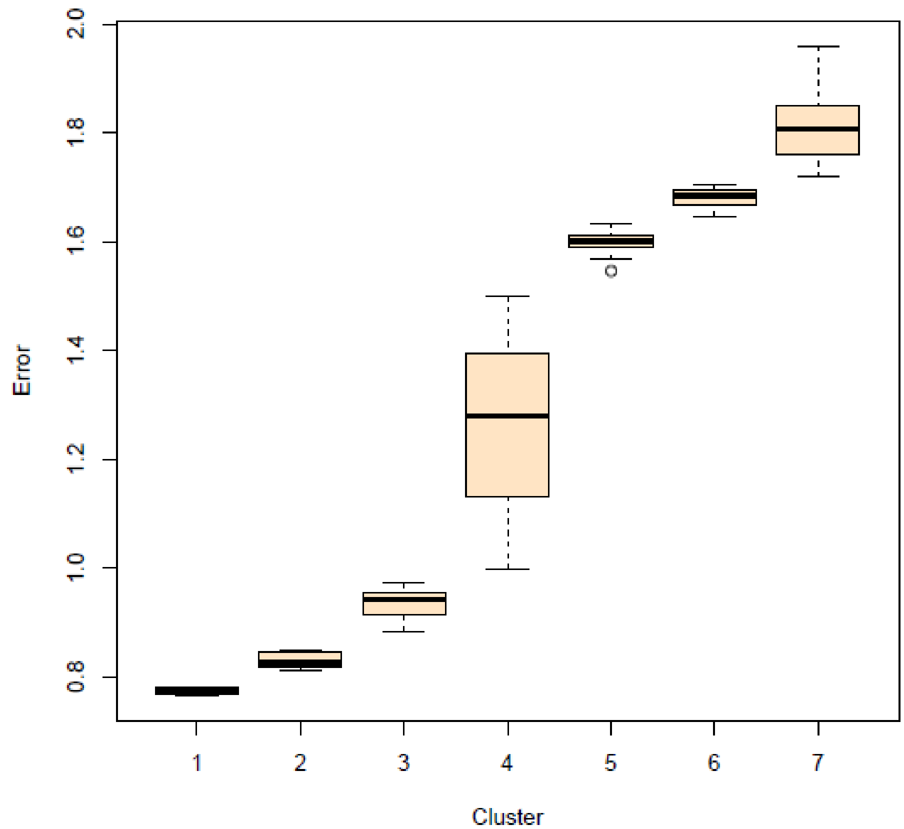

Figure 31: Box plot of RMSE error values broken into cluster groups that correspond to the bar chart groups shown in the previous figure. The thick black lines within each box represent the median value of that cluster group.

The optimized characteristics delivered by the evolutionary, deterministic modeling process corresponded to an emission emanating from Nevado del Huila on 28 October 2009 at 1:00 UT, with the peak height at the emission site of 6500 m, releasing 100,000,000 mass units of gas and taking 19 hours to travel to the OMI image coordinates. To conclude the process a final HYSPLIT forward concentration run was simulated with these characteristics and the results of which are presented below in the concentration and particle density illustrations of Figure 29. When compared with the original OMI image, there is a close fit between the image and the simulation, allowing for the confirmation of this scenario as a likely case in determining the source characteristics of the emission.

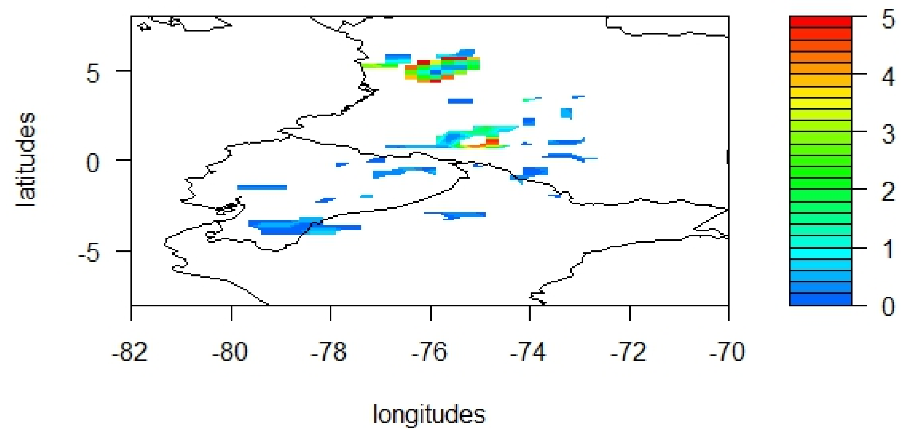
latitudes
longitudes
5
0
-5
-82
-80
-78
-76
-74
-72
-70
0
1
2
3
4
5

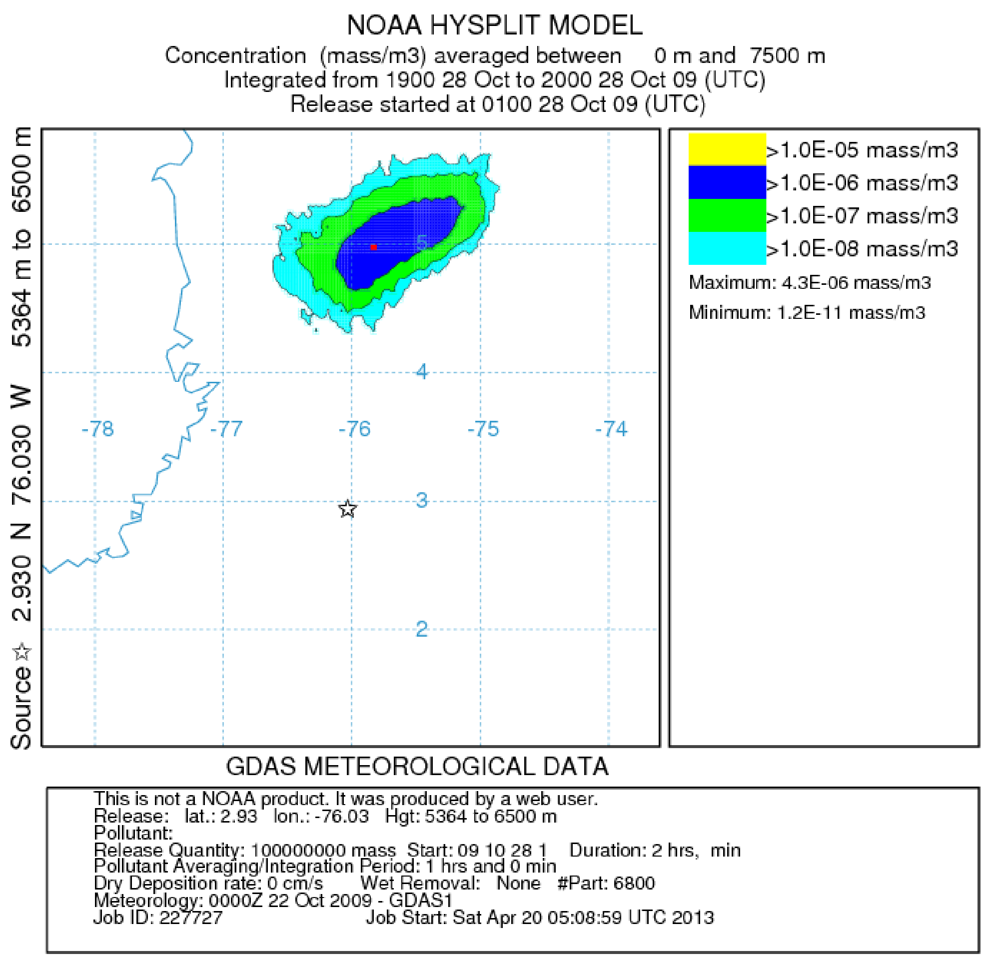
NOAA HYSPLIT MODEL
Concentration (mass/m3) averaged between 0 m and 7500 m
Integrated from 1900 28 Oct to 2000 28 Oct 09 (UTC)
Release started at 0100 28 Oct 09 (UTC)
Source ☆ 2.930 N 76.030 W 5364 m to 6500 m
>1.0E-05 mass/m3
>1.0E-06 mass/m3
>1.0E-07 mass/m3
>1.0E-08 mass/m3
Maximum: 4.3E-06 mass/m3
Minimum: 1.2E-11 mass/m3
-78
-77
-76
-75
-74
5
4
3
2
GDAS METEOROLOGICAL DATA
This is not a NOAA product. It was produced by a web user.
Release: lat.: 2.93 lon.: -76.03 Hgt: 5364 to 6500 m
Pollutant:
Release Quantity: 100000000 mass Start: 09 10 28 1 Duration: 2 hrs, min
Pollutant Averaging/Integration Period: 1 hrs and 0 min
Dry Deposition rate: 0 cm/s Wet Removal: None #Part: 6800
Meteorology: 0000Z 22 Oct 2009 - GDAS1
Job ID: 227727 Job Start: Sat Apr 20 05:08:59 UTC 2013

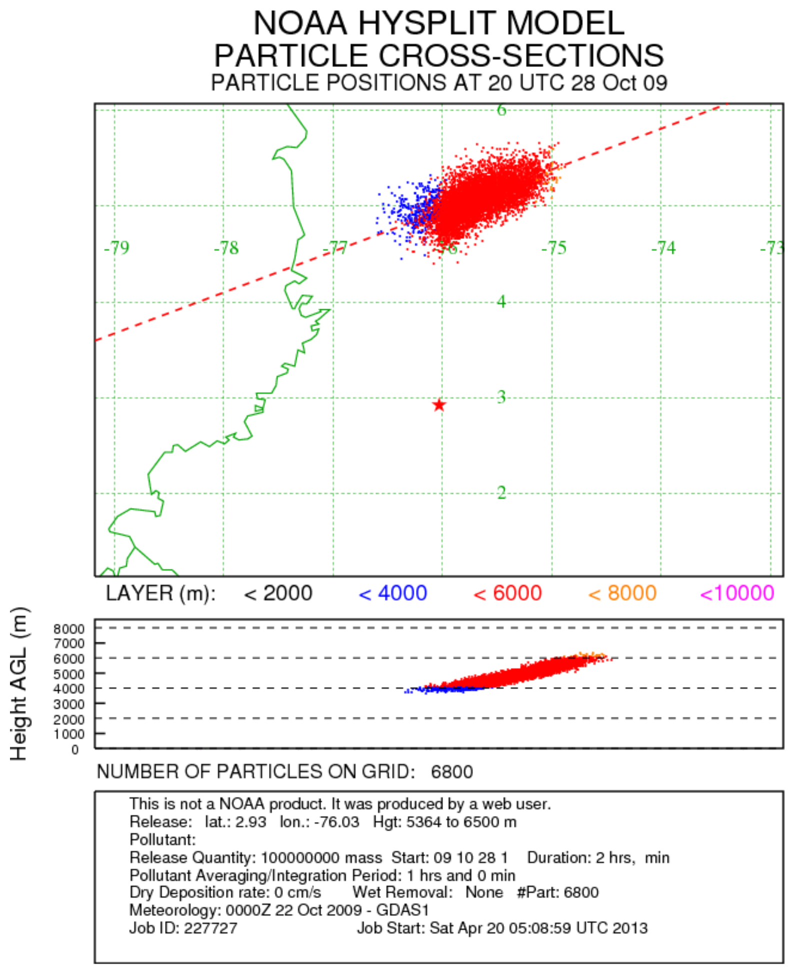

Figure 32: Top: R program map output displaying the map output associated with the lowest error scenario. Middle and Bottom: HYSPLIT forward concentration simulations, with the upper image displaying the trajectory of the emission 19 hours after release and the lower image displaying the particle density of the emission 19 hours post release.

Limitations

As a methodology in determining the source characteristics of an emission, this methodology has proven itself successful in both a control case and a test case environment, but like any other data intensive initiative, it is completely dependent upon the quality of the data inputs. The largest limitation of this methodology's capability is due to the lack of altitude data CALIOP can provide because of its limited swath width of 60 km in comparison to OMI's swath width of 2795 km (Winker et al., 2009). While a user is able to develop minimized error scenarios without the CALIOP data, it is preferential to have the altitude data provided by CALIOP both as an independent data source by which to check the optimization results as well as a resource in decreasing processing time by providing the altitude data utilized in the sensitivity analysis and the optimization procedure. Additionally, OMI and CALIOP data is limited to specific intervals in which the satellite systems passed over that particular area and at times does not produce an image with enough usable data to employ this methodology. For example, an OMI image of an SO_2 emission off of the western coast of Ecuador on 15 January 2010 produced only 12 data points for analysis in comparison to 2303 data points in the Nevado del Huila dataset, rendering mostly null results from the R program. Lastly, NASA's Giovanni system only has CALIOP data ranging from 13 June 2006 through 29 March 2010, so users must go to an alternate website at NASA's Langley Research Center to obtain data outside this range.

The next limitation of this methodology is that "HYSPLIT and other T&D systems that allow for backward modeling are susceptible to greater uncertainty of air parcel origination when tracking trajectories over periods larger than 3 days." (L. Y. L. Lee, Kwok, Cheung, & Yu, 2004). While the majority of emissions detected by OMI will fall within this 3 day range due to OMI's daily global coverage, it would impact emissions for which longer back tracking scenarios are required, forcing the user to piece together multiple successive days of OMI images and HYSPLIT simulations to trace an emission to its source. Additionally, HYSPLIT has a precision/accuracy limitation of 1% to 5% per day resulting from the integration over time interval, with the numerical uncertainty of a trajectory being ½ the distance between the starting and ending points (R. Draxler, 2008). Taking this precision/accuracy limitation into account explains why some of the latitude and longitude coordinates examined in both the Mt. Etna and Nevado del Huila case studies reported better error calculations slightly away from the volcano's coordinates and was the rationale behind why the volcano's latitude, longitude and elevation were utilized as the emission's source latitude, longitude and bottom of emission altitude in the optimization procedure.

Areas for Further Research

While outside the scope of this Thesis, the integration of other input products into the process would allow for a more robust study of the emission source characteristics as well as provide an additional set of data to compare to the OMI and HYSPLIT simulation results. For example, SO_2 exhibits measurable characteristics in the infrared portion of the spectrum, so the integration of this type of data or of ground based UV sensor data could help refine the results of the methodology presented in this Thesis.

An additional refinement of this process would be to automate the HYSPLIT data runs via a call program as well as changing the optimization procedure from an evolutionary deterministic model to an evolutionary stochastic model. By integrating these refinements, precision would theoretically increase while decreasing the user's processing time in manually starting each HYSPLIT simulation, converting each file to ASCII format and manually executing the R program.

Lastly, this process shows promise in better quantifying and understanding the characteristics of passive volcanic emissions. The VEI provides a framework in which to classify eruptive events, but little work has been done on analyzing and classifying the passive emissions from volcanoes on a global scale in an effort to better catalog and understand their characteristic eruptive patterns.

CONCLUSION

Volcanoes, built by successive layers of magma rising from the mantle of the Earth below the fractured crust, percolating upward through rocks, filling in fissures and ascending towards the surface, are a glimpse into the sheer power Earth has in recreating itself. Without these volcanoes, the Earth could not renew itself. For their destructiveness, their constructiveness is of equal measure. In the 4.6 billion years of Earth's existence, volcanoes have punctured the surface, creating the continents upon which we stand, creating an atmosphere that provides the air we breathe and protection from space as well as renewing the soil that provides our nourishment. And yet, such magnificence comes at a price. The peril of living in the shadow of such a crater emphasizes the human need to know about potential eruptive events prior to their onset, so evacuation planning can commence as well as determining the potential longer-term impacts of an eruption.

Recent examples of Mt. St. Helens, Mt. Pinatubo and Eyjafjallajökull illustrate the incredible energy a volcanic eruption can impart locally, and we are only beginning to glimpse the broader and longer term impacts of such eruptions. In the past 50 years, science and technology have improved to allow for remote monitoring of volcanoes via ground and satellite-based remote sensors. Such sensors can provide crucial data such as gas emissions of CO_2 and SO_2 while mitigating the risk to humans studying volcanic events and cycles. OMI is only one of the many sensors tasked with this responsibility, and it provides continual, daily global coverage of Earth's gaseous emissions at a higher and more precise resolution than any other fully operational satellite currently employed.

Utilizing this information in tandem with meteorologically integrated T & D modeling software such as HYSPLIT enables both forward and backward trajectory modeling to discern the path a dangerous volcanic gaseous emission will take or allow the user to trace the emission back to its source. The methodology presented in this Thesis illustrates the ability to harness this data to more accurately assess the dangers a remotely located volcano poses in a highly cost-effective and timely manner to the end user. It also has the added benefit of applicability to any type of trace gas release, making it a powerful system for use in areas such as monitoring and enforcement of toxic gas releases.

INDEX

APPENDIX A – ETNA SENSITIVITY ANALYSIS AND OPTIMATION DATA

Etna Sensitivity Study Data

Etna Sensitivity Study									
Start Date	Time frame	Dura-tion	Origination		Rlse	Rlse	Mass		
and Time	in hrs	in min	Lat	Lon	Top in m	Bottom in m	Units	Error	Description
Sensitivity analysis of Release Start Time									
5/16/08 2:00	10	5	37.73	15	3340	3330	1	0.8560251	Coordinates of release at 10 hr post start
5/16/08 1:00	11	5	37.73	15	3340	3330	1	0.6692707	Coordinates of release at 11 hr post start
5/16/08 0:00	12	5	37.73	15	3340	3330	1	0.6685623	Coordinates of release at 12 hr post start
5/15/08 23:00	13	5	37.73	15	3340	3330	1	0.6326918	Coordinates of release at 13 hr post start
5/15/08 22:00	14	5	37.73	15	3340	3330	1	0.5464527	Coordinates of release at 14hr post start
5/15/08 21:00	15	5	37.73	15	3340	3330	1	0.6119673	Coordinates of release at 15hr post start
5/15/08 20:00	16	5	37.73	15	3340	3330	1	0.6599336	Coordinates of release at 16 hr post start
5/15/08 19:00	17	5	37.73	15	3340	3330	1	0.615100	Coordinates of release at 17 hr post start
5/15/08 18:00	18	5	37.73	15	3340	3330	1	0.6534218	Coordinates of release at 18 hr post start
5/15/08 17:00	19	5	37.73	15	3340	3330	1	0.7078085	Coordinates of release at 19 hr post start
5/15/08 16:00	20	5	37.73	15	3340	3330	1	0.7987118	Coordinates of release at 20 hr post start
5/15/08 15:00	21	5	37.73	15	3340	3330	1	0.8037726	Coordinates of release at 21hr post start

Etna Sensitivity Study									
Start Date	Time frame	Dura-tion	Origination		Rlse	Rlse	Mass		
and Time	in hrs	in min	Lat	Lon	Top in m	Bottom in m	Units	Error	Description
5/15/08 14:00	22	5	37.73	15	3340	3330	1	0.7986256	Coordinates of release at 22 hr post start
5/15/08 22:00	14	5	37.73	15	3340	3330	1	0.5464527	Proposed Ideal Source Characteristics (based on the time sensitivity analysis)
Sensitivity Analysis of Release Duration									
5/15/08 22:00	14	1	37.73	15	3340	3330	1	0.5717084	Duration of 1 minute
5/15/08 22:00	14	5	37.73	15	3340	3330	1	0.5464527	Duration of 5 minutes
5/15/08 22:00	14	10	37.73	15	3340	3330	1	0.5682005	Duration of 10 minutes
5/15/08 22:00	14	12	37.73	15	3340	3330	1	0.5479003	Duration of 12 minutes
5/15/08 22:00	14	14	37.73	15	3340	3330	1	0.6104894	Duration of 14 minutes
5/15/08 22:00	14	15	37.73	15	3340	3330	1	0.4966785	Duration of 15 minutes
5/15/08 22:00	14	16	37.73	15	3340	3330	1	0.6108789	Duration of 16 minutes
5/15/08 22:00	14	17	37.73	15	3340	3330	1	0.5472741	Duration of 17 minutes
5/15/08 22:00	14	20	37.73	15	3340	3330	1	0.5429609	Duration of 20 minutes
5/15/08 22:00	14	25	37.73	15	3340	3330	1	0.5680507	Duration of 25 minutes
5/15/08 22:00	14	30	37.73	15	3340	3330	1	0.5010863	Duration of 30 minutes
5/15/08 22:00	14	45	37.73	15	3340	3330	1	0.5607656	Duration of 45 minutes
5/15/08 22:00	14	60	37.73	15	3340	3330	1	0.5077341	Duration of 60 minutes
5/15/08 22:00	14	65	37.73	15	3340	3330	1	0.5058056	Duration of 65 minutes
5/15/08 22:00	14	75	37.73	15	3340	3330	1	0.5771574	Duration of 75 minutes
5/15/08 22:00	14	90	37.73	15	3340	3330	1	0.6404438	Duration of 90 minutes
5/15/08 22:00	14	120	37.73	15	3340	3330	1	0.6067116	Duration of 120 minutes
5/15/08 22:00	14	15	37.73	15	3340	3330	1	0.4966785	Revised Proposed Ideal (using data from time and duration sensitivity analysis)
Sensitivity analysis of mass units									

Etna Sensitivity Study									
Start Date	Time frame	Dura-tion	Origination		Rlse	Rlse	Mass		
and Time	in hrs	in min	Lat	Lon	Top in m	Bottom in m	Units	Error	Description
5/15/08 22:00	14	15	37.73	15	3340	3330	1	0.4966785	Mass at 1 unit
5/15/08 22:00	14	15	37.73	15	3340	3330	5	0.4963128	Mass adjusted to 5 units
5/15/08 22:00	14	15	37.73	15	3340	3330	10	0.4960059	Mass adjusted to 10 units
5/15/08 22:00	14	15	37.73	15	3340	3330	25	0.4961429	Mass adjusted to 25 units
5/15/08 22:00	14	15	37.73	15	3340	3330	50	0.4958029	Mass adjusted to 50 units
5/15/08 22:00	14	15	37.73	15	3340	3330	100	0.4956	Mass adjusted to 100 units
5/15/08 22:00	14	15	37.73	15	3340	3330	500	0.4956885	Mass adjusted to 500 units
5/15/08 22:00	14	15	37.73	15	3340	3330	1000	0.495671	Mass adjusted to 1000 units
5/15/08 22:00	14	15	37.73	15	3340	3330	5000	0.4962745	Mass adjusted to 5000 units
5/15/08 22:00	14	15	37.73	15	3340	3330	10000	0.4965849	Mass adjusted to 10000 units
5/15/08 22:00	14	15	37.73	15	3340	3330	50000	0.4981036	Mass adjusted to 50000 units
5/15/08 22:00	14	15	37.73	15	3340	3330	100	0.4956	Revised Proposed Ideal (using sensitivity analysis of time, duration & mass units)
Sensitivity analysis of latitude									
5/15/08 22:00	14	15	39	15	3340	3330	100	0.9002084	Latitude adjusted to 39N
5/15/08 22:00	14	15	38.5	15	3340	3330	100	1.437334	Latitude adjusted to 38.5N
5/15/08 22:00	14	15	38.25	15	3340	3330	100	1.486458	Latitude adjusted to 38.25N
5/15/08 22:00	14	15	38	15	3340	3330	100	R shuts down?	Latitude adjusted to 38N
5/15/08 22:00	14	15	37.73	15	3340	3330	100	0.4956	Latitude adjusted to 37.73N
5/16/08 22:00	14	15	37.6	15	3340	3330	100	0.528274	Latitude adjusted to 37.6N
5/15/08 22:00	14	15	37.5	15	3340	3330	100	0.4912598	Latitude adjusted to 37.5N
5/15/08 22:00	14	15	37.25	15	3340	3330	100	R shuts down?	Latitude adjusted to 37.25N
5/15/08 22:00	14	15	37	15	3340	3330	100	0.7324858	Latitude adjusted to 37N
5/15/08 22:00	14	15	36	15	3340	3330	100	0.9120356	Latitude adjusted to 36N
5/15/08 22:00	14	15	37.5	15	3340	3330	100	0.4912598	Revised Proposed Ideal (using sensitivity analysis of time, duration, mass &

Etna Sensitivity Study									
Start Date	Time frame	Dura-tion	Origination		Rlse	Rlse	Mass		
and Time	in hrs	in min	Lat	Lon	Top in m	Bottom in m	Units	Error	Description
									latitude)
Sensitivity analysis of longitude									
5/15/08 22:00	14	15	37.5	16	3340	3330	100	1.546898	Longitude adjusted to 16E
5/15/08 22:00	14	15	37.5	15.75	3340	3330	100	0.7345344	Longitude adjusted to 15.75E
5/15/08 22:00	14	15	37.5	15.5	3340	3330	100	R shuts down	Longitude adjusted to 15.5E
5/15/08 22:00	14	15	37.5	15.25	3340	3330	100	0.5649172	Longitude adjusted to 15.25E
5/15/08 22:00	14	15	37.5	15	3340	3330	100	0.4912598	Longitude adjusted to 15E
5/15/08 22:00	14	15	37.5	14.75	3340	3330	100	0.563299	Longitude adjusted to 14.75E
5/15/08 22:00	14	15	37.5	14.5	3340	3330	100	0.7736084	Longitude adjusted to 14.5E
5/15/08 22:00	14	15	37.5	14.25	3340	3330	100	0.8621168	Longitude adjusted to 15.25E
5/15/08 22:00	14	15	37.5	14	3340	3330	100	0.8666851	Longitude adjusted to 14E
5/15/08 22:00	14	15	37.5	15	3340	3330	100	0.4912598	Revised Proposed Ideal (using sensitvity analysis of time, duration, mass latitude & longitude
Sensitivity analysis of Top of Release altitude									
5/15/08 22:00	14	15	37.5	15	3340	3330	100	0.4912598	Top of release altitude adjusted to 3340 m
5/15/08 22:00	14	15	37.5	15	3350	3330	100	0.493318	Top of release altitude adjusted to 3350 m
5/15/08 22:00	14	15	37.5	15	3375	3330	100	0.4921238	Top of release altitude adjusted to 3375 m
5/15/08 22:00	14	15	37.5	15	3400	3330	100	0.4905458	Top of release altitude adjusted to 3400 m
5/15/08 22:00	14	15	37.5	15	3450	3330	100	0.4902826	Top of release adjusted to 3450 m
5/15/08 22:00	14	15	37.5	15	3500	3330	100	0.4646676	Top of release altitude adjusted to 3500 m

Etna Sensitivity Study									
Start Date	Time frame	Dura-tion	Origination		Rlse	Rlse	Mass		
and Time	in hrs	in min	Lat	Lon	Top in m	Bottom in m	Units	Error	Description
5/15/08 22:00	14	15	37.5	15	3550	3330	100	0.4679991	Top of release adjusted to 3350 m
5/15/08 22:00	14	15	37.5	15	3750	3330	100	0.5341488	Top of release altitude adjusted to 3750 m
5/15/08 22:00	14	15	37.5	15	4000	3330	100	0.5278252	Top of release altitude adjusted to 4000 m
5/15/08 22:00	14	15	37.5	15	5000	3330	100	0.626968	Top of release altitude adjusted to 5000 m
5/15/08 22:00	14	15	37.5	15	6000	3330	100	R shuts down	Top of release altitude adjusted to 6000 m
5/15/08 22:00	14	15	37.5	15	3500	3330	100	0.4646676	Revised Proposed Ideal (using sensitvity analysis of time, duration, mass units, latitude, longitude and top of release)
Sensitivity analysis of Bottom of Release altitude									
5/15/08 22:00	14	15	37.5	15	3500	0	100	0.7451115	Bottom of release altitude adjusted to 0 m
5/15/08 22:00	14	15	37.5	15	3500	1000	100	0.7097318	Bottom of release altitude adjusted to 1000 m
5/15/08 22:00	14	15	37.5	15	3500	2000	100	0.5945467	Bottom of release altitude adjusted to 2000 m
5/15/08 22:00	14	15	37.5	15	3500	2500	100	0.5525178	Bottom of release altitude adjusted to 2500 m
5/15/08 22:00	14	15	37.5	15	3500	3000	100	R shut down	Bottom of release altitude adjusted to 3000 m
5/15/08 22:00	14	15	37.5	15	3500	3330	100	0.4646676	Bottom of release altitude adjusted to
5/15/08 22:00	14	15	37.5	15	3500	3400	100	0.5083263	Bottom of release altitude adjusted to 3400 m
5/15/08 22:00	14	15	37.5	15	3500	3330	100	0.4646676	Ideal (based on sensitivity analysis of time, duration, mass units, latitude, longitude & top

Etna Sensitivity Study									
Start Date	Time frame	Dura- tion	Origination		Rlse	Rlse	Mass		
and Time	in hrs	in min	Lat	Lon	Top in m	Bottom in m	Units	Error	Description
									and bottom of release data)

Etna Optimization Study Data

Etna Optimization Study									
Start Date	Time frame	Duration	Origination		Release	Release	Mass	HYSPLIT	
and Time	in hrs	in min	Lat	Long	Top in m	Bottom in m	Units	Job #	Error
5/16/08 0:00	12	15	37.73	15	3350	3330	100	227107	0.500131
5/16/08 0:00	12	15	37.73	15	3500	3330	100	226990	0.483774
5/16/08 0:00	12	15	37.73	15	4000	3330	100	226991	0.606964
5/16/08 0:00	12	15	37.73	15	4500	3330	100	227137	0.609518
5/16/08 0:00	12	15	37.73	15	5000	3330	100	227159	0.626856
5/16/08 0:00	12	10	37.73	15	3350	3330	100	227108	0.678922
5/16/08 0:00	12	10	37.73	15	3500	3330	100	226993	0.660679
5/16/08 0:00	12	10	37.73	15	4000	3330	100	226994	0.486459
5/16/08 0:00	12	10	37.73	15	4500	3330	100	227138	0.655674
5/16/08 0:00	12	10	37.73	15	5000	3330	100	227160	0.660207
5/16/08 0:00	12	5	37.73	15	3350	3330	100	227109	0.671402
5/16/08 0:00	12	5	37.73	15	3500	3330	100	226997	0.490692
5/16/08 0:00	12	5	37.73	15	4000	3330	100	226998	0.470721
5/16/08 0:00	12	5	37.73	15	4500	3330	100	227139	0.551537
5/16/08 0:00	12	5	37.73	15	5000	3330	100	227164	0.627492
5/16/08 0:00	12	20	37.73	15	3350	3330	100	227110	0.480848
5/16/08 0:00	12	20	37.73	15	3500	3330	100	227000	0.478003
5/16/08 0:00	12	20	37.73	15	4000	3330	100	227001	0.468415
5/16/08 0:00	12	20	37.73	15	4500	3330	100	227140	0.665102
5/16/08 0:00	12	20	37.73	15	5000	3330	100	227165	0.660207
5/16/08 0:00	12	25	37.73	15	3350	3330	100	227111	0.655024
5/16/08 0:00	12	25	37.73	15	3500	3330	100	227004	0.49581
5/16/08 0:00	12	25	37.73	15	4000	3330	100	227010	0.586307
5/16/08 0:00	12	25	37.73	15	4500	3330	100	227141	0.717677
5/16/08 0:00	12	25	37.73	15	5000	3330	100	227166	0.64469

Etna Optimization Study									
Start Date	Time frame	Duration	Origination		Release	Release	Mass	HYSPLIT	
and Time	in hrs	in min	Lat	Long	Top in m	Bottom in m	Units	Job #	Error
5/15/2008 23:00	13	15	37.73	15	3350	3330	100	227112	0.455627
5/15/2008 23:00	13	15	37.73	15	3500	3330	100	227012	0.479154
5/15/2008 23:00	13	15	37.73	15	4000	3330	100	227013	0.466822
5/15/2008 23:00	13	15	37.73	15	4500	3330	100	227142	0.564553
5/16/2008 23:00	13	15	37.73	15	5000	3330	100	227172	0.539033
5/15/2008 23:00	13	10	37.73	15	3350	3330	100	227113	0.63088
5/15/2008 23:00	13	10	37.73	15	3500	3330	100	227015	0.633832
5/15/2008 23:00	13	10	37.73	15	4000	3330	100	227016	0.492476
5/15/2008 23:00	13	10	37.73	15	4500	3330	100	227143	0.575435
5/15/2008 23:00	13	10	37.73	15	5000	3330	100	227173	0.544205
5/15/2008 23:00	13	5	37.73	15	3350	3330	100	227114	0.614994
5/15/2008 23:00	13	5	37.73	15	3500	3330	100	227018	0.643311
5/15/2008 23:00	13	5	37.73	15	4000	3330	100	227019	0.630885
5/16/2008 23:00	13	5	37.73	15	4500	3330	100	227144	0.57242
5/16/2008 23:00	13	5	37.73	15	5000	3330	100	227174	0.596463
5/15/2008 23:00	13	20	37.73	15	3350	3330	100	227115	0.643914
5/15/2008 23:00	13	20	37.73	15	3500	3330	100	227021	0.619505
5/15/2008 23:00	13	20	37.73	15	4000	3330	100	227022	0.486559
5/15/2008 23:00	13	20	37.73	15	4500	3330	100	227145	0.556894
5/15/2008 23:00	13	20	37.73	15	5000	3330	100	227175	0.551626
5/15/2008 23:00	13	25	37.73	15	3350	3330	100	227116	0.619616
5/15/2008 23:00	13	25	37.73	15	3500	3330	100	227025	0.614738
5/15/2008 23:00	13	25	37.73	15	4000	3330	100	227026	0.482316
5/16/2008 23:00	13	25	37.73	15	4500	3330	100	227146	0.575876
5/16/2008 23:00	13	25	37.73	15	5000	3330	100	227176	0.532341
5/16/2008 23:00	13	30	37.73	15	3350	3330	100	227325	0.613425
5/16/2008 23:00	13	45	37.73	15	3350	3330	100	227326	0.627717
5/16/2008 23:00	13	60	37.73	15	3350	3330	100	227338	0.60088
5/15/2008 22:00	14	15	37.73	15	3350	3330	100	227117	0.47712

Etna Optimization Study									
Start Date	Time frame	Duration	Origination		Release	Release	Mass	HYSPLIT	
and Time	in hrs	in min	Lat	Long	Top in m	Bottom in m	Units	Job #	Error
5/15/2008 22:00	14	15	37.73	15	3500	3330	100	227029	0.481175
5/15/2008 22:00	14	15	37.73	15	4000	3330	100	227030	0.477337
5/15/2008 22:00	14	15	37.73	15	4500	3330	100	227147	0.55461
5/15/2008 22:00	14	15	37.73	15	5000	3330	100	227177	0.579348
5/15/2008 22:00	14	10	37.73	15	3350	3330	100	227118	0.573791
5/15/2008 22:00	14	10	37.73	15	3500	3330	100	227032	0.572241
5/15/2008 22:00	14	10	37.73	15	4000	3330	100	227033	0.574992
5/15/2008 22:00	14	10	37.73	15	4500	3330	100	227148	0.558619
5/15/2008 22:00	14	10	37.73	15	5000	3330	100	227178	0.597498
5/15/2008 22:00	14	5	37.73	15	3350	3330	100	227119	0.551836
5/15/2008 22:00	14	5	37.73	15	3500	3330	100	227035	0.571908
5/15/2008 22:00	14	5	37.73	15	4000	3330	100	227036	0.53193
5/15/2008 22:00	14	5	37.73	15	4500	3330	100	227150	0.569617
5/15/2008 22:00	14	5	37.73	15	5000	3330	100	227179	0.608309
5/15/2008 22:00	14	20	37.73	15	3350	3330	100	227120	0.56359
5/15/2008 22:00	14	20	37.73	15	3500	3330	100	227038	0.546486
5/15/2008 22:00	14	20	37.73	15	4000	3330	100	227039	0.56399
5/15/2008 22:00	14	20	37.73	15	4500	3330	100	227151	0.589224
5/15/2008 22:00	14	20	37.73	15	5000	3330	100	227162	0.599232
5/15/2008 22:00	14	25	37.73	15	3350	3330	100	227121	0.578735
5/15/2008 22:00	14	25	37.73	15	3500	3330	100	227041	0.546032
5/15/2008 22:00	14	25	37.73	15	4000	3330	100	227042	0.542744
5/15/2008 22:00	14	25	37.73	15	4500	3330	100	227152	0.556682
5/15/2008 22:00	14	25	37.73	15	5000	3330	100	227180	0.595782
5/15/2008 21:00	15	15	37.73	15	3350	3330	100	227122	0.625188
5/15/2008 21:00	15	15	37.73	15	3500	3330	100	227045	0.625712
5/15/2008 21:00	15	15	37.73	15	4000	3330	100	227047	0.623963
5/15/2008 21:00	15	15	37.73	15	4500	3330	100	227153	0.537076
5/15/2008 21:00	15	15	37.73	15	5000	3330	100	227181	0.587999

Etna Optimization Study									
Start Date	Time frame	Duration	Origination		Release	Release	Mass	HYSPLIT	
and Time	in hrs	in min	Lat	Long	Top in m	Bottom in m	Units	Job #	Error
5/15/2008 21:00	15	10	37.73	15	3350	3330	100	227123	0.638135
5/15/2008 21:00	15	10	37.73	15	3500	3330	100	227050	0.661835
5/15/2008 21:00	15	10	37.73	15	4000	3330	100	227054	0.559683
5/15/2008 21:00	15	10	37.73	15	4500	3330	100	227154	0.552095
5/15/2008 21:00	15	10	37.73	15	5000	3330	100	227182	0.600858
5/15/2008 21:00	15	5	37.73	15	3350	3330	100	227124	0.625433
5/15/2008 21:00	15	5	37.73	15	3500	3330	100	227058	0.636626
5/15/2008 21:00	15	5	37.73	15	4000	3330	100	227059	0.587665
5/15/2008 21:00	15	5	37.73	15	4500	3330	100	227155	0.560469
5/15/2008 21:00	15	5	37.73	15	5000	3330	100	227183	0.595151
5/15/2008 21:00	15	20	37.73	15	3350	3330	100	227125	0.594917
5/15/2008 21:00	15	20	37.73	15	3500	3330	100	227061	0.602396
5/15/2008 21:00	15	20	37.73	15	4000	3330	100	227062	0.607135
5/15/2008 21:00	15	20	37.73	15	4500	3330	100	227156	0.570242
5/15/2008 21:00	15	20	37.73	15	5000	3330	100	227184	0.634474
5/15/2008 21:00	15	25	37.73	15	3350	3330	100	227126	0.601827
5/15/2008 21:00	15	25	37.73	15	3500	3330	100	227064	0.620244
5/15/2008 21:00	15	25	37.73	15	4000	3330	100	227065	0.610986
5/15/2008 21:00	15	25	37.73	15	4500	3330	100	227157	0.549196
5/15/2008 21:00	15	25	37.73	15	5000	3330	100	227185	0.589398
5/15/2008 20:00	16	15	37.73	15	3350	3330	100	227127	0.66154
5/15/2008 20:00	16	15	37.73	15	3500	3330	100	227067	0.660493
5/15/2008 20:00	16	15	37.73	15	4000	3330	100	227068	0.613201
5/15/2008 20:00	16	15	37.73	15	4500	3330	100	227136	0.64471
5/15/2008 20:00	16	15	37.73	15	5000	3330	100	227186	0.670194
5/15/2008 20:00	16	10	37.73	15	3350	3330	100	227128	0.675229
5/15/2008 20:00	16	10	37.73	15	3500	3330	100	227070	0.674547
5/15/2008 20:00	16	10	37.73	15	4000	3330	100	227071	0.646206
5/15/2008 20:00	16	10	37.73	15	4500	3330	100	227135	0.663098

Etna Optimization Study									
Start Date	Time frame	Duration	Origination		Release	Release	Mass	HYSPLIT	
and Time	in hrs	in min	Lat	Long	Top in m	Bottom in m	Units	Job #	Error
5/15/2008 20:00	16	10	37.73	15	5000	3330	100	227187	0.673221
5/15/2008 20:00	16	5	37.73	15	3350	3330	100	227129	0.674347
5/15/2008 20:00	16	5	37.73	15	3500	3330	100	227073	0.672376
5/15/2008 20:00	16	5	37.73	15	4000	3330	100	227074	0.63169
5/15/2008 20:00	16	5	37.73	15	4500	3330	100	227134	0.670781
5/15/2008 20:00	16	5	37.73	15	5000	3330	100	227188	0.658014
5/15/2008 20:00	16	20	37.73	15	3350	3330	100	227130	0.663302
5/15/2008 20:00	16	20	37.73	15	3500	3330	100	227076	0.653756
5/15/2008 20:00	16	20	37.73	15	4000	3330	100	227077	0.635446
5/15/2008 20:00	16	20	37.73	15	4500	3330	100	227133	0.670636
5/15/2008 20:00	16	20	37.73	15	5000	3330	100	227189	0.674536
5/15/2008 20:00	16	25	37.73	15	3350	3330	100	227131	0.698592
5/15/2008 20:00	16	25	37.73	15	3500	3330	100	227079	0.729673
5/15/2008 20:00	16	25	37.73	15	4000	3330	100	227082	0.683565
5/15/2008 20:00	16	25	37.73	15	4500	3330	100	227132	0.674833
5/15/2008 20:00	16	25	37.73	15	5000	3330	100	227190	0.683353
								Sum	
								Count	128
								Mean	0.595449
								Std Dev	0.063209
								Min	0.455627
								Max	
								Median	0.601354

APPENDIX B – COLOMBIA/ECUADOR SENSITIVITY ANALYSIS AND OPTIMZATION DATA

Nevado del Huila									
Sensitivity Analysis									
Start Date	Time frame	Duration	Origination		Release	Release	Mass		
and Time	in hrs	in min	Lat	Long	Top in m	Bottom in m	Units	Error	Description
Sensitivity analysis of Release Start Time									
10/27/2009 20:00	22	30	2.93	-76.03	5600	5364	1	2.193326	Coordinates of release at 22 hr post start
10/27/2009 20:00	23	30	2.93	-76.03	5600	5364	1	2.007818	Coordinates of release at 23 hr post start
10/27/2009 20:00	24	30	2.93	-76.03	5600	5364	1	1.925592	Coordinates of release at 24 hr post start
10/27/2009 21:00	21	30	2.93	-76.03	5600	5364	1	2.242097	Coordinates of release at 21 hr post start
10/27/2009 21:00	22	30	2.93	-76.03	5600	5364	1	2.013439	Coordinates of release at 22 hr post start
10/27/2009 21:00	23	30	2.93	-76.03	5600	5364	1	2.002481	Coordinates of release at 23 hr post start
10/27/09 22:00	22	30	2.93	-76.03	5600	5364	1	2.033969	Coordinates of release at 22 hr post start
10/27/09 22:00	20	30	2.93	-76.03	5600	5364	1	2.209299	Coordinates of release at 20 hr post start
10/27/09 22:00	21	30	2.93	-76.03	5600	5364	1	2.259653	Coordinates of release at 21 hr post start
10/27/09 22:00	22	30	2.93	-76.03	5600	5364	1	2.033969	Coordinates of release at 22 hr post start
10/27/09 23:00	21	30	2.93	-76.03	5600	5364	1	1.944948	Coordinates of release at 21 hr post start

Nevado del Huila									
Sensitivity Analysis									
Start Date	Time frame	Duration	Origination		Release	Release	Mass		
and Time	in hrs	in min	Lat	Long	Top in m	Bottom in m	Units	Error	Description
10/28/09 0:00	20	30	2.93	-76.03	5600	5364	1	1.831355	Coordinates of release at 20 hr post start
10/28/09 1:00	19	30	2.93	-76.03	5600	5364	1	1.287319	Coordinates of release at 19 hr post start
10/28/09 2:00	18	30	2.93	-76.03	5600	5364	1	null	Coordinates of release at 18 hr post start
10/28/09 3:00	17	30	2.93	-76.03	5600	5364	1	null	Coordinates of release at 17 hr post start
10/28/09 4:00	16	30	2.93	-76.03	5600	5364	1	null	Coordinates of release at 16 hr post start
10/27/09 19:00	23	30	2.93	-76.03	5600	5364	1	2.01526	Coordinates of release at 23 hr post start
10/27/09 19:00	24	30	2.93	-76.03	5600	5364	1	2.01353	Coordinates of release at 24 hr post start
10/26/09 20:00	22	30	2.93	-76.03	5600	5364	1	2.159501	Coordinates of release at 22 hr post start
10/27/09 20:00	23	30	2.93	-76.03	5600	5364	1	2.024422	Coordinates of release at 23 hr post start
10/27/09 21:00	22	30	2.93	-76.03	5600	5364	1	2.010496	Coordinates of release at 22 hr post start
10/27/09 22:00	21	30	2.93	-76.03	5600	5364	1	2.062926	Coordinates of release at 21 hr post start
10/27/2009 23:00	20	30	2.93	-76.03	5600	5364	1	2.178853	Coordinates of release at 20 hr post start
10/28/09 0:00	19	30	2.93	-76.03	5600	5364	1	2.239156	Coordinates of release at 19 hr post start
10/28/09 1:00	18	30	2.93	-76.03	5600	5364	1	null	Coordinates of release at 18 hr post start
10/28/09 2:00	17	30	2.93	-76.03	5600	5364	1	null	Coordinates of release at 17 hr post start
10/27/19 15:00	27	30	2.93	-76.03	5600	5364	1	1.929631	Coordinates of release at 27 hr post start
10/27/09 16:00	26	30	2.93	-76.03	5600	5364	1	1.928557	Coordinates of release at 26 hr post start

Nevado del Huila										
Sensitivity Analysis										
Start Date	Time frame	Duration	Origination		Release	Release	Mass		
and Time	in hrs	in min	Lat	Long	Top in m	Bottom in m	Units	Error	Description
10/27/09 16:00	27	30	2.93	-76.03	5600	5364	1	1.880602	Coordinates of release at 27 hr post start
10/27/09 17:00	25	30	2.93	-76.03	5600	5364	1	1.936516	Coordinates of release at 25 post start
10/27/09 17:00	26	30	2.93	-76.03	5600	5364	1	1.894984	Coordinates of release at 26 hr post start
10/27/09 17:00	27	30	2.93	-76.03	5600	5364	1	1.761329	Coordinates of release at 25 hr post start
10/27/09 18:00	24	30	2.93	-76.03	5600	5364	1	2.022307	Coordinates of release at 24 hr post start
10/27/09 19:00	23	30	2.93	-76.03	5600	5364	1	2.017712	Coordinates of release at 23 hr post start
10/27/09 20:00	22	30	2.93	-76.03	5600	5364	1	2.254836	Coordinates of release at 22 hr post start
10/27/09 21:00	21	30	2.93	-76.03	5600	5364	1	2.233405	Coordinates of release at 21 hr post start
10/27/09 22:00	20	30	2.93	-76.03	5600	5364	1	2.329479	Coordinates of release at 20 hr post start
10/27/09 23:00	19	30	2.93	-76.03	5600	5364	1	2.218996	Coordinates of release at 19 hr post start
10/28/09 0:00	18	30	2.93	-76.03	5600	5364	1	null	Coordinates of release at 18 hr post start
10/28/09 1:00	19	30	2.93	-76.03	5600	5364	1	1.287319	Proposed Ideal Source Characteristics (based on the time sensitivity analysis)
Sensitivity Analysis of Duration									
10/28/09 1:00	19	5	2.93	-76.03	5600	5364	1	1.476656	Duration of 5 minutes
10/28/09 1:00	19	10	2.93	-76.03	5600	5364	1	1.478023	Duration of 10 minutes
10/28/09 1:00	19	15	2.93	-76.03	5600	5364	1	1.302711	Duration of 15 minutes
10/28/09 1:00	19	30	2.93	-76.03	5600	5364	1	1.287319	Duration of 30 minutes

Nevado del Huila										
Sensitivity Analysis										
Start Date	Time frame	Duration	Origination		Release	Release	Mass		
and Time	in hrs	in min	Lat	Long	Top in m	Bottom in m	Units	Error	Description
10/28/09 1:00	19	45	2.93	-76.03	5600	5364	1	2.175753	Duration of 45 minutes
10/28/09 1:00	19	60	2.93	-76.03	5600	5364	1	1.275166	Duration of 60 minutes
10/28/09 1:00	19	90	2.93	-76.03	5600	5364	1	1.57086	Duration of 90 minutes
10/28/09 1:00	19	120	2.93	-76.03	5600	5364	1	1.258901	Duration of 2 hours
10/28/09 1:00	19	180	2.93	-76.03	5600	5364	1	1.529077	Duration of 3 hours
10/28/09 1:00	19	300	2.93	-76.03	5600	5364	1	2.142156	Duration of 5 hours
10/28/09 1:00	19	450	2.93	-76.03	5600	5364	1	2.157743	Duration of 7.5 hours
10/28/09 1:00	19	600	2.93	-76.03	5600	5364	1	2.168282	Duration of 10 hours
10/28/09 1:00	19	750	2.93	-76.03	5600	5364	1	2.167045	Duration of 12.5 hours
10/28/09 1:00	19	900	2.93	-76.03	5600	5364	1	2.175364	Duration of 15 hours
10/28/09 1:00	19	1080	2.93	-76.03	5600	5364	1	null	Duration of 18 hours
10/28/09 1:00	19	1260	2.93	-76.03	5600	5364	1	null	Duration of 21 hours
10/28/09 1:00	19	120	2.93	-76.03	5600	5364	1	1.258901	Revised Proposed Ideal (using data from time and duration sensitivity analysis)
Sensitivity analysis of mass units									
10/28/09 1:00	19	120	2.93	-76.03	5600	5364	1	1.258901	Mass at 1 unit
10/28/09 1:00	19	120	2.93	-76.03	5600	5364	5	1.250077	Mass adjusted to 5 units
10/28/09 1:00	19	120	2.93	-76.03	5600	5364	10	1.246858	Mass adjusted to 10 units
10/28/09 1:00	19	120	2.93	-76.03	5600	5364	25	1.240746	Mass adjusted to 25 units
10/28/09 1:00	19	120	2.93	-76.03	5600	5364	50	1.236634	Mass adjusted to 50 units
10/28/09 1:00	19	120	2.93	-76.03	5600	5364	100	1.23281	Mass adjusted to 100 units
10/28/09 1:00	19	120	2.93	-76.03	5600	5364	500	1.220822	Mass adjusted to 500 units
10/28/09 1:00	19	120	2.93	-76.03	5600	5364	1000	1.216224	Mass adjusted to 1000 units
10/28/09 1:00	19	120	2.93	-76.03	5600	5364	5000	1.201974	Mass adjusted to 5000 units
10/28/09 1:00	19	120	2.93	-76.03	5600	5364	10000	1.196364	Mass adjusted to 10000 units

Nevado del Huila									
Sensitivity Analysis									
Start Date	Time frame	Duration	Origination		Release	Release	Mass		
and Time	in hrs	in min	Lat	Long	Top in m	Bottom in m	Units	Error	Description
10/28/09 1:00	19	120	2.93	-76.03	5600	5364	50000	1.179157	Mass adjusted to 50000 units
10/28/09 1:00	19	120	2.93	-76.03	5600	5364	100000	1.172198	Mass adjusted to 100,000
10/28/09 1:00	19	120	2.93	-76.03	5600	5364	500000	1.151045	Mass adjusted to 500,000
10/28/09 1:00	19	120	2.93	-76.03	5600	5364	1000000	1.142248	Mass adjusted to 1,000,000
10/28/09 1:00	19	120	2.93	-76.03	5600	5364	5000000	1.115728	Mass adjusted to 5,000,000
10/28/09 1:00	19	120	2.93	-76.03	5600	5364	10000000	1.104382	Mass adjusted to 10,000,000
10/29/09 1:00	19	120	2.93	-76.03	5600	5364	100,000,000	1.055634	Mass adjusted to 100,000,000
10/28/09 1:00	19	120	2.93	-76.03	5600	5364	100000000	1.055634	Revised Proposed Ideal (using sensitivity analysis of time, duration and mass unit)
Sensitivity analysis of Top of Release altitude									
10/28/09 1:00	19	120	2.93	-76.03	5500	5364	100000000	1.116655	Top of release altitude adjusted to 5500 m
10/28/09 1:00	19	120	2.93	-76.03	5600	5364	100000000	1.055634	Top of release altitude adjusted to 5600 m
10/28/09 1:00	19	120	2.93	-76.03	5750	5364	100000000	1.047208	Top of release altitude adjusted to 5750 m
10/28/09 1:00	19	120	2.93	-76.03	6000	5364	100000000	1.305513	Top of release altitude adjusted to 6000 m
10/28/09 1:00	19	120	2.93	-76.03	6500	5364	100000000	0.7652537	Top of release altitude adjusted to 6500 m
10/28/09 1:00	19	120	2.93	-76.03	7000	5364	100000000	0.8263977	Top of release altitude adjusted to 7000 m
10/28/09 1:00	19	120	2.93	-76.03	7500	5364	100000000	0.8106974	Top of release altitude adjusted to 7500 m

Nevado del Huila									
Sensitivity Analysis									
Start Date	Time frame	Duration	Origination		Release	Release	Mass		
and Time	in hrs	in min	Lat	Long	Top in m	Bottom in m	Units	Error	Description
10/28/09 1:00	19	120	2.93	-76.03	8000	5364	100000000	0.9494559	Top of release altitude adjusted to 8000 m
10/28/09 1:00	19	120	2.93	-76.03	8500	5364	100000000	0.9314221	Top of release altitude adjusted to 8500 m
10/28/09 1:00	19	120	2.93	-76.03	6500	5364	100000000	0.7652537	Revised Proposed Ideal (using sensitivity analysis of time, duration, mass units, latitude, longitude and top of release)
Sensitivity analysis of Bottom of Release altitude									
10/28/09 1:00	19	120	2.93	-76.03	6500	6000	100000000	0.8263609	Bottom of release altitude adjusted to 6000 m
10/28/09 1:00	19	120	2.93	-76.03	6500	5500	100000000	0.745451	Bottom of release altitude adjusted to 5500 m
10/28/09 1:00	19	120	2.93	-76.03	6500	5364	100000000	0.7652537	Bottom of release altitude adjusted to 5364 m
10/28/09 1:00	19	120	2.93	-76.03	6500	5200	100000000	1.10203	Bottom of release altitude adjusted to 5200 m
10/28/09 1:00	19	120	2.93	-76.03	6500	5000	100000000	1.228955	Bottom of release altitude adjusted to 5000 m
10/28/09 1:00	19	120	2.93	-76.03	6500	4700	100000000	1.383054	Bottom of release altitude adjusted to 4700 m
10/28/09 1:00	19	120	2.93	-76.03	6500	4000	100000000	1.665255	Bottom of release altitude adjusted to

Nevado del Huila									
Sensitivity Analysis									
Start Date	Time frame	Duration	Origination		Release	Release	Mass		
and Time	in hrs	in min	Lat	Long	Top in m	Bottom in m	Units	Error	Description
									4000 m
10/28/09 1:00	19	120	2.93	-76.03	6500	5364	100000000	0.7652537	Revised Proposed Ideal (using sensitivity analysis of time, duration, mass units, latitude, longitude and top of release)
Sensitivity analysis of latitude									
10/28/09 1:00	19	120	2	-76.03	6500	5364	100000000	0.9109807	Latitude adjusted to 2N
10/28/09 1:00	19	120	2.25	-76.03	6500	5364	100000000	0.783866	Latitude adjusted to 2.25N
10/28/09 1:00	19	120	2.5	-76.03	6500	5364	100000000	0.9218416	Latitude adjusted to 2.5N
10/28/09 1:00	19	120	2.75	-76.03	6500	5364	100000000	0.8717194	Latitude adjusted to 2.75N
10/28/09 1:00	19	120	2.93	-76.03	6500	5364	100000000	0.7652537	Latitude adjusted to 2.93N
10/28/09 1:00	19	120	3.25	-76.03	6500	5364	100000000	0.9824442	Latitude adjusted to 3.25N
10/28/09 1:00	19	120	3.5	-76.03	6500	5364	100000000	0.9656475	Latitude adjusted to 3.5N
10/28/09 1:00	19	120	3.75	-76.03	6500	5364	100000000	0.6374257	Latitude adjusted to 3.75N
10/28/09 1:00	19	120	4	-76.03	6500	5364	100000000	0.8503635	Latitude adjusted to 4N
10/28/09 1:00	19	120	2.93	-76.03	6500	5364	100000000	0.7652537	Revised Proposed Ideal (using sensitivity analysis of time, duration, mass & latitude)
Sensitivity analysis of longitude									

Nevado del Huila									
Sensitivity Analysis									
Start Date	Time frame	Duration	Origination		Release	Release	Mass		
and Time	in hrs	in min	Lat	Long	Top in m	Bottom in m	Units	Error	Description
10/28/09 1:00	19	120	2.93	-75	6500	5364	100000000	0.8940017	Longitude adjusted to 75W
10/28/09 1:00	19	120	2.93	-75.25	6500	5364	100000000	0.9623289	Longitude adjusted to 75.25W
10/28/09 1:00	19	120	2.93	-75.5	6500	5364	100000000	0.9008625	Longitude adjusted to 75.5W
10/28/09 1:00	19	120	2.93	-75.75	6500	5364	100000000	0.9001186	Longitude adjusted to 75.75W
10/28/09 1:00	19	120	2.93	-76.03	6500	5364	100000000	0.7652537	Longitude adjusted to 76.03W
10/28/09 1:00	19	120	2.93	-76.25	6500	5364	100000000	1.051898	Longitude adjusted to 76.25W
10/28/09 1:00	19	120	2.93	-76.5	6500	5364	100000000	1.301479	Longitude adjusted to 76.5W
10/28/09 1:00	19	120	2.93	-76.75	6500	5364	100000000	1.347669	Longitude adjusted to 76.75W
10/28/09 1:00	19	120	2.93	-77	6500	5364	100000000	1.423649	Longitude adjusted to 77W
10/28/09 1:00	19	120	2.93	-76.03	6500	5364	100000000	0.7652537	Ideal (based on sensitivity analysis of time, duration, mass units, latitude, longitude & top and bottom of release data)

Nevado del Huila Optimization Data

Start Date	Time frame	Duration	Origination		Release	Release	Mass	HYSPLIT	
and Time	in hrs	in hrs	Lat	Long	Top in m	Bottom in m	Units	Job #	Error
10/27/09 23:00	21	0.5	2.93	-76.03	5500	5364	100000000	227562	1.882013
10/27/09 23:00	21	0.5	2.93	-76.03	6000	5364	100000000	227563	1.725817
10/27/09 23:00	21	0.5	2.93	-76.03	6500	5364	100000000	227564	1.687087
10/27/09 23:00	21	0.5	2.93	-76.03	7000	5364	100000000	227565	1.54689
10/27/09 23:00	21	1	2.93	-76.03	5500	5364	100000000	227566	1.917619
10/27/09 23:00	21	1	2.93	-76.03	6000	5364	100000000	227567	1.769042
10/27/09 23:00	21	1	2.93	-76.03	6500	5364	100000000	227568	1.744865
10/27/09 23:00	21	1	2.93	-76.03	7000	5364	100000000	227569	1.497945
10/27/09 23:00	21	2	2.93	-76.03	5500	5364	100000000	227570	1.850357
10/27/09 23:00	21	2	2.93	-76.03	6000	5364	100000000	227571	1.718537
10/27/09 23:00	21	2	2.93	-76.03	6500	5364	100000000	227572	1.634396
10/27/09 23:00	21	2	2.93	-76.03	7000	5364	100000000	227573	1.371988
10/27/09 23:00	21	3	2.93	-76.03	5500	5364	100000000	227574	1.68862
10/27/09 23:00	21	3	2.93	-76.03	6000	5364	100000000	227575	1.721857
10/27/09 23:00	21	3	2.93	-76.03	6500	5364	100000000	227576	1.495692
10/27/09 23:00	21	3	2.93	-76.03	7000	5364	100000000	227577	1.347072
10/28/09 0:00	20	0.5	2.93	-76.03	5500	5364	100000000	227578	1.670487
10/28/09 0:00	20	0.5	2.93	-76.03	6000	5364	100000000	227579	abort
10/28/09 0:00	20	0.5	2.93	-76.03	6500	5364	100000000	227580	1.204083
10/28/09 0:00	20	0.5	2.93	-76.03	7000	5364	100000000	227581	1.142598
10/28/09 0:00	20	1	2.93	-76.03	5500	5364	100000000	227582	1.543139
10/28/09 0:00	20	1	2.93	-76.03	6000	5364	100000000	227583	1.599321
10/28/09 0:00	20	1	2.93	-76.03	6500	5364	100000000	227584	1.411179
10/28/09 0:00	20	1	2.93	-76.03	7000	5364	100000000	227585	1.273941

Start Date and Time	Time frame in hrs	Duration in hrs	Origination Lat	Long	Release Top in m	Release Bottom in m	Mass Units	HYSPLIT Job #	Error
10/28/09 0:00	20	2	2.93	-76.03	5500	5364	100000000	227586	1.490085
10/28/09 0:00	20	2	2.93	-76.03	6000	5364	100000000	227587	1.568746
10/28/09 0:00	20	2	2.93	-76.03	6500	5364	100000000	227588	1.280197
10/28/09 0:00	20	2	2.93	-76.03	7000	5364	100000000	227589	1.186654
10/28/09 0:00	20	3	2.93	-76.03	5500	5364	100000000	227590	1.466306
10/28/09 0:00	20	3	2.93	-76.03	6000	5364	100000000	227591	1.499272
10/28/09 0:00	20	3	2.93	-76.03	6500	5364	100000000	227592	1.072447
10/28/09 0:00	20	3	2.93	-76.03	7000	5364	100000000	227593	0.959051
10/28/2009 1:00	19	0.5	2.93	-76.03	5500	5364	100000000	227598	1.132756
10/28/2009 1:00	19	0.5	2.93	-76.03	6000	5364	100000000	227599	1.378402
10/28/2009 1:00	19	0.5	2.93	-76.03	6500	5364	100000000	227600	0.951602
10/28/2009 1:00	19	0.5	2.93	-76.03	7000	5364	100000000	227601	0.998215
10/28/2009 1:00	19	1	2.93	-76.03	5500	5364	100000000	227603	1.141708
10/28/2009 1:00	19	1	2.93	-76.03	6000	5364	100000000	227604	1.062496
10/28/2009 1:00	19	1	2.93	-76.03	6500	5364	100000000	227605	0.971898
10/28/2009 1:00	19	1	2.93	-76.03	7000	5364	100000000	227606	0.957156
10/28/2009 1:00	19	2	2.93	-76.03	5500	5364	100000000	227607	1.116655
10/28/2009 1:00	19	2	2.93	-76.03	6000	5364	100000000	227608	1.305513
10/28/2009 1:00	19	2	2.93	-76.03	6500	5364	100000000	227609	0.765254
10/28/2009 1:00	19	2	2.93	-76.03	6750	5364	100000000	227706	0.834211
10/28/2009 1:00	19	2	2.93	-76.03	7000	5364	100000000	227610	0.826398
10/28/2009 1:00	19	2	2.93	-76.03	7500	5364	100000000	227709	0.810697
10/28/2009 1:00	19	2.5	2.93	-76.03	6500	5364	100000000	227707	1.126336
10/28/2009 1:00	19	2.5	2.93	-76.03	6750	5364	100000000	227708	1.047026
10/28/2009 1:00	19	2.5	2.93	-76.03	7000	5364	100000000	227710	0.810697
10/28/2009 1:00	19	2.5	2.93	-76.03	7500	5364	100000000	227711	abort
10/28/2009 1:00	19	3	2.93	-76.03	5500	5364	100000000	227611	1.29826
10/28/2009 1:00	19	3	2.93	-76.03	6000	5364	100000000	227612	1.336611
10/28/2009 1:00	19	3	2.93	-76.03	6500	5364	100000000	227613	0.846736
10/28/2009 1:00	19	3	2.93	-76.03	6750	5364	100000000	227712	1.041179

Start Date	Time frame	Duration	Origination		Release	Release	Mass	HYSPLIT	
and Time	in hrs	in hrs	Lat	Long	Top in m	Bottom in m	Units	Job #	Error
10/28/2009 1:00	19	3	2.93	-76.03	7000	5364	100000000	227614	0.825602
10/28/2009 1:00	19	3	2.93	-76.03	7500	5364	100000000	227713	0.780889
10/28/2009 1:00	20	2	2.93	-76.03	6500	5364	100000000	227714	0.947109
10/28/2009 1:00	20	2	2.93	-76.03	6750	5364	100000000	227715	0.888785
10/28/2009 1:00	20	2	2.93	-76.03	7000	5364	100000000	227716	0.883612
10/28/2009 1:00	20	2	2.93	-76.03	7500	5364	100000000	227717	0.925995
10/28/2009 1:00	20	2.5	2.93	-76.03	6500	5364	100000000	227718	0.91878
10/28/2009 1:00	20	2.5	2.93	-76.03	6750	5364	100000000	227719	0.897259
10/28/2009 1:00	20	2.5	2.93	-76.03	7000	5364	100000000	227720	0.926253
10/28/2009 1:00	20	2.5	2.93	-76.03	7500	5364	100000000	227721	0.906636
10/28/2009 1:00	20	3	2.93	-76.03	6500	5364	100000000	227722	0.963775
10/28/2009 1:00	20	3	2.93	-76.03	6750	5364	100000000	227723	0.951353
10/28/2009 1:00	20	3	2.93	-76.03	7000	5364	100000000	227724	0.941386
10/28/2009 1:00	20	3	2.93	-76.03	7500	5364	100000000	227725	0.947619
10/28/2009 2:00	18	0.5	2.93	-76.03	5500	5364	100000000	227616	null
10/28/2009 2:00	18	0.5	2.93	-76.03	6000	5364	100000000	227617	null
10/28/2009 2:00	18	0.5	2.93	-76.03	6500	5364	100000000	227618	0.777176
10/28/2009 2:00	18	0.5	2.93	-76.03	7000	5364	100000000	227619	0.818404
10/28/2009 2:00	18	1	2.93	-76.03	5500	5364	100000000	227620	null
10/28/2009 2:00	18	1	2.93	-76.03	6000	5364	100000000	227623	null
10/28/2009 2:00	18	1	2.93	-76.03	6500	5364	100000000	227625	0.817542
10/28/2009 2:00	18	1	2.93	-76.03	7000	5364	100000000	227627	0.847875
10/28/2009 2:00	18	2	2.93	-76.03	5500	5364	100000000	227628	null
10/28/2009 2:00	18	2	2.93	-76.03	6000	5364	100000000	227629	null
10/28/2009 2:00	18	2	2.93	-76.03	6500	5364	100000000	227630	0.908791
10/28/2009 2:00	18	2	2.93	-76.03	7000	5364	100000000	227631	0.846306
10/28/2009 2:00	18	3	2.93	-76.03	5500	5364	100000000	227632	null
10/28/2009 2:00	18	3	2.93	-76.03	6000	5364	100000000	227633	null
10/28/2009 2:00	18	3	2.93	-76.03	6500	5364	100000000	227634	0.934762
10/28/2009 2:00	18	3	2.93	-76.03	7000	5364	100000000	227635	0.773771

Start Date	Time frame	Duration	Origination		Release	Release	Mass	HYSPLIT	
and Time	in hrs	in hrs	Lat	Long	Top in m	Bottom in m	Units	Job #	Error
10/28/2009 2:00	18	3	2.93	-76.03	7500	5364	100000000	227726	0.97089
10/27/2009 20:00	24	0.5	2.93	-76.03	5500	5364	100000000	227636	1.815022
10/27/2009 20:00	24	0.5	2.93	-76.03	6000	5364	100000000	227637	1.913241
10/27/2009 20:00	24	0.5	2.93	-76.03	6500	5364	100000000	227638	1.817564
10/27/2009 20:00	24	0.5	2.93	-76.03	7000	5364	100000000	227639	1.598576
10/27/2009 20:00	24	1	2.93	-76.03	5500	5364	100000000	227640	1.835131
10/27/2009 20:00	24	1	2.93	-76.03	6000	5364	100000000	227641	1.929021
10/27/2009 20:00	24	1	2.93	-76.03	6500	5364	100000000	227642	1.775443
10/27/2009 20:00	24	1	2.93	-76.03	7000	5364	100000000	227643	1.615455
10/27/2009 20:00	24	2	2.93	-76.03	5500	5364	100000000	227644	1.846689
10/27/2009 20:00	24	2	2.93	-76.03	6000	5364	100000000	227645	1.903118
10/27/2009 20:00	24	2	2.93	-76.03	6500	5364	100000000	227646	1.686289
10/27/2009 20:00	24	2	2.93	-76.03	7000	5364	100000000	227647	1.602671
10/27/2009 20:00	24	3	2.93	-76.03	5500	5364	100000000	227648	1.922906
10/27/2009 20:00	24	3	2.93	-76.03	6000	5364	100000000	227649	1.864529
10/27/2009 20:00	24	3	2.93	-76.03	6500	5364	100000000	227650	1.69294
10/27/2009 20:00	24	3	2.93	-76.03	7000	5364	100000000	227651	1.594897
10/27/2009 15:00	27	0.5	2.93	-76.03	5500	5364	100000000	227652	1.835606
10/27/2009 15:00	27	0.5	2.93	-76.03	6000	5364	100000000	227653	1.791052
10/27/2009 15:00	27	0.5	2.93	-76.03	6500	5364	100000000	227654	1.606696
10/27/2009 15:00	27	0.5	2.93	-76.03	7000	5364	100000000	227655	1.600373
10/27/2009 15:00	27	1	2.93	-76.03	5500	5364	100000000	227656	1.791233
10/27/2009 15:00	27	1	2.93	-76.03	6000	5364	100000000	227657	1.730372
10/27/2009 15:00	27	1	2.93	-76.03	6500	5364	100000000	227658	1.603548
10/27/2009 15:00	27	1	2.93	-76.03	7000	5364	100000000	227659	1.675677
10/27/2009 15:00	27	2	2.93	-76.03	5500	5364	100000000	227660	1.845624
10/27/2009 15:00	27	2	2.93	-76.03	6000	5364	100000000	227661	1.651207
10/27/2009 15:00	27	2	2.93	-76.03	6500	5364	100000000	227662	1.597353
10/27/2009 15:00	27	2	2.93	-76.03	7000	5364	100000000	227663	1.670551
10/27/2009 15:00	27	3	2.93	-76.03	5500	5364	100000000	227667	1.888475

Start Date and Time	Time frame in hrs	Duration in hrs	Origination Lat	Long	Release Top in m	Release Bottom in m	Mass Units	HYSPLIT Job #	Error
10/27/2009 15:00	27	3	2.93	-76.03	6000	5364	100000000	227669	1.790326
10/27/2009 15:00	27	3	2.93	-76.03	6500	5364	100000000	227670	1.683756
10/27/2009 15:00	27	3	2.93	-76.03	7000	5364	100000000	227671	1.604068
10/27/2009 16:00	27	0.5	2.93	-76.03	5500	5364	100000000	227672	1.768278
10/27/2009 16:00	27	0.5	2.93	-76.03	6000	5364	100000000	227673	1.739714
10/27/2009 16:00	27	0.5	2.93	-76.03	6500	5364	100000000	227674	1.668617
10/27/2009 16:00	27	0.5	2.93	-76.03	7000	5364	100000000	227675	1.568481
10/27/2009 16:00	27	1	2.93	-76.03	5500	5364	100000000	227676	1.739678
10/27/2009 16:00	27	1	2.93	-76.03	6000	5364	100000000	227677	1.74062
10/27/2009 16:00	27	1	2.93	-76.03	6500	5364	100000000	227678	1.659409
10/27/2009 16:00	27	1	2.93	-76.03	7000	5364	100000000	227679	1.569649
10/27/2009 16:00	27	2	2.93	-76.03	5500	5364	100000000	227680	1.759291
10/27/2009 16:00	27	2	2.93	-76.03	6000	5364	100000000	227681	1.777426
10/27/2009 16:00	27	2	2.93	-76.03	6500	5364	100000000	227682	1.699685
10/27/2009 16:00	27	2	2.93	-76.03	7000	5364	100000000	227683	1.601377
10/27/2009 16:00	27	3	2.93	-76.03	5500	5364	100000000	227684	1.809073
10/27/2009 16:00	27	3	2.93	-76.03	6000	5364	100000000	227685	1.833796
10/27/2009 16:00	27	3	2.93	-76.03	6500	5364	100000000	227686	1.697649
10/27/2009 16:00	27	3	2.93	-76.03	7000	5364	100000000	227687	1.607747
10/27/2009 16:00	26	0.5	2.93	-76.03	5500	5364	100000000	227672	1.833804
10/27/2009 16:00	26	0.5	2.93	-76.03	6000	5364	100000000	226673	1.628878
10/27/2009 16:00	26	0.5	2.93	-76.03	6500	5364	100000000	227674	1.646767
10/27/2009 16:00	26	0.5	2.93	-76.03	7000	5364	100000000	227675	1.650807
10/27/2009 16:00	26	1	2.93	-76.03	5500	5364	100000000	227676	1.838136
10/27/2009 16:00	26	1	2.93	-76.03	6000	5364	100000000	227677	1.73151
10/27/2009 16:00	26	1	2.93	-76.03	6500	5364	100000000	227678	1.605928
10/27/2009 16:00	26	1	2.93	-76.03	7000	5364	100000000	227679	1.598073
10/27/2009 16:00	26	2	2.93	-76.03	5500	5364	100000000	227680	1.887255
10/27/2009 16:00	26	2	2.93	-76.03	6000	5364	100000000	227681	1.70404
10/27/2009 16:00	26	2	2.93	-76.03	6500	5364	100000000	227682	1.676969

Start Date	Time frame	Duration	Origination		Release	Release	Mass	HYSPLIT	
and Time	in hrs	in hrs	Lat	Long	Top in m	Bottom in m	Units	Job #	Error
10/27/2009 16:00	26	2	2.93	-76.03	7000	5364	100000000	227683	1.595976
10/27/2009 16:00	26	3	2.93	-76.03	5500	5364	100000000	227684	1.929731
10/27/2009 16:00	26	3	2.93	-76.03	6000	5364	100000000	227685	1.747007
10/27/2009 16:00	26	3	2.93	-76.03	6500	5364	100000000	227686	abort
10/27/2009 16:00	26	3	2.93	-76.03	7000	5364	100000000	227687	1.592025
10/27/2009 17:00	27	0.5	2.93	-76.03	5500	5364	100000000	227704	1.581264
10/27/2009 17:00	27	0.5	2.93	-76.03	6000	5364	100000000	227689	1.601079
10/27/2009 17:00	27	0.5	2.93	-76.03	6500	5364	100000000	227690	1.684812
10/27/2009 17:00	27	0.5	2.93	-76.03	7000	5364	100000000	227691	1.567573
10/27/2009 17:00	27	1	2.93	-76.03	5500	5364	100000000	227692	1.618297
10/27/2009 17:00	27	1	2.93	-76.03	6000	5364	100000000	227693	1.660973
10/27/2009 17:00	27	1	2.93	-76.03	6500	5364	100000000	227694	1.624961
10/27/2009 17:00	27	1	2.93	-76.03	7000	5364	100000000	227695	1.454868
10/27/2009 17:00	27	2	2.93	-76.03	5500	5364	100000000	227696	1.656957
10/27/2009 17:00	27	2	2.93	-76.03	6000	5364	100000000	227697	1.754797
10/27/2009 17:00	27	2	2.93	-76.03	6500	5364	100000000	227698	1.785671
10/27/2009 17:00	27	2	2.93	-76.03	7000	5364	100000000	227699	1.589858
10/27/2009 17:00	27	3	2.93	-76.03	5500	5364	100000000	227700	1.786265
10/27/2009 17:00	27	3	2.93	-76.03	6000	5364	100000000	227701	1.807399
10/27/2009 17:00	27	3	2.93	-76.03	6500	5364	100000000	227702	1.692938
10/27/2009 17:00	27	3	2.93	-76.03	7000	5364	100000000	227703	1.569749
10/27/2009 17:00	26	0.5	2.93	-76.03	5500	5364	100000000	227704	1.760466
10/27/2009 17:00	26	0.5	2.93	-76.03	6000	5364	100000000	227689	1.778712
10/27/2009 17:00	26	0.5	2.93	-76.03	6500	5364	100000000	227690	1.694367
10/27/2009 17:00	26	0.5	2.93	-76.03	7000	5364	100000000	227691	1.572176
10/27/2009 17:00	26	1	2.93	-76.03	5500	5364	100000000	227692	1.790945
10/27/2009 17:00	26	1	2.93	-76.03	6000	5364	100000000	227693	1.798614
10/27/2009 17:00	26	1	2.93	-76.03	6500	5364	100000000	227694	1.622064
10/27/2009 17:00	26	1	2.93	-76.03	7000	5364	100000000	227695	1.59688
10/27/2009 17:00	26	2	2.93	-76.03	5500	5364	100000000	227696	1.822455

Start Date	Time frame	Duration	Origination		Release	Release	Mass	HYSPLIT	
and Time	in hrs	in hrs	Lat	Long	Top in m	Bottom in m	Units	Job #	Error
10/27/2009 17:00	26	2	2.93	-76.03	6000	5364	100000000	227697	1.847914
10/27/2009 17:00	26	2	2.93	-76.03	6500	5364	100000000	227698	1.699189
10/27/2009 17:00	26	2	2.93	-76.03	7000	5364	100000000	227699	1.627953
10/27/2009 17:00	26	3	2.93	-76.03	5500	5364	100000000	227700	1.849926
10/27/2009 17:00	26	3	2.93	-76.03	6000	5364	100000000	227701	1.915593
10/27/2009 17:00	26	3	2.93	-76.03	6500	5364	100000000	227702	1.747379
10/27/2009 17:00	26	3	2.93	-76.03	7000	5364	100000000	227703	1.614922
10/27/2009 17:00	25	0.5	2.93	-76.03	5500	5364	100000000	227704	1.851156
10/27/2009 17:00	25	0.5	2.93	-76.03	6000	5364	100000000	227689	1.719986
10/27/2009 17:00	25	0.5	2.93	-76.03	6500	5364	100000000	227690	1.677182
10/27/2009 17:00	25	0.5	2.93	-76.03	7000	5364	100000000	227691	1.603538
10/27/2009 17:00	25	1	2.93	-76.03	5500	5364	100000000	227692	1.909519
10/27/2009 17:00	25	1	2.93	-76.03	6000	5364	100000000	227693	1.727681
10/27/2009 17:00	25	1	2.93	-76.03	6500	5364	100000000	227694	1.702627
10/27/2009 17:00	25	1	2.93	-76.03	7000	5364	100000000	227695	1.619762
10/27/2009 17:00	25	2	2.93	-76.03	5500	5364	100000000	227696	1.936356
10/27/2009 17:00	25	2	2.93	-76.03	6000	5364	100000000	227697	1.760129
10/27/2009 17:00	25	2	2.93	-76.03	6500	5364	100000000	227698	1.734666
10/27/2009 17:00	25	2	2.93	-76.03	7000	5364	100000000	227699	1.59712
10/27/2009 17:00	25	3	2.93	-76.03	5500	5364	100000000	227700	1.958705
10/27/2009 17:00	25	3	2.93	-76.03	6000	5364	100000000	227701	1.867089
10/27/2009 17:00	25	3	2.93	-76.03	6500	5364	100000000	227702	1.702635
10/27/2009 17:00	25	3	2.93	-76.03	7000	5364	100000000	227703	1.619387
								Sum	279.979
								Count	186
								Mean	1.505264
								Std Dev	0.347168
								Min	0.765254
								Max	
								Median	1.619575

REFERENCES

Admin. (2008, July 9). Write Charlie's FAQ. *IB Chemistry*. Retrieved November 26, 2012, from http://www.ibchem.com/faq/wp-content/uploads/2008/07/so2.gif

Air Resources Laboratory. (2012, April). Air Resources Laboratory - HYSPLIT Model Research. NOAA, Air Resources Laboratory. Retrieved from http://www.arl.noaa.gov/documents/Summaries/Dispersion_HYSPLIT.pdf

Aiuppa, A., Franco, A., von Glasow, R., Allen, A. G., D'Alessandro, W., Mather, T. A., … Valenza, M. (2007). The tropospheric processing of acidic gases and hydrogen sulfide in volcanic gas plumes as inferred from field and model investigations. *Atmospheric Chemistry and Physics*, *7*, 1441–1450.

Arellano, S. R., Hall, M., Samaniego, P., Le Pennec, J.-L., Ruiz, A., Molina, I., & Yepes, H. (2008). Degassing patterns of Tungurahua volcano (Ecuador) during the 1999-2006 eruptive period, inferred from remote spectroscopic measurements of SO2 emissions. *Journal of Volcanology and Geothermal Research*, *176*, 151–162.

Bani, P., Oppenheimer, C., Allard, P., Shinohara, H., Tsanev, V., Carn, S. A., … Garaebiti, E. (2012). First estimate of volcanic SO2 budget for Vanuatu island arc. *Journal of Volcanology and Geothermal Research*, *211-212*, 36–46.

Baxter, P. J. (2005). Human Impacts of Volcanoes. In J. Marti & G. G. J. Ernst (Eds.), *Volcanoes and the Environment* (pp. 273–303). Cambridge, United Kingdom: Cambridge University Press.

Bhugwant, C., Sieja, B., Bessafi, M., Staudacher, T., & Ecormier, J. (2009). Atmospheric sulfur dioxide measurements during the2005 and 2007 eruptions of the Piton de La Fournaise volcano: Implicaitons for human health and environmental changes. *Journal of Volcanology and Geothermal Research*, *184*, 208–224.

Bluth, G. J. S., Doiron, S. D., Schnetzler, C. C., Krueger, A. J., & Walter, L. S. (1992). Global Tracking of the SO2 Clouds from the June, 1991 Mount Pinatubo Eruptions. *Geophysical Research Letters*, *19*(2), 151–154.

Boichu, M., Oppenheimer, C., Tsanev, V., & Kyle, P. R. (2010). High temporal resolution SO2 flux measurements at Erebus volcano, Antarctica. *Journal of*

Volcanology and Geothermal Research, *190*(3-4), 325–336. doi:10.1016/j.jvolgeores.2009.11.020

Branca, S., Coltelli, M., De Beni, E., & Wijbrans, J. (2007). Geological evolution of Mount Etna volcano (Italy) from earliest products until the first central volcanism (between 500 and 100 ka ago) inferred from geochronological and stratigraphic data. *International Journal of Earth Sciences*, *97*(1), 135–152. doi:10.1007/s00531-006-0152-0

Bridgman, H. (2005). Atmosphere. In J. Oliver (Ed.), *The Encyclopedia of World Climatology* (p. 125). Dordrecht, The Netherlands: Springer.

Burton, M. R., Caltabiano, T., Mure, F., Salerno, G., & Randazzo, D. (2009). SO2 flux from Stromboli during the 2007 eruption: Results from the FLAME network and traverse measurements. *Journal of Volcanology and Geothermal Research*, *182*, 214–220.

Cannata, A., Montalto, P., Privitera, E., Russo, G., & Gresta, S. (2009). Tracking eruptive phenomena by infrasound: May 13, 2008 eruption at Mt. Etna. *Geophysical Research Letters*, *36*(5). doi:10.1029/2008GL036738

Carn, S. A., Froyd, K. D., Anderson, B. E., Wennberg, P., Crounse, J., Spencer, K., … Vay, S. A. (2011). In situ measurements of tropospheric volcanic plumes in Ecuador and Colombia during TC 4. *Journal of Geophysical Research*, *116*. doi:10.1029/2010JD014718

Carn, S. A., Krotkov, N. A., Yang, K., Hoff, R. M., Prata, A. J., Krueger, A. J., … Levelt, P. F. (2007). Extended observations of volcanic SO2 and sulfate aerosol in the stratosphere. *Atmospheric Chemistry and Physics Discussions*, *7*(1), 2857–2871. doi:10.5194/acpd-7-2857-2007

Carn, S. A., Prata, A. J., & Karlsdóttir, S. (2008). Circumpolar transport of a volcanic cloud from Hekla (Iceland). *Journal of Geophysical Research*, *113*(D14). doi:10.1029/2008JD009878

Carn, S., Krueger, A., Bluth, G., Schaefer, S., Krotkov, N., Watson, I., & Datta, S. (2003). Volcanic eruption detection by the Total Ozone Mapping Spectrometer (TOMS) instruments: a 22-year record of sulphur dioxide and ash emissions. *Geological Society, London, Special Publications*, *213*, 177–202. doi:10.1144/GSL.SP.2003.213.01.11

Carn, S.A., Krueger, A. J., Arellano, S., Krotkov, N. A., & Yang, K. (2008). Daily monitoring of Ecuadorian volcanic degassing from space. *Journal of Volcanology and Geothermal Research*, *176*, 141–150.

Carn, Simon A., Krueger, A. J., Krotkov, N. A., Yang, K., & Evans, K. (2009). Tracking volcanic sulfur dioxide clouds for aviation hazard mitigation. *Natural Hazards*, *51*, 325–343.

Carn, Simon A., Krueger, A. J., Krotkov, N. A., Yang, K., & Levelt, P. F. (2007). Sulfur dioxide emissions from Peruvian copper smelters detected by the Ozone Monitoring Instrument. *Geophysical Research Letters*, *34*(L09801), 1–5.

Centers for Disease Control and Prevention. (1999, June). Sulfur Dioxide. *ATSDR - Sulfur Dioxide*. Agency for Toxic Substances and Disease Registry ToxFAQs. Retrieved March 24, 2013, from http://www.atsdr.cdc.gov/tfacts116.pdf

Cervone, G., & Franzese, P. (2010). Monte Carlo source detection of atmospheric emissions and error functions analysis. *Computers & Geosciences*, *36*(7), 902–909. doi:10.1016/j.cageo.2010.01.007

Clerbaux, C., Coheur, P.-F., Clarisse, L., Hadji-Lazaro, J., Hurtmans, D., Turquety, S., … Carn, S. A. (2008). Measurements of SO2 profiles in volcanic plumes from the NASA Tropospheric Emission Spectrometer (TES). *Geophysical Research Letters*, *35*(22). doi:10.1029/2008GL035566

Cordelia Maerker, K., Seidenberger, T. E., Rix, M., Valks, P., & van Geffen, J. (2008). Trajectory matching and dispersion modeling of volcanic plumes utilising space-based observations. In *Use of Remote Sensing Techniques for Monitoring Volcanoes and Seismogenic Areas* (Vol. Second Workshop, pp. 1–5). Presented at the USEReST 2008, IEEE.

Dingman, S. L. (2008). *Physical hydrology* (2nd ed.). Long Grove, IL: Waveland Press Inc.

Doutriaux-Boucher, M., & Dubuisson, P. (2009). Detection of volcanic SO2 by spaceborne infrared radiometers. *Atmospheric Research*, *92*, 69–79.

Draxler, R., Stunder, B., Rolph, G., Stein, A., & Taylor, A. (2009, January). HYSPLIT4 User's Guide. NOAA, Air Resources Laboratory. Retrieved from http://gus.arlhq.noaa.gov/~rdraxler/cover.htm

Draxler, R.R., & Rolph, G. D. (2003). HYSPLIT (Hybrid Single-Particle Lagrangian Integrated Trajectory). NOAA ARL READY Website. Retrieved from http://www.arl.noaa.gov/ready/hysplit4.html

Draxler, Roland R. (2004, June). Modeling Particle Motion or Particle Distributions (Puffs). *HYSPLIT Training Seminar*. Retrieved March 27, 2013, from http://www.arl.noaa.gov/documents/workshop/hysplit1/english/puffeqns.pdf

Draxler, Roland R., & Hess, G. D. (1998). An overview of the HYSPLIT_4 modelling system for trajectories, dispersion and deposition. *Australian Meteorological Magazine*, *47*, 295–308.

Eatough, D. J., Caka, F. M., & Farber, R. J. (1994). The Conversion of SO2 to Sulfate in the Atmosphere. *Israel Journal of Chemistry*, *34*, 301–314.

Ebbing, D. D. (1996). *General Chemistry* (5th ed.). Boston: Houghton Mifflin Company.

Ernst, G. G. J., Kervyn, M., & Teeuw, R. M. (2008). Advances in the remote sensing of volcanic activity and hazards, with speci... *International Journal of Remote Sensing*, *29*(22), 6687–6723.

ESRI. (2011). ArcGIS Desktop: Release 10. Redlands, CA: Environmental Systems Research Institute.

Faivre-Pierret, R., & Le Guern, F. (1983). Chapter 7: Health Risks Linked with Inhalation of Volcanic Gases and Aerosols. In H. Tazieff & J. Sabroux (Eds.), *Forecasting Volcanic Events* (pp. 75–76). New York: Elsevier.

Galle, B., Bobrowski, N., Carn, S., Durieux, J., Johansson, M., Kasereka, M., … Zhang, Y. (2005). Gas emissions from Nyiragongo volcano D.R. of Congo, measured by UV mini-DOAS spectroscopy. *Geophysical Research Abstracts*, *7*, 08332.

Galle, Bo, Oppenheimer, C., Geyer, A., McGonigle, A., Edmonds, M., & Horrocks, L. (2002). A miniaturised ultraviolet spectrometer for remote sensing of SO2 fluxes: a new tool for volcano sureillance. *Journal of Volcanology and Geothermal Research*, *119*, 241–254.

Georgoulias, A. K., Balis, D., Koukouli, M. E., Meleti, C., Bais, A., & Zerefos, C. (2009). A study of the total atmospheric sulfur dioxide load using ground-based measurements and the satellite derived Sulfur Dioxide Index. *Atmospheric Environment*, *43*, 1693–1701.

Gerlach, T. M., Westrich, H. R., & Symonds, R. B. (1996). Preeruption Vapor in Magma of the Climatic Mount Pinatubo Eruption: Source of the Giant Stratospheric Sulfur Dioxide Cloud. In *Fire and mud: eruptions and lahars of Mount Pinatubo, Philippines* (p. 415). Quezon City : Seattle: Philippine Institute Volcanology and Seismology ; University of Washington Press.

Giovanelli, G., Tirabassi, T., & Sandroni, S. (1979). Sulphur Dioxide Plume Structure by Mask Correlation Spectroscopy. *Atmospheric Environment*, *13*(9), 1311–1318.

Global Volcanism Program. (n.d.-a). Global Volcanism Program | Etna | Summary. *Global Volcanism Program; Etna Summary*. Retrieved April 4, 2013, from http://www.volcano.si.edu/world/volcano.cfm?vnum=0101-06=

Global Volcanism Program. (n.d.-b). Global Volcanism Program | Volcanoes of the World | Volcanoes of South America | Colombia. *Global Volcanism Program; Volcanoes of South America*. Retrieved April 3, 2013, from http://www.volcano.si.edu/world/region.cfm?rnum=1501

Grattan, J., & Brayshay, M. (1995). An Amazing and Portentous Summer: Environmental and Social Responses in Britain to the 1783 Eruption of an Iceland Volcano - 3059970.pdf. *Geographical Journal*, *161*(2), 125–134.

Grindle, T. J., & Burcham, Jr., F. W. (2002). Even minor volcanic ash encounters can cause major damage to aircraft. *ICAO Journal*, *2*, 12–14.

Hoff, R. M., & Christopher, S. A. (2009). Remote Sensing of Particulate Pollution from Space: Have We Reached the Pro... *Journal of Air & Waste Management Association*, *59*(6), 645–675. doi:10.3155/1047-3289.59.6.645

Hunt, W., Winker, D., Vaughan, M., Powell, K., Lucker, P., & Weimer, C. (2009). CALIPSO Lidar Description and Performance Assessment. *Journal of Atmospheric and Oceanic Technology*, *26*(7), 1214–1229.

Igarashi, Y., Sawa, Y., Yoshioka, K., Matsueda, H., Fujii, K., & Dokiya, Y. (2004). Monitoring the SO2 concentration at the summit of Mt. Fuji and a comparison with other trace gases during winter. *Journal of Geophysical Research*, *109*(D17304), 1–21.

Johansson, M., Galle, B., Zhang, Y., Rivera, C., Chen, D., & Wyser, K. (2009). The dual-beam mini-DOAS technique--measurements of volcanic gas emission, plume height and plume speed with a single instrument. *Bulletin of Volcanology*, *71*(7), 747–751. doi:10.1007/s00445-008-0260-8

Kempler, S. J. (2008, May 11). VFM.002_Feature_Classification_Flags.png (PNG Image, 1000 × 750 pixels) - Scaled (74%). *Results from NASA Giovanni CALIPSO - Lidar Data Inquiry*. Retrieved March 26, 2013, from ftp://gdata1.sci.gsfc.nasa.gov//ftp/incoming/G3/OPS/ws/136426130014775/VFM.002_Feature_Classification_Flags.png

Kempler, S. J., & Hedge, M. (2013, April 4). Giovanni - A-Train Data Collocated Along the CloudSat Track. *NASA Giovanni A-Train Data*. Retrieved April 4, 2013, from http://gdata1.sci.gsfc.nasa.gov/daac-bin/G3/results.cgi?wsid=136505079230882&app=jnrcalipso-h2p&instance_id=atrain&sid=136505036727336&gsid=atrain_173.73.157.191_1365050367

Khokhar, M., Frankenberg, C., Van Roozendael, M., Beirle, S., Kuhl, S., Richter, A., … Wagner, T. (2005). Satellite observations of atmospheric SO2 from volcanic eruptions during the time-period of 1996-2002. *Advances in Space Research*, *36*(5), 879–887.

Knabe, W. (1976). Effects of Sulfur Dioxide on Terrestrial Vegetation. *Ambio*, *5*(5/6), 213–218.

Kristiansen, N. I., Stohl, A., Prata, A. J., Richter, A., Eckhardt, S., Seibert, P., … Stebel, K. (2010). Remote sensing and inverse transport modeling of the Kasatochi eruption sulfur dioxide cloud. *Journal of Geophysical Research*, *115*. doi:10.1029/2009JD013286

Krotkov, N. A. (2012, March 17). Daily SO2 image. *NASA Goddard Space Flight Center*. Retrieved January 24, 2013, from http://so2.gsfc.nasa.gov/pix/special/2012/etna/etnaEruptionInitial_march4.html

Krueger, A., Carn, S., Krotkov, N., Serafino, G., & Vicente, G. (2008). Detection and Monitoring of Sulfur Dioxide from Satellite-based UV Sensors. In *2008 EUMETSAT Meteorological Satellite Conference and Workshop Proceedings* (Vol. Session 11). Presented at the 2008 EUMETSAT Meterological Satellite Conference, Darmstadt, Germany.

Krueger, A. J., Krotkov, N. A., Yang, K., Carn, S., Vicente, G., & Schroeder, W. (2009). Applications of Satellite-Based Sulfur Dioxide Monitoring. *IEEE Journal of Selected Topics in Applied Earth Observations and Remote Sensing*, *2*(4), 293–298.

Krueger, A. J., Walter, L. S., Bhartia, P. K., Schnetzler, C. C., Krotkov, N. A., Sprod, I., & Bluth, G. J. S. (1995). Volcanic sulfur dioxide measurements from the total ozone mapping spectrometer instruments. *Journal of Geophysical Research*, *100*(D7), 14057–14076.

Krueger, A., Krotkov, N., & Carn, S. (2008). El Chichon: The genesis of volcanic sulfur dioxide monitoring from space. *Journal of Volcanology and Geothermal Research*, *175*(4), 408–414. doi:10.1016/j.jvolgeores.2008.02.026

Lacis, A., Hansen, J., & Sato, M. (1992). Climate forcing by stratospheric aerosols. *Geophysical Research Letters*, *19*(15), 1607–1610. doi:10.1029/92GL01620

Lee, Chulkyu, Martin, R. V., van Donkelaar, A., Lee, H., Dickerson, R. R., Hains, J. C., … Schwab, J. J. (2011). SO2 emissions and lifetimes: Estimates from inverse modeling using in situ and global, space-based (SCIAMACHY and OMI) observations. *Journal of Geophysical Research*, *116*(D6). doi:10.1029/2010JD014758

Lee, L. Y. L., Kwok, R. C. W., Cheung, Y. P., & Yu, K. N. (2004). Analyses of airborne 7Be concentrations in Hong Kong using back-trajectories. *Atmospheric Environment*, *38*(40), 7033–7040. doi:10.1016/j.atmosenv.2003.11.045

Levelt, P. F., van den Oord, G. H. J., Dobber, M. R., Malkki, A., Visser, H., de Vries, J., … Saari, H. (2006). The Ozone Monitoring Instrument. *IEEE Transactions on Geoscience and Remote Sensing*, *44*(5), 1093–1101.

Linzon, S.N. (1965). Sulphur Dioxide Injury to Trees in the Vicinity of Petroleum Refineries. *The Forestry Chronicle*, *41*(2), 245–250. doi:10.5558/tfc41245-2

Linzon, Samuel N. (1971). Economic Effects of Sulfur Dioxide on Forest Growth. *Journal of the Air Pollution Control Association*, *21*(2), 81–86. doi:10.1080/00022470.1971.10469503

Lopez, T., Carn, S. A., Werner, C., Fee, D., Kelly, P., Doukas, M., … Schneider, D. (2012). Evaluation of Redoubt Volcano's sulfur dioxide emissions by the Ozone Monitoring Instrument. *Journal of Volcanology and Geothermal Research*.

Lu, Z., Streets, D. G., Zhang, Q., & Wang, S. (2012). A novel back-trajectory analysis of the origin of black carbon transported to the Himalayas and Tibetan Plateau during 1996–2010. *Geophysical Research Letters*, *39*(1). doi:10.1029/2011GL049903

McKeen, S. A., Liu, S. C., & Kiang, C. S. (1984). On the Chemistry of Statospheric SO2 from Volcanic Eruptions. *Journal of Geophysical Research*, *89*(D3), 4873–4881.

McPeters, R. D. (2013, March 24). FULLDAY_AERO.PNG (PNG Image, 640 × 480 pixels). *NASA Space-Based Measurements of Ozone and Air Quality in the Ultraviolet and Visible*. Retrieved March 26, 2013, from http://ozoneaq.gsfc.nasa.gov/images/FULLDAY_AERO.PNG

Nadeau, P., & Williams-Jones, G. (2008). Chapter 6: Beyond COSPEC: Recent advances in SO2 Monitoring Technology. In G. Williams-Jones, J. Stix, & C. Hickson

(Eds.), *The COSPEC Cookbook: Making SO2 Measurements at Active Volcanoes* (pp. 219–233). IAVCEI.

NASA. (2012). NPP. *NPP*. Retrieved November 24, 2012, from http://eospso.gsfc.nasa.gov/eos_homepage/mission_profiles/docs/NPP.pdf

NASA/Goddard Space Flight Center. (2002, October). Global Tectonic Activity Mapp of the Earth; Tectonism and Volcanism of the Last One Million Years. *Goddard Space Flight Center Planetary Geodynamics Laboratory*. NASA. Retrieved March 25, 2013, from http://denali.gsfc.nasa.gov/dtam/gtam/

NASA/Goddard Space Flight Center. (2012, December 18). OMSO2ReleaseDetails_v111_0303.doc. Retrieved March 26, 2013, from http://so2.gsfc.nasa.gov/Documentation/OMSO2ReleaseDetails_v111_0303.doc

Newhall, C. G., & Self, S. (1982). The Volcanic Explosivity Index (VEI): An Estimate of Explosive Magnitude for Historical Volcanism. *Journal of Geophysical Research*, *87*(C2), 1231–1238.

Newhook, R., Hirtle, H., Byrne, K., & Meek, M. E. (2003). Releases from copper smelters and refineries and zinc plants in Canada: human health exposure and risk characterization. *Science of The Total Environment*, *301*(1-3), 23–41. doi:10.1016/S0048-9697(02)00229-2

NOAA Satellite Services Division. (n.d.). Advanced Very High Resolution Radiometer - AVHRR. *Advanced Very High Resolution Radiometer - AVHRR*. Retrieved November 25, 2012, from http://noaasis.noaa.gov/NOAASIS/ml/avhrr.html

NOAA-Air Resources Laboratory. (2013, January 8). Air Resources Laboratory - GDAS Data Archive. *Air Resources Laboratory Global Data Assimilation System (GDAS1) Archive Information*. Retrieved April 3, 2013, from http://ready.arl.noaa.gov/gdas1.php

Prata, A. J., & Tupper, A. (2009). Aviation hazards from volcanoes: the state of the science. *Natural Hazards*, *51*(2), 239–244. doi:10.1007/s11069-009-9415-y

Read, B. (2011, January 10). Under the Ash Cloud. *Aerospace International*. Retrieved March 24, 2013, from http://media.aerosociety.com/aerospace-insight/2011/01/07/under-the-ash-cloud/3502/

Richter, A., Wittrock, F., & Burrows, J. (2006). SO2 Measurements with SCIAMACHY. Presented at the ESA Atmospheric Science Conference. Retrieved from http://earth.esa.int/workshops/atmos2006/participants/804/paper_richter_esa_06.pdf

Rix, M., Valks, P., Hao, N., van Geffen, J., Clerbaux, C., Clarisse, L., … Emmadi, S. (2009). Satellite Monitoring of Volcanic Sulfur Dioxide Emissions for Early Warning of Volcanic Hazards. *IEEE Journal of Selected Topics in Applied Earth Observations and Remote Sensing*, *2*(3), 196–206. doi:10.1109/JSTARS.2009.2031120

Robock, A. (2000). Volcanic Eruptions and Climate. *Reviews of Geophysics*, *38*(2), 191–219.

Scandone, R. (1996). Factors controlling the temporal evolution of explosive eruptions. *Journal of Volcanology and Geothermal Research*, *72*, 71–83.

Sennert, S. K. (2012). Global Volcanism Program | Volcanic Activity Reports | Smithsonian / USGS Weekly Volcanic Activity Report |. *Global Volcanism Program; Smithsonian/USGS Weekly Volcanic Activity Report*. Retrieved April 3, 2013, from http://www.volcano.si.edu/reports/usgs/

Soden, B. J., Wetherald, R. T., Stenchikov, G. L., & Robock, A. (2002). Global Cooling After the Eruption of Mount Pinatubo: A Test of Climate Feedback by Water Vapor. *Science*, *296*(5568), 727–730. doi:10.1126/science.296.5568.727

Spector, L. (2007, August 15). R.I.P. TOMS: NASA Ozone Instrument Laid to Rest After Three Decades. *NASA*. Retrieved November 25, 2012, from http://www.nasa.gov/centers/goddard/news/topstory/2007/toms_end_prt.htm

Stern, C. R. (2004). Active Andean volcanism: its geologic and tectonic setting. *Revista geológica de Chile*, *31*(2). doi:10.4067/S0716-02082004000200001

Stix, J., Williams-Jones, G., & Hickson, C. (2008). Chapter 3: Applying COSPEC at Active Volcanoes. In G. Williams-Jones, J. Stix, & C. Hickson (Eds.), *The COSPEC Cookbook: Making SO2 Gas Measurements at Active Volcanoes* (pp. 142–148). IAVCEI.

Stoiber, R. E., Williams, S. N., & Huebert, B. (1987). Annual Contribution of Sulfur Dioxide to the Atmosphere by Volcanoes. *Journal of Volcanology and Geothermal Research*, *33*, 1–8.

Thomas, H. E., & Prata, A. J. (2011). Sulphur dioxide as a volcanic ash proxy during the April–May 2010 eruption of Eyjafjallajökull Volcano, Iceland. *Atmospheric Chemistry and Physics*, *11*(14), 6871–6880. doi:10.5194/acp-11-6871-2011

Voldner, E. C., Barrie, L. A., & Sirois, A. (1986). A literature review of dry deposition of oxides of sulfur and nitrogen with emphasis on long-range transport modeling in North America. *Atmospheric Environment*, *20*(11), 2101–2123.

Wallace, P. J. (2001). Volcanic SO2 emissions and the abundance and distribution of exsolved gas in magma bodies. *Journal of Volcanology and Geothermal Research*, *108*, 85–106.

Watson, I. M., Realmuto, V. J., Rose, W. I., Prata, A. J., Bluth, G. J. S., Gu, Y., … Yu, T. (2004). Thermal infrared remote sensing of volcanic emissions using the moderate resolution imaging spectoradiometer. *Journal of Volcanology and Geothermal Research*, *135*, 75–89.

Webley, P. W., Lopez, T. M., Ekstrand, A. L., Dean, K. G., Rinkleff, P., Dehn, J., … Worden, A. (2012). Remote observations of eruptive clouds and surface thermal activity during the 2009 eruption of Redoubt volcano. *Journal of Volcanology and Geothermal Research*.

Winker, D. M., Vaughan, M. A., Omar, A., Hu, Y., Powell, K. A., Liu, Z., … Young, S. A. (2009). Overview of the CALIPSO Mission and CALIOP Data Processing Algorithms. *Journal of Atmospheric and Oceanic Technology*, *26*(11), 2310–2323. doi:10.1175/2009JTECHA1281.1

Xu, Y., & Carmichael, G. R. (1998). Modeling the Dry Deposition Velocity of Sulfur Dioxide and Sulfate in Asia. *Journal of Applied Meteorology*, *37*, 1084–1099.

Yang, K., Krotkov, N. A., Krueger, A. J., Carn, S. A., Bhartia, P. K., & Levelt, P. F. (2007a). Retrieval of large volcanic SO2 columns from the Aura Ozone Monitoring Instrument: Comparison and limitations. *Journal of Geophysical Research*, *112*(D24S43), 1–14.

Yang, K., Krotkov, N. A., Krueger, A. J., Carn, S. A., Bhartia, P. K., & Levelt, P. F. (2007b). Retrieval of large volcanic SO2 columns from the Aura Ozone Monitoring Instrument: Comparison and limitations. *Journal of Geophysical Research*, *112*(D24S43), 1–14.

Yang, K., Liu, X., Bhartia, P. K., Krotkov, N. A., Carn, S. A., Hughes, E. J., … Trahan, S. G. (2010). Direct retrieval of sulfur dioxide amount and altitude from spaceborne hyperspectral UV measurements: Theory and application. *Journal of Geophysical Research*, *115*. doi:10.1029/2010JD013982

CURRICULUM VITAE

Lori Mandable graduated from Joseph Wheeler High School, in 1989. She received her Bachelor of Science in Business Administration from American University in 1993. She was employed as a Business Analyst and Technical Consultant at American Management Systems for 7 years and is in the process of completing Master of Science in Earth Systems Science from George Mason University in 2013.